

VISCOUS FLOW COMPUTATIONS WITH THE LATTICE BOLTZMANN
EQUATION METHOD

By

DAZHI YU

A DISSERTATION PRESENTED TO THE GRADUATE SCHOOL
OF THE UNIVERSITY OF FLORIDA IN PARTIAL FULFILLMENT
OF THE REQUIREMENTS FOR THE DEGREE OF
DOCTOR OF PHILOSOPHY

UNIVERSITY OF FLORIDA

2002

ACKNOWLEDGMENTS

I would like to thank my advisors, Professors Renwei Mei and Wei Shyy, for their advice, inspiration, patience, and mentoring. They constantly provide insightful suggestions when I need help. This dissertation would not have been possible without their expert guidance and the high standards they set.

I would also like to express my gratitude to my committee members: Dr. Li-shi Luo, Professors Tony Ladd and Ulrich Kurzweg. Various stimulating technical discussions with Dr. Luo and Professor Ladd have improved the quality of the thesis.

The financial support from NASA Langley Research Center, ICASE at NASA Langley Research Center, and Dr. Shyy are greatly acknowledged.

Finally, I am forever indebted to my wife, Yuhong, and my parents for their understanding, endless patience and encouragement when it was most required.

TABLE OF CONTENTS

	<u>page</u>
ACKNOWLEDGMENTS	ii
LIST OF FIGURES	vi
ABSTRACT.....	xii
CHAPTERS	
1 INTRODUCTION	1
2 BACKGROUND OF THE LATTICE BOLTZMANN EQUATION (LBE) METHOD	7
2.1 Lattice Gas Automata	7
2.2 Lattice Boltzmann Equation	9
2.2.1 Development of LGA	9
2.2.2 Derivation of LBE from the Boltzmann Equation.....	11
2.3 From the LBE to the Navier-Stokes (NS) Equations.....	13
2.4 Two-Dimension 9-Velocity Model (D2Q9).....	16
2.5 Practical Issues in the Implementation of LBE Method.....	18
2.5.1 Boundary Conditions	18
2.5.2 Reconciliation of Resolution Requirement.....	20
2.5.3 Force Evaluation	21
2.5.4 Computational Stability and Dispersion	21
2.6 Scope of the Research.....	22
3 DEVELOPMENT OF MULTI-BLOCK METHODS IN THE LBE METHOD	25
3.1 Introduction.....	25
3.2 Basics of the Multi-Block Strategy in the LBE Method.....	27
3.3 Interface Structure and Computational Procedure.....	29
3.4 Results and Discussions.....	31
3.4.1 Lid-Driven Cavity Flow.....	31
3.4.2 Channel Flow over an Asymmetrically Placed Cylinder at $Re=100$	34
3.4.3 Steady Flow over the NACA0012 Airfoil	35
3.5 Conclusions.....	37

4	FORCE EVALUATION ON A SOLID BODY IN THE LBE METHOD.....	51
4.1	Introduction.....	51
4.1.1	Force Evaluation and Related Works	51
4.1.2	Scope of the Present Work.....	53
4.2	Methods for Force Evaluation in the LBE Method	54
4.2.1	Force Evaluation Based on Stress Integration	54
4.2.2	Force Evaluation Based on the Momentum Exchange	56
4.3	Results and Discussions.....	57
4.3.1	Pressure-Driven 2-D Channel Flow.....	57
4.3.2	Steady Uniform Flow over a Column of Cylinders	62
4.3.3	Flow over an Asymmetrically Placed Circular Cylinder in Channel with Vortex Shedding	65
4.3.4	Pressure Driven Flow in a Circular Pipe.....	66
4.3.5	Steady Uniform Flow over a Sphere.....	67
4.4	Conclusions.....	69
5	MULTI-TIME-RELAXATION MODELS IN THE LBE METHOD.....	78
5.1	Introduction.....	78
5.2	Multi-Relaxation-Time (MRT) Model	80
5.3	Results and Discussions.....	82
5.3.1	Stokes First Problem	82
5.3.2	Flow over a Cascade of Zero-Thickness, Finite Length Flat Plate....	83
5.3.3	Lid-Driven Cavity Flow.....	85
5.4	Implementation of MRT Model in the Multi-Block Method.....	86
5.4.1	Basics of the Multi-Block Strategy for MRT Model	87
5.4.2	Computational Assessment.....	91
5.5	Conclusions.....	93
6	IMPROVEMENT OF BOUNDARY TREATMENTS IN THE LBE METHOD.....	107
6.1	The Open Boundary Treatment	109
6.1.1	Introduction.....	109
6.1.2	The Proposed Inlet Treatment.....	112
6.1.3	Computational Assessment.....	113
6.1.4	Conclusions.....	116
6.2	A Unified Treatment for Solid Wall Boundary Condition in LBE.....	124
6.2.1	The Unified Boundary Condition for Solid Wall Boundary.....	126
6.2.2	Computational Assessment.....	128
6.2.3	Conclusion	134
6.3	An Improved Moving Wall Boundary Condition in LBE	142
6.3.1	Issues in the Moving Boundary Problems	142
6.3.2	Formulation for the Moving Boundary Condition.....	146
6.3.3	An Analysis on the Pressure Change near the wall and Momentum Exchange between Fluid and Solid.....	147
6.3.4	Computational Assessment.....	151

6.3.5	Conclusions.....	153
7	SUMMARY AND FUTURE WORKS	161
	LIST OF REFERENCES	166
	BIOGRAPHICAL SKETCH	170

LIST OF FIGURES

Figure	page
1.1 A 2-D, 9-velocity lattice (D2Q9) model.....	6
1.2 Bounce-back inlet condition gives $\tilde{f}_{\bar{a}}(t) = \tilde{f}_a(t)$, where $e_{\bar{a}} = -e_a$, and \sim denotes the post-collision state.....	6
2.1 A hexagonal lattice	23
2.2 Two possible results of a head-on collision in lattice gas.....	24
3.1 Interface structure between two blocks of different lattice spacing.	38
3.2 Flow chart of the computational procedure in the multi-block method.....	39
3.3 Block layout for a 2-D cavity. Lattice spacing is reduced by a factor of 8 for graphical clarity.	40
3.4 Streamlines in the cavity flow at Re=100.	40
3.5 Comparison of velocity between present results and those by Ghia <i>et al.</i> (1982).....	41
3.6 Pressure contours in the cavity flow from the single-block LBE simulation.	42
3.7 Pressure contours in the cavity from multi-block LBE solution. (For the circled region, see Figure 3.8)	42
3.8 Enlarged view of pressure contour in the circled region in Figure 3.7 near the intersection of three blocks. The figure demonstrates that the block interface and corner are well handled.....	43
3.9 Shear stress contour. Solid and dash lines represent positive and negative values, respectively.....	43
3.10 Contour of x-component mass flux ρu_x . Solid and dash lines represent positive and negative values, respectively.....	44
3.11 Contour of momentum flux in the x-direction ρu_x^2	44
3.12 The x-component of the mass flux $\rho u_x / (\rho_0 U)$ on the interface AB. In Figure 3.12- Figure 3.15, $\rho_0=1$ and $U=0.0156$	45

3.13 The x-component of the mass flux $\rho u_y / (\rho_0 U)$ on the interface AB.....	45
3.14 The x-component of the momentum flux, $\rho u_x^2 / \rho_0 U^2$, on the interface AB.	46
3.15 The y-component of the momentum flux, $\rho u_x u_y / \rho_0 U^2$, on the interface AB.....	46
3.16 Shear stress $\tau_{xy} / (\mu U / H)$ on the interface AB.....	47
3.17 Pressure on the interface AB.....	47
3.18 Instantaneous streamlines for channel flow over an asymmetrically placed cylinder at $Re=100$	47
3.19 Unsteady drag and lift coefficients on the cylinder.	48
3.20 NACA 0012 airfoil.	49
3.21 Block and lattice layout for flow over NACA 0012. The lattice spacing is reduced by a factor 32 for graphical clarity.....	49
3.22 Streamlines, pressure contour, and velocity vectors for a uniform flow over NACA 0012 airfoil at $Re=2000$	49
3.23 Grid-independence test of the velocity profiles near the leading edge at $(x-x_{LE})/L=0.06$ for flow over NACA0012 airfoil at $Re=500$	50
3.24 Comparison of C_d between the present simulation and Xfoil calculation as a function of Re for flow over NACA0012 airfoil. The straight line is the slope according to the laminar boundary layer theory.	50
4.1 Layout of the regularly spaced lattices and curved wall boundary.....	71
4.2 Variation of pressure coefficient on the surface of a circular cylinder at $Re=40$, $H/r=10$. The result is obtained using $\tau=0.6$, radius=6.6 lattice unit.	71
4.3 Lattice distribution in channel flow simulations with arbitrary Δ	72
4.4 Ratio of the wall force evaluated using Eq. (4.9) to the exact value, $\xi = \mu \frac{du_x}{dy} \big _{y=H} /$ $[-\frac{1}{2} \frac{dp}{dx} H]$ in 2-D channel flow as a function of τ for $\Delta=0.2, 1/3, 0.5$, and 0.7	72
4.5 Dimensionless wall slip velocity in the 2-D channel flow as a function of τ for $\Delta=0.2$, $1/3, 0.5$, and 0.7	73
4.6 Drag coefficient for a uniform flow over a column of cylinder over range of radius r a) $Re=100$ and b) $Re=10$	74

4.7 Comparison of the lift coefficient (Figure 4.7a) and drag coefficient (Figure 4.7b) with the benchmark results given in Schäfer and Turek (1996).	75
4.8 Ratio of the tangential force F_x on the pipe to the exact value ($\frac{dp}{dx}\pi r^2$) over a range of pipe radius r	76
4.9 Schematic for uniform flow over a sphere.....	76
4.10 Variation of the non-Stokesian correction factor with sphere radius at $Re=10$	77
5.1 Comparison of the relative error in the evolution of the wall shearstress for Stokes first problem between the SRT and MRT models.	94
5.2 Comparison of the density profiles near the leading edge ($x/L=0.0125$) between the SRT model and MRT model at $Re=1000$	94
5.3 Comparison of the density profiles at $x/L=0.5125$ between the SRT model and MRT model at $Re=1000$	95
5.4 Comparison of the viscous normal stress profiles at $x/L=0.5125$ between the SRT model and MRT model at $Re=1000$	95
5.5 Comparison of the viscous shear stress profiles at $x/L=0.5125$ between the SRT model and MRT model at $Re=1000$	96
5.6 Comparison of pressure coefficient as a function of x at $y/L=0.0125$ between the SRT model and MRT model.....	96
5.7 Comparison of viscous shear stress as a function of x at $y/L=0.0125$ between the SRT model and MRT model.....	97
5.8 Comparison of wall vorticity as a function of x between the SRT model and MRT model.....	97
5.9 Comparison of the velocity profiles of x -component at $x=\Delta$ ($i=2$).	98
5.10 Comparison of the velocity profiles of y -component at $x=\Delta$ ($i=2$).	98
5.11 Comparison of the velocity profiles of x -component at $x/H=0.5$ in the lower region of the cavity.....	99
5.12 Convergent history of drag coefficient, here $s8=s9=1/0.502$, $s2=1.81$, $s3=s5=s7=1.2$ in coarsest block. $s3$, $s5$, and $s7$ are not rescaled.	99
5.13 Convergent history of drag coefficient, here $s8=s9=1/0.502$, $s2=1.81$, $s3=s5=s7=1.2$ in coarsest block. All parameters are not rescaled.	100

5.14 Convergent history of drag coefficient, here $s8=s9=1/0.502$, $s2=s3=s5=s7=1.81$ in coarsest block. All parameters are not rescaled.	100
5.15 Comparison of velocity between SRT model, MRT model and those by Ghia <i>et al.</i> (1982).	101
5.16 Pressure contours in the cavity from the multi-block MRT LBE solution. (For the circled region, see Figure 5.17).....	102
5.17 Enlarged view of pressure contour in the circled region in Figure 5.16 near the intersection of three blocks. The figure demonstrates that the block interface and corner are well handled in MRT model.	102
5.18 Shear stress contour based on the MRT model. Solid and dash lines represent positive and negative values, respectively.	103
5.19 Contour of x-component of velocity based on the MRT model. Solid and dash lines represent positive and negative values, respectively	103
5.20 Contour of y-component of velocity based on the MRT model. Solid and dash lines represent positive and negative values, respectively	104
5.21 The x-component of the velocity u_x/U on the interface AB based on the MRT model. In Figure 5.21-Figure 5.22, $U=0.0156$	104
5.22 The x-component of the velocity u_y/U on the interface AB based on the MRT model.....	105
5.23 Pressure on the interface AB based on the MRT model.	105
5.24 Shear stress $\tau_{xy}/(\mu U/H)$ on the interface AB based on the MRT model.	106
6.1 Density contour at $Re=2000$ using bounce-back condition at inlet, upper and lower boundaries	117
6.2 Computational domain and boundary conditions.	117
6.3 Configuration of distribution functions which are used to construct inlet boundary condition.	118
6.4 Convergence history of drag coefficient and value of drag near convergence.	119
6.5 Drag coefficient after vortex shedding for both inlet conditions.	120
6.6 Convergence history of drag and lift coefficient using bounce-back inlet condition.	120
6.7 Convergence history of drag and lift coefficient using EQ inlet condition.	121

6.8 Convergence history of Drag coefficient at $Re=2000$ using bounce-back condition at inlet, upper and lower boundaries.....	121
6.9 Convergence history of Drag coefficient at $Re=2000$ using local inlet condition at inlet, upper and lower boundaries.....	122
6.10 Density contour at time equaling to 30000 lattice unit at $Re=2000$ using bounce-back condition at inlet, upper and lower boundaries.	122
6.11 Density contour at time equaling to 30000 lattice unit at $Re=2000$ using local inlet condition at inlet, upper and lower boundaries.....	122
6.12 Velocity profile at nodes which is 0.2 lattice unit to the right of inlet at x-direction.	123
6.13 Velocity profile at nodes which is 0.2 lattice unit to the right of inlet at x-direction.	123
6.14 Layout of the regularly spaced lattices and curved wall boundary.....	135
6.15 Quadratic convergence of the wall slip velocity for present boundary condition in constant pressure driven channel flow	136
6.16 Dependence of relative L_2 -norm error using Eq. (6.30) for the present boundary conditions on the lattice resolution H in steady state pressure-driven channel flow simulations.....	136
6.17 Dependence of relative L_2 -norm error using Eq. (6.33) for the present boundary conditions on the lattice resolution H	137
6.18 Relative L_2 -norm error using Eq. (6.30) as a function of Δ for different boundary conditions in steady state pressure-driven channel flow simulations.	137
6.19 Velocity profiles at different time in an impulsively started plate ($\Delta t = 1/2$) using present linear boundary condition.....	138
6.20a Relative L_2 -norm error of the velocity profile $u_x(y)$ during the initial transient of the impulsively started plate with various values of Δ for the present boundary conditions.	138
6.21 Centerline velocity variation for a uniform flow over a column of cylinders with FH, present quadratic, and present linear boundary conditions. Center of cylinder is at (130,65) lattice unit.	139
6.22 Computational domain of for flow over oscillating zero-thickness flat plate.	140

6.23 Drag coefficient C_D for flow over oscillating zero-thickness flat plate using three different boundary conditions: FH, Bouzidi <i>et al.</i> linear, and present linear scheme.....	140
6.24 Layout of the regularly spaced lattices and curved wall boundary and definition of nodes.	154
6.25 The generation of a new FBN and SBN in a moving boundary problem.....	154
6.26 The generation of a new FBN in a moving boundary problem.	154
6.27 Quadratic convergence of the wall slip velocity for present boundary condition in a constant pressure driven channel flow.	155
6.28a Convergent history of drag coefficient.	155
6.29a Density contour for the flow over a stationary cylinder.	156
6.30 Computational domain for flow due to a sinusoidally oscillation plate.	157
6.31 Pressure characteristic at a point which is one grid away to the left of the plate. FH's boundary condition is used in computation.	159
6.32 Pressure characteristic at a point which is one grid away to the left of the plate. Present boundary condition is used in computation.	160

Abstract of Dissertation Presented to the Graduate School
of the University of Florida in Partial Fulfillment of the
Requirements for the Degree of Doctor of Philosophy

VISCOUS FLOW COMPUTATIONS WITH THE LATTICE BOLTZMANN
EQUATION METHOD

By

Dazhi Yu

August 2002

Chair: Renwei Mei

Cochair: Wei Shyy

Department: Aerospace Engineering, Mechanics and Engineering Science

The lattice Boltzmann equation (LBE) method is a kinetics-based approach for fluid flow computations, and it is amenable to parallel computing. Compared to the well-established Navier-Stokes (NS) approaches, critical issues remain with the LBE method, noticeably flexible spatial resolution, boundary treatments, and dispersion and relaxation time mode. Those issues are addressed in this dissertation with improved practice presented. At the formulation level, both the single-relaxation-time (SRT) and multiple-relaxation-time (MRT) models are analyzed. The SRT model involves no artificial parameters, with a constant relaxation time regulating the physical value of fluid viscosity. The MRT model allows different relaxation time scales for different variables. Computational assessment shows that the MRT model has advantages over the SRT model in maintaining stability, reducing the oscillation, and improving the convergence rate in the computation.

A multi-block method is developed for both the SRT and MRT model to facilitate flexible spatial resolutions according to the flow structures. The formulae for information exchange at the interface between coarse and fine grids are derived to ensure the mass and momentum conservation while maintaining the second-order accuracy. A customized time matching between coarse and fine grids is also presented to ensure smooth exchange information. Results show that the multi-block method can greatly increase the computational efficiency of the LBE method without losing the accuracy.

Two methods of force evaluation in LBE are examined: one based on stress integration on the solid boundary and the other momentum exchange between fluid and solid. The momentum exchange method is found to be simpler to implement while the integration of stress requires evaluation of the detailed surface geometry and extrapolation of stress-related variables to the same surface. The momentum exchange method performs better overall.

Improved treatments for both opened and solid boundaries are presented. It is demonstrated that these treatments are simpler than those existing ones while offering second order accuracy. Furthermore, the issues associated with moving solid boundaries are addressed. The proposed technique can substantially reduce the specious pressure fluctuation as the boundary crosses the grid lines.

CHAPTER 1 INTRODUCTION

Recently, there has been much progress in developing the method of the lattice Boltzmann equation (LBE) (McNamara and Zanetti 1988, Higuera and Jimenez 1989, Chen *et al.* 1992, Qian *et al.* 1992) as an alternative, computational technique for solving complex fluid dynamic systems (Benzi *et al.* 1992, Chen and Doolen 1998). Adopting the macroscopic method for computational fluid dynamics (CFD), the macroscopic variables of interest, such as velocity \mathbf{u} and pressure p , are usually obtained by solving the Navier-Stokes (NS) equations (e.g., Peyret and Taylor 1983, Fletcher 1988). In the LBE approach, one solves the kinetic equation for the particle velocity distribution function $f(\mathbf{x}, \boldsymbol{\xi}, t)$, where $\boldsymbol{\xi}$ is the particle velocity vector, \mathbf{x} is the spatial position vector, and t is the time. The macroscopic quantities (such as mass density ρ and momentum density $\rho\mathbf{u}$) can then be obtained by evaluating the hydrodynamic moments of the distribution function f . This approach was first proposed by Frisch *et al.* (1986), with the additional theoretical foundation established in the subsequent papers, notably McNamara and Zanetti (1988), Higuera and Jimenez (1989), Koelman (1991), and Qian *et al.* (1992).

A popular kinetic model adopted in the literature is the single relaxation time approximation, the so-called Bhatnagar-Gross-Krook (BGK) model (Bhatnagar *et al.* 1954):

$$\frac{\partial f}{\partial t} + \boldsymbol{\xi} \cdot \nabla f = -\frac{1}{\lambda}(f - f^{(eq)}) \quad (1.1)$$

where $f^{(eq)}$ is the equilibrium distribution function (the Maxwell-Boltzmann distribution function), and λ is the relaxation time.

To solve for f numerically, Eq. (1.1) is first discretized in the velocity space using a finite set of velocities $\{\xi_\alpha\}$ without affecting the conservation laws (Chen and Doolen 1998, He and Luo 1997a, 1997b),

$$\frac{\partial f_\alpha}{\partial t} + \xi_\alpha \cdot \nabla f_\alpha = -\frac{1}{\lambda} (f_\alpha - f_\alpha^{(eq)}) \quad (1.2)$$

In the above equation, $f_\alpha(\mathbf{x}, t) \equiv f(\mathbf{x}, \xi_\alpha, t)$ is the distribution function associated with the α -th discrete velocity ξ_α and $f_\alpha^{(eq)}$ is the corresponding equilibrium distribution function. The 9-velocity square lattice model, which is often referred to as the D2Q9 model (Figure 1.1) has been successfully used for simulating 2-D flows. In the D2Q9 model, we use e_α to denote the discrete velocity set and we have

$$e_0 = 0,$$

$$e_\alpha = c(\cos((\alpha-1)\pi/4), \sin((\alpha-1)\pi/4)) \quad \text{for } \alpha=1, 3, 5, 7,$$

$$e_\alpha = \sqrt{2}c(\cos((\alpha-1)\pi/4), \sin((\alpha-1)\pi/4)) \quad \text{for } \alpha=2, 4, 6, 8 \quad (1.3)$$

where $c = \delta x / \delta t$, δx and δt are the lattice constant and the time step size, respectively.

The equilibrium distribution for D2Q9 model is of the form

$$f_\alpha^{(eq)} = \rho w_\alpha \left[1 + \frac{3}{c^2} e_\alpha \cdot \mathbf{u} + \frac{9}{2c^4} (e_\alpha \cdot \mathbf{u})^2 - \frac{3}{2c^2} \mathbf{u} \cdot \mathbf{u} \right] \quad (1.4)$$

where w_α is the weighting factor given by

$$w_\alpha = \begin{cases} 4/9, & \alpha = 0 \\ 1/9, & \alpha = 1, 3, 5, 7 \\ 1/36, & \alpha = 2, 4, 6, 8. \end{cases} \quad (1.5)$$

With the discretized velocity space, the density and momentum fluxes can be evaluated as

$$\rho = \sum_{k=0}^8 f_{\alpha} = \sum_{k=0}^8 f_{\alpha}^{(eq)} \quad (1.6)$$

and

$$\rho \mathbf{u} = \sum_{k=1}^8 \mathbf{e}_{\alpha} f_{\alpha} = \sum_{k=1}^8 \mathbf{e}_{\alpha} f_{\alpha}^{(eq)} \quad (1.7)$$

The speed of sound in this model is $c_s = c / \sqrt{3}$ and the equation of state is that of an ideal gas,

$$p = \rho c_s^2 \quad (1.8)$$

Equation (1.2) can be further discretized in space and time. The completely discretized form of Eq. (1.1), with the time step δt and space step $\mathbf{e}_{\alpha} \delta \mathbf{x}$, is:

$$f_{\alpha}(\mathbf{x}_i + \mathbf{e}_{\alpha} \delta \mathbf{x}, t + \delta t) - f_{\alpha}(\mathbf{x}_i, t) = -\frac{1}{\tau} [f_{\alpha}(\mathbf{x}_i, t) - f_{\alpha}^{(eq)}(\mathbf{x}_i, t)] \quad (1.9)$$

where $\tau = \lambda / \delta t$, and \mathbf{x}_i is a point in the discretized physical space. The above equation is the discrete lattice Boltzmann equation (McNamara and Zanetti 1988, Higuera and Jimenez 1989, Chen *et al.* 1992) with BGK approximation (Bhatnagar *et al.* 1954). Eq. (1.9) is usually solved in the following two steps:

$$\text{collision step:} \quad \tilde{f}_{\alpha}(\mathbf{x}_i, t + \delta t) = f_{\alpha}(\mathbf{x}_i, t) - \frac{1}{\tau} [f_{\alpha}(\mathbf{x}_i, t) - f_{\alpha}^{(eq)}(\mathbf{x}_i, t)] \quad (1.10a)$$

$$\text{streaming step:} \quad f_{\alpha}(\mathbf{x}_i + \mathbf{e}_{\alpha} \delta \mathbf{x}, t + \delta t) = \tilde{f}_{\alpha}(\mathbf{x}_i, t + \delta t) \quad (1.10b)$$

where \sim represents the post-collision state.

The viscosity in the NS equation derived from Eq. (1.8) is

$$\nu = (\tau - 1/2) c_s^2 \delta t \quad (1.11)$$

This result makes formally the LBGK scheme a second order method for solving incompressible flows (He and Luo 1997a, 1997b). The positivity of the viscosity requires that $\tau > 1/2$.

It is noted that the collision step is completely local and the streaming step takes very little computational effort. Eq. (1.9) is explicit, easy to implement, and straightforward to parallelize.

These inherent advantages of the LBE method can be best maintained with the use of a regular lattice structure (such as a square lattice or hexagonal lattice) with uniform spacing. A challenge of using the uniform grid is the need for higher resolution in high gradient region such as near wall high Reynolds number flows, and where reduced resolution is acceptable, such as the outer boundary far away from the body for external flows. In order to use the regularly spaced lattice while developing the capability to place the outer boundary far away, it is desirable to divide the computational domain into a number of grid blocks so that within each block uniform lattice spacing can be used. Such a multi-block approach has been actively employed in the Navier-Stokes (NS) equation methods with both Cartesian and curvilinear coordinates (Rai, 1985, Steger, 1991, Shyy *et al.*, 1994). A similar multi-block approach in LBE will be desirable also.

Like in any other fluid flow computations, the numerical boundary condition is a very important issue in the LBE method. Two types of boundaries are considered for, namely, the solid wall and the open boundary. Unlike solving the NS equations where the macroscopic variables, their derivatives, or a well established constraint (such as the mass continuity for pressure distributions) can often be explicitly specified at boundary (Shyy *et al.*, 1994), in the LBE method, these conditions need to be converted into distribution function f . Due to the use of the Cartesian grids, the boundary of a practically interesting geometry will often intersect with the grid lines irregularly. To obtain an accurate numerical result, it is important to resolve the geometric details in such situations. The

bounce-back scheme is a standard boundary condition. It is intuitively derived from lattice gas automata and has been extensively applied in lattice Boltzmann equation simulations. In this scheme, the particles hit the boundary and bounces back opposite to its incoming direction as illustrated in Figure 1.2.

Finally, the presence of moving boundaries is of substantial interest in many important practical problems (Shyy *et al.*, 1996). The treatment of the moving boundary can add substantial complexities and burden to a given method. In the context of the LBE method, most moving boundaries work has been reported to address the particle suspension in fluids. An overall review for the application of lattice Boltzmann method to simulation of particle-fluid suspension has been given by Ladd and Verberg (2001).

The present dissertation is structured as follows. Chapter 2 will review in detail the development of the theoretical foundation of the LBE method and the numerical implication. Chapter 3 will present the concepts related to the multi-block techniques, with special attention paid to ensure the conservation of mass and momentum fluxes across the interface between blocks. Next, in Chapter 4, methods for evaluating force (drag and lift) on a body are discussed. In Chapter 5, a multi-relaxation-time LBE model is introduced, and it is shown computationally that this model can reduce the spatial oscillations observed in the numerical high Reynolds number flow solution. In Chapter 6, suitable boundary treatment strategies will be discussed for both irregularly shaped solid walls and the moving boundary problem as well as for open boundaries. Finally, conclusions and future work are discussed in Chapter 7.

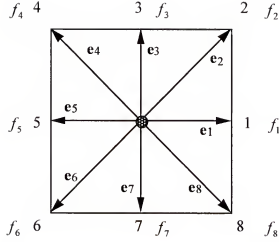


Figure 1.1 A 2-D, 9-velocity lattice (D2Q9) model.

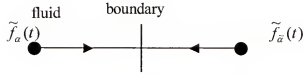


Figure 1.2 Bounce-back inlet condition gives $\tilde{f}_{\bar{\alpha}}(t) = \tilde{f}_{\alpha}(t)$, where $e_{\bar{\alpha}} = -e_{\alpha}$, and \sim denotes the post-collision state.

CHAPTER 2 BACKGROUND OF THE LATTICE BOLTZMANN EQUATION (LBE) METHOD

2.1 Lattice Gas Automata

Broadwell (1964) presented a kinetic equation with single particle speed to simulate the flow involving a shock wave. In his model, time and space are continuous. Hardy *et al.* (1976) proposed a fully discretized kinetic model on square lattice. However, due to the lack of isotropy of the lattice, this model failed to recover the NS equation. Frish, Hasslacher, Pomeau (1986) presented a 2-D kinetic model based on the hexagonal lattice. In this model, which is often referred to as the FHP model, the isotropy condition is enforced and for the first time the NS equation is successfully recovered. In the FHP model, the Boolean variables (0 or 1) are used to describe the particle occupation.

The construct of the kinetic model involves two steps. First, a correct symmetrical lattice must be designed. Second, suitable rules of evolution must be established. There are two alternatives: lattice gas automata (LGA) and lattice Boltzmann equation (McNamara and Zanetti 1988). In LGA, Boolean variables are used. At each node, a set of Boolean variables $n_\alpha(x, t)$ ($\alpha = 1, \dots, M$) is used to describe the particle state, where M is the number of particle velocities. The number n represents the state of particle. When $n_\alpha = 1$, there is a particle in the α th-direction and when $n_\alpha = 0$ there is no particle in the α th-direction. The evolution equation of LGA is as follows:

$$n_\alpha(x + e_\alpha, t + 1) = n_\alpha(x, t) + \Omega_\alpha(n(x, t)) \quad (2.1)$$

where e_α is the particle velocities and Ω_α is the collision operator. Evolution involves the following two steps:

Streaming: particle moves to the nearest neighboring nodes along its velocity direction.

Collision: when arriving at nodes, particles collide with each other and change their velocities and directions according to collision rules.

An example of the 2-D FHP kinetic model is shown in Figure 2.1 to illustrate the computational procedures. In the 2-D FHP model, the hexagonal lattice is used. At each node, there are six links to its nearest neighboring nodes. Starting from an initial state, the particles move to the neighboring nodes with unit velocity in unit time. After arriving at the new location, the particles collide with each other and change their directions. Figure 2.2 shows two possible outcomes of the head-on collision of two particles in the FHP model.

The construction of the collision rule is a crucial part in the LGA. In the collision step, the mass, momentum, and energy conservation need to be maintained while no spurious invariance should be preserved when the conservation laws are enforced. For example, the head-on collision can results in two possible scenarios as shown in Figure 2.2, but because of the lack of redistribution particles along any part of the opposite direction, these collision rules alone will generate spurious invariance. The problem can be solved by using triple collision rules or putting a rest particle at every node (Firsch *et al.* 1986).

The advantages of LGA are obvious. The evolution rules are very simple. Only Boolean operation is needed in the computation. Some special machine can be designed and built to take the advantage of these characteristics. The drawback is also obvious. The macroscopic variables need to be obtained by averaging over a large number of

possible combinations of random initial condition of particle states over a long time (Benzi *et al.* 1992). The process will inevitably produce statistical noise. When high order physical quantities such as vorticity or stress, which involves the derivatives of macroscopic variables, are needed, a much lower level of noise is needed.

2.2 Lattice Boltzmann Equation

2.2.1 Development of LGA

Historically the LBE method was derived from LGA. In LBE, the Boolean variables in the LGA are replaced by real variables, $f_\alpha = \langle n_\alpha \rangle$, in which $\langle \rangle$ represents the ensemble average. Here f_α is the particle distribution function. Because of the use of real variables, the collision rules need to be redefined in LBE. The discrete kinetic equation for particle distribution in LBE is

$$f_\alpha(\mathbf{x} + \mathbf{e}_\alpha \Delta t, t + \Delta t) = f_\alpha(\mathbf{x}, t) + \Omega_\alpha(f(\mathbf{x}, t)) \quad (2.2)$$

where $\Omega_\alpha(f(\mathbf{x}, t))$ is the collision operator which represents the rate of change of f_α due to collision, Δt is the time step, and \mathbf{e}_α is the discretized velocity in phase space and $|\mathbf{e}_\alpha| = \Delta \mathbf{x} / \Delta t$. Eq. (2.2) requires that space be discretized in a way that is consistent with the kinetic equation. The coordinates of the nearest neighbor points around \mathbf{x} are $\mathbf{x} + \mathbf{e}_\alpha$. It is noted that Ω_α depends on the local distribution function and the lattice structure.

The macroscopic variables such as density, ρ , and momentum density, $\rho \mathbf{u}$, are calculated from the moments of particle distribution function, f_α :

$$\rho = \sum_{\alpha=0}^m f_\alpha \quad \rho \mathbf{u} = \sum_{\alpha=1}^m f_\alpha \mathbf{e}_\alpha \quad (2.3)$$

where $m+1$ is the number of discretized velocity in the phase space. The collision operator must satisfy the conservation of mass and momentum at each node,

$$\sum_{\alpha=0}^m \Omega_{\alpha} = 0 \quad \sum_{\alpha=0}^m \Omega_{\alpha} \mathbf{e}_{\alpha} = 0 \quad (2.4)$$

Since Δt physically is the time required for a particle to move from one node to another and is much smaller than the time scale that characterizes the variation of physical variables, and Δt can be taken as a small parameter of order in ε in a perturbation analysis. Using a Taylor series expansion in space and time in Eq. (2.2), the following continuous form of the kinetic equation, which is accurate up to second order in ε , can be obtained,

$$\frac{\partial f_{\alpha}}{\partial t} + \mathbf{e}_{\alpha} \cdot \nabla f_{\alpha} + \varepsilon \left(\frac{1}{2} \mathbf{e}_{\alpha} \cdot \mathbf{e}_{\alpha} \nabla \nabla f_{\alpha} + \mathbf{e}_{\alpha} \cdot \nabla \frac{\partial f_{\alpha}}{\partial t} + \frac{1}{2} \frac{\partial^2 f_{\alpha}}{\partial t^2} \right) = \frac{\Omega_{\alpha}}{\varepsilon} \quad (2.5)$$

Assuming that the distribution function f_i is close to its value at the equilibrium state, f_{α} can be expanded as

$$f_{\alpha} = f_{\alpha}^{(eq)} + \varepsilon f_{\alpha}^{(1)} + O(\varepsilon^2) \quad (2.6)$$

where $f_{\alpha}^{(1)}$ is the leading order perturbation that accounts for the major part of the non-equilibrium part of f_{α} . Substituting Eq. (2.6) into the collision operator Ω_{α} in Eq. (2.5) and performing the Taylor series expansion, one obtains

$$\Omega_{\alpha}(f) = \Omega_{\alpha}(f^{eq}) + \varepsilon \frac{\partial \Omega_{\alpha}(f^{eq})}{\partial f_{\beta}} f_{\beta}^{(1)} \quad (2.7)$$

Substituting Eqs. (2.6-2.7) into (2.5), we find,

$$\Omega_{\alpha}(f^{eq}) = 0 \quad (2.8)$$

This leads to the linearized collision operator:

$$\Omega_{\alpha}(f) = M_{\alpha\beta}(f_{\beta} - f_{\beta}^{eq}) \quad (2.9)$$

where $M_{\alpha\beta} \equiv \frac{\partial \Omega_\alpha(f^{(eq)})}{\partial f_\beta}$ is the coefficient of the collision matrix (Higuera and Jimenez

1989). The following definitions for $M_{\alpha\beta}$ are given by Benzi *et al.* (1992):

- (i) The $[M_{\alpha\beta}]$ is a symmetrical matrix.
- (ii) The general element $M_{\alpha\beta}$ only depends on the angle between the directions of \mathbf{e}_α and \mathbf{e}_β .
- (iii) Collision conserves mass and momentum, so that

$$\sum_{\alpha=0}^m M_{\alpha\beta} = 0, \quad \sum_{\alpha=0}^m \mathbf{e}_\alpha M_{\alpha\beta} = 0, \quad \beta=1, \dots, m \quad (2.10)$$

The matrix elements, $M_{\alpha\beta}$, are numerical parameters, which can be changed at will. If we further assume that the local particle distribution relaxes to an equilibrium state with the same relaxation time τ , it can be obtained that

$$M_{\alpha\beta} = -\frac{1}{\tau} \delta_{\alpha\beta} \quad (2.11)$$

Subsequently the lattice Boltzmann equation with BGK collision (hereinafter referred to as LBGK equation) is obtained:

$$f_\alpha(x + \mathbf{e}_\alpha \Delta t, t + \Delta t) = f_\alpha(x, t) - \frac{1}{\tau} (f_\alpha - f_\alpha^{(eq)}) \quad (2.12)$$

The BGK collision term was first proposed by Bhatnagar, Gross, and Krook (1954).

2.2.2 Derivation of LBE from the Boltzmann Equation

Without the external force, the Boltzmann equation with BGK collision is as follows (Bhatnagar *et al.* 1954):

$$\frac{\partial f}{\partial t} + \xi \cdot \nabla f = -\frac{1}{\lambda} (f - f^{(eq)}) \quad (2.13)$$

where $f = f(x, \xi, t)$ is the particle distribution function in continuum phase space, ξ is the particle velocity, and f^{eq} is the Maxwell-Boltzmann equilibrium distribution function:

$$f^{eq} = \frac{\rho}{(2\pi RT)^{D/2}} \exp\left(-\frac{(\xi - \mathbf{u})^2}{2RT}\right) \quad (2.14)$$

where T is the temperature, R is ordinary gas constant, D is the spatial dimension, and \mathbf{u} is the flow velocity. The macroscopic variables are obtained by taking various moments of the distribution function:

$$\rho = \int f d\xi \quad \rho \mathbf{u} = \int f \xi d\xi \quad (2.15)$$

Equation (2.13) is a partial differential equation and we can use any known numerical methods to solve it. After discretizing Eq. (2.13) in phase space and replacing ξ with \mathbf{e} , if we apply the first order finite difference scheme in time, the first order upwind discretization for the convective term gives

$$\begin{aligned} f_a(\mathbf{x}, t + \Delta t) = f_a(\mathbf{x}, t) - d[f_a(\mathbf{x} + \Delta \mathbf{x}, t + \Delta t) - f_a(\mathbf{x}, t + \Delta t)] \\ - \frac{\Delta t}{\lambda} [f_a(\mathbf{x}, t) - f_a^{(eq)}(\mathbf{x}, t)] \end{aligned} \quad (2.16)$$

where $d = \Delta t \mathbf{e}_a / \Delta \mathbf{x}$, and Δt and $\Delta \mathbf{x}$ are the time step and grid size, respectively.

Choosing $d=1$ and denoting $\tau = \lambda / \Delta t$, Eq. (2.16) becomes standard LBE,

$$f_a(\mathbf{x} + \Delta t \mathbf{e}_a, t + \Delta t) - f_a(\mathbf{x}, t) = -\frac{1}{\tau} (f_a(\mathbf{x}, t) - f_a^{(eq)}(\mathbf{x}, t)) \quad (2.17)$$

Although only the first order schemes are used to obtain the discretized differential equation, as shown by Sterling and Chen (1996), the discretization error has a special

form which can be included into the viscous term, and the solution to Eq. (2.17) gives second order accuracy for the macroscopic variables in time and space.

2.3 From the LBE to the Navier-Stokes (NS) Equations

In order to recover the NS equations from the LBE scheme, we begin with the most commonly used single-relaxation-time (SRT), LBGK model, expressed in Eq. (2.17).

Performing the Taylor series expansion in time and space, we obtain

$$\begin{aligned} \Delta t \frac{\partial f_\alpha}{\partial t} + \Delta t e_{\alpha k} \frac{\partial f_\alpha}{\partial x_k} + \frac{(\Delta t)^2}{2} \left[\frac{\partial^2 f_\alpha}{\partial t^2} + 2e_{\alpha k} \frac{\partial^2 f_\alpha}{\partial t \partial x_k} + e_{\alpha k} e_{\alpha n} \frac{\partial^2 f_\alpha}{\partial x_k \partial x_n} \right] \\ + \frac{1}{\tau} (f_\alpha - f_\alpha^{(eq)}) = 0 \end{aligned} \quad (2.18)$$

In order to derive the NS equations from LBE, the Chapman-Enskog expansion is used. In essence, it is a standard multi-scale expansion (Kervokian and Cole, 1980), with time and space being expanded as

$$\begin{aligned} t = \varepsilon t_1 + \varepsilon^2 t_2 + \dots \quad x = \varepsilon x_1 + \varepsilon^2 x_2 + \dots \\ \frac{\partial}{\partial t} = \varepsilon \frac{\partial}{\partial t_1} + \varepsilon^2 \frac{\partial}{\partial t_2}, \quad \frac{\partial}{\partial x} = \varepsilon \frac{\partial}{\partial x_1}, \end{aligned} \quad (2.19)$$

and the particle distribution function f_α expanded similarly as,

$$f_\alpha = f_\alpha^{(0)} + \varepsilon f_\alpha^{(1)} + \varepsilon^2 f_\alpha^{(2)} + O(\varepsilon^3) \quad (2.20)$$

Substituting equations (2.19-2.20) into Eq. (2.18) results in

$$\begin{aligned} \frac{1}{\tau} (f_\alpha^{(0)} - f_\alpha^{(eq)}) + \varepsilon \left[\Delta t \frac{\partial f_\alpha^{(0)}}{\partial t_1} + \Delta t e_{\alpha k} \frac{\partial f_\alpha^{(0)}}{\partial x_{1k}} + \frac{1}{\tau} f_\alpha^{(1)} \right] \\ \varepsilon^2 \left(\Delta t \left[\frac{\partial f_\alpha^{(1)}}{\partial t_1} + \frac{\partial f_\alpha^{(0)}}{\partial t_2} + e_{\alpha k} \frac{\partial f_\alpha^{(1)}}{\partial x_{1k}} \right] + \frac{(\Delta t)^2}{2} \left[\frac{\partial^2 f_\alpha^{(0)}}{\partial t_1^2} + 2e_{\alpha k} \frac{\partial^2 f_\alpha^{(0)}}{\partial t_1 \partial x_{1k}} + e_{\alpha k} e_{\alpha n} \frac{\partial^2 f_\alpha^{(0)}}{\partial x_{1k} \partial x_{1n}} \right] \right) + \end{aligned}$$

$$\varepsilon^2 \frac{1}{\tau} f_\alpha^{(2)} = 0 \quad (2.21)$$

Arranging terms in ascending orders in ε , we obtain

$$O(\varepsilon^0): \quad f_\alpha^{(0)} = f_\alpha^{(eq)} \quad (2.22)$$

$$O(\varepsilon^1): \quad f_\alpha^{(1)} = -\tau \Delta t \left[\frac{\partial f_\alpha^{(0)}}{\partial t_1} + e_{\alpha k} \frac{\partial f_\alpha^{(0)}}{\partial x_{1k}} \right] \quad (2.23)$$

$$O(\varepsilon^2): \quad f_\alpha^{(2)} = -\tau \Delta t \left[\frac{\partial f_\alpha^{(1)}}{\partial t_1} + \frac{\partial f_\alpha^{(0)}}{\partial t_2} + e_{\alpha k} \frac{\partial f_\alpha^{(1)}}{\partial x_{1k}} \right] \\ - \tau \frac{(\Delta t)^2}{2} \left[\frac{\partial^2 f_\alpha^{(0)}}{\partial t_1^2} + 2e_{\alpha k} \frac{\partial^2 f_\alpha^{(0)}}{\partial t_1 \partial x_{1k}} + e_{\alpha k} e_{\alpha m} \frac{\partial^2 f_\alpha^{(0)}}{\partial x_{1k} \partial x_{1m}} \right] \quad (2.24)$$

Using Eq. (2.23), Eq. (2.24) can be simplified to

$$f_\alpha^{(2)} = -\tau \Delta t \frac{\partial f_\alpha^{(0)}}{\partial t_2} + \left(\frac{1}{2} - \tau \right) \Delta t \left[\frac{\partial f_\alpha^{(1)}}{\partial t_1} + e_{\alpha k} \frac{\partial f_\alpha^{(1)}}{\partial x_{1k}} \right] \quad (2.25)$$

It is noted that the equilibrium distribution should satisfy following constraints:

$$\rho = \sum_{\alpha=1}^m f_\alpha^{(eq)} \quad \rho \mathbf{u} = \sum_{\alpha=1}^m f_\alpha^{(eq)} \mathbf{e}_\alpha \quad (2.26)$$

From equations (2.22) and (2.25) we find

$$f_\alpha = f_\alpha^{(eq)} + \varepsilon f_\alpha^{(1)} + \varepsilon^2 f_\alpha^{(2)} + O(\varepsilon^3) \quad (2.27)$$

Equations (2.25-2.26) lead to following results:

$$\sum_{\alpha=0}^m f_\alpha^{(1)} = \sum_{\alpha=0}^m f_\alpha^{(2)} = 0 \quad (2.28)$$

$$\sum_{\alpha=0}^m f_\alpha^{(1)} \mathbf{e}_\alpha = \sum_{\alpha=0}^m f_\alpha^{(2)} \mathbf{e}_\alpha = 0 \quad (2.29)$$

Summing Eq. (2.23) over the phase space, the continuity equation is recovered to the first order in ε :

$$\frac{\partial \rho}{\partial t_1} + \frac{\partial \rho u_k}{\partial x_{1k}} = 0 \quad (2.30)$$

Multiplying Eq. (2.23) with the discrete particle velocity $e_{\alpha n}$ and summing over α , the momentum equations to the first order in ε are recovered as

$$\frac{\partial \rho u_n}{\partial t_1} + \sum_{l=1}^m e_{\alpha n} e_{\alpha l} \frac{\partial f_{\alpha}^{(0)}}{\partial x_{1l}} = 0 \quad (2.31)$$

In order to obtain the NS equations we need to use the expression for f to the second order of ε . Summing over Eq. (2.25) and enforcing the conditions given by Eqs. (2.28-2.29) lead to

$$\frac{\partial \rho}{\partial t_2} = 0 \quad (2.32)$$

Multiplying Eq. (2.25) with $e_{\alpha n}$ and summing over α , we obtain

$$\frac{\partial \rho u_n}{\partial t_2} = \left(\frac{1}{2\tau} - 1\right) \Delta t \sum_{l=1}^m e_{\alpha l} e_{\alpha n} \frac{\partial f_{\alpha}^{(1)}}{\partial x_{1l}} \quad (2.33)$$

Combining equations (2.30) and (2.32), to the second order of ε , the continuity equation equations is recovered:

$$\frac{\partial \rho}{\partial t} + \frac{\partial \rho u_{\beta}}{\partial x_{\beta}} = 0 \quad (2.34)$$

Combining equations (2.31) and (2.33), to the second order of ε , the momentum equation becomes

$$\frac{\partial \rho u_n}{\partial t} + \sum_{\alpha=1}^m e_{\alpha k} e_{\alpha n} \frac{\partial f_{\alpha}^{(0)}}{\partial x_{1k}} = \left(\frac{1}{2\tau} - 1\right) \Delta t \sum_{\alpha=1}^m e_{\alpha k} e_{\alpha n} \frac{\partial f_{\alpha}^{(1)}}{\partial x_{1k}} \quad (2.35)$$

Changing the notation of k in Eq. (2.23) to m and substituting it into (2.35), we obtain the momentum equations by integrating over the equilibrium distribution of f :

$$\frac{\partial \rho u_n}{\partial t} + \sum_{\alpha=1}^m e_{\alpha k} e_{\alpha n} \frac{\partial f_{\alpha}^{(0)}}{\partial x_{1k}} = \left(\frac{1}{2} - \tau \right) \Delta t \sum_{\alpha=1}^m \left(e_{\alpha k} e_{\alpha n} \frac{\partial^2 f_{\alpha}^{(0)}}{\partial t_1 \partial x_{1k}} + e_{\alpha k} e_{\alpha n} e_{\alpha m} \frac{\partial^2 f_{\alpha}^{(0)}}{\partial x_{1k} \partial x_{1m}} \right) \quad (2.36)$$

Using the definition of $\sum_{\alpha=1}^m e_{\alpha k} e_{\alpha n} f_{\alpha}^{(0)} = \int_{-\infty}^{\infty} c_k c_n f^{(0)} dV_c = \rho u_k u_n + p \delta_{kn}$, one obtains

$$\frac{\partial \rho u_n}{\partial t} + \frac{\partial (\rho u_k u_n)}{\partial x_{1k}} = - \frac{\partial p}{\partial x_{1n}} + \left(\frac{1}{2} - \tau \right) \Delta t \sum_{\alpha=1}^m \left(e_{\alpha k} e_{\alpha n} \frac{\partial^2 f_{\alpha}^{(0)}}{\partial t_1 \partial x_{1k}} + e_{\alpha k} e_{\alpha n} e_{\alpha m} \frac{\partial^2 f_{\alpha}^{(0)}}{\partial x_{1k} \partial x_{1m}} \right) \quad (2.37)$$

In Eq. (2.35), we can see that the viscous terms depend on the leading order term of the non-equilibrium part of distribution function, while equilibrium part only determines momentum flux and pressure terms. The key to the recovering of the NS equation is to find an equilibrium distribution function in the discretized phase space.

2.4 Two-Dimension 9-Velocity Model (D2Q9)

The 9-velocity (or 9-bit) LBE model on the 2-D square lattice (Figure 1.1), denoted as the D2Q9 model, has been widely used for simulating 2-D flows. For athermal fluids, the equilibrium distributions are defined in Eq. (1.4). To recover the NS equations the following identities are noted:

$$\sum_{\alpha=1}^8 w_{\alpha} e_{\alpha m} e_{\alpha n} e_{\alpha k} e_{\alpha j} = \frac{c^4}{9} (\delta_{mn} \delta_{kj} + \delta_{mk} \delta_{nj} + \delta_{mj} \delta_{nk}) \quad (2.38)$$

$$\frac{\partial}{\partial x_{1m}} \frac{\partial}{\partial x_{k\theta}} \sum_{\alpha=1}^8 w_{\alpha} e_{\alpha m} e_{\alpha n} e_{\alpha k} e_{\alpha j} \rho u_j = \frac{c^4}{9} \left(\frac{\partial^2}{\partial x_{1m} \partial x_{1m}} (\rho u_n) + 2 \frac{\partial^2}{\partial x_{1n} \partial x_{1j}} \rho u_n \right) \quad (2.39)$$

Substituting Eq. (1.4) into the second order derivative terms of $f^{(0)}$ in Eq. (2.36) and using the identity (2.39), we obtain

$$\sum_{\alpha=1}^m \left(e_{\alpha k} e_{\alpha n} \frac{\partial^2 f_{\alpha}^{(0)}}{\partial t_1 \partial x_{1k}} + e_{\alpha k} e_{\alpha n} e_{\alpha m} \frac{\partial^2 f_{\alpha}^{(0)}}{\partial x_{1k} \partial x_{1m}} \right) = \frac{c^2}{3} \left[\frac{\partial^2}{\partial x_{1m} \partial x_{1m}} (\rho u_n) + 2 \frac{\partial^2}{\partial x_{1m} \partial x_{1n}} \rho u_n \right] \quad (2.40)$$

Substituting Eq. (2.40) back into Eq. (2.36), we obtain the momentum equations:

$$\frac{\partial \rho u_n}{\partial t} + \frac{\partial \rho u_k u_n}{\partial x_{1k}} = - \frac{\partial p}{\partial x_{1n}} + \left(\tau - \frac{1}{2} \right) \Delta t \frac{c^2}{3} \left[\frac{\partial^2}{\partial x_{1m} \partial x_{1m}} (\rho u_n) + 2 \frac{\partial^2}{\partial x_{1m} \partial x_{1n}} \rho u_n \right] \quad (2.41)$$

where the dynamic shear and bulk viscosities are

$$\mu_s = \mu_b = \frac{c^2}{3} \left(\tau - \frac{1}{2} \right) \Delta t \quad (2.42)$$

It is noted that $\tau > 1/2$ is required to obtain a positive viscosity. In the incompressible flow limit we have

$$\frac{\partial u_{\alpha}}{\partial x_{\alpha}} = 0 \quad (2.43)$$

$$\frac{\partial u_{\beta}}{\partial t} + u_{\alpha} \frac{\partial u_{\beta}}{\partial x_{\alpha}} = - \frac{1}{\rho} \frac{\partial p}{\partial x_{\beta}} + \nu \nabla^2 u_{\beta} \quad (2.44)$$

The differences between LBE and incompressible NS equation are as follows:

1. LBE is a kinetic equation; NS equations are macroscopic equations.
2. The convection terms in LBE are linear; NS equations have nonlinear convection terms.
3. LBE is a discretized kinetic equation; NS equations can take either integral or differential forms.
4. LBE depends on the grid structure; NS is in vector form that is independent on the coordinate and grids.
5. Iterative procedure is usually employed to obtain converged solution when numerically solving the NS equations. LBE does not employ iterative procedure.

6. Generally LBE is designed for time-dependent simulations. NS equations can take either steady state or unsteady form.

2.5 Practical Issues in the Implementation of LBE Method

2.5.1 Boundary Conditions

Two classes of boundaries are often encountered in computational fluid dynamics: open boundaries and the solid wall. The open boundaries include lines (or planes) of symmetry, periodic cross-sections, infinity, and inlet and outlet. At these boundaries, velocity or pressure is usually specified in the macroscopic description of fluid flow.

A difficulty of the LBE method is that the boundary conditions for the distribution functions f are not known. One must construct a suitable condition for $f_{\alpha s}$ based on the macroscopic flow variables.

At the symmetric and periodic boundaries, the conditions for $f_{\alpha s}$ can be given exactly. At the outlet of a computational domain, the condition can usually be given by simple extrapolation. The boundary condition for the velocity at a solid wall can only be given approximately. A popular approach is to employ the bounce-back scheme (Ladd 1994a, 1994b, Behrend 1995). The same idea for the solid wall has been directly extended at inlet to provide the required inlet condition (Cornubert *et al.* 1991, Ziegler 1993, Behrend 1995). While this kind of treatment is an easy extension of the solid wall condition, it also creates a mechanism for the pressure waves from the interior of the computational domain to strike on the inlet boundary and reflect back into the computational domain. Because the pressure wave propagation is typically of an inviscid nature, depending on the nonlinearity and complexity of the specific problem, this may provoke computational instability or prevent the spatial wiggles from being dissipated quickly during the course

of computation. It is desirable to specify a suitable boundary condition for f 's that prevents such a feedback of the pressure wave into the computational domain.

For the evolution of the particle distribution function f near a solid wall, it is noted that the values of f after the collision at the nodes inside the solid wall that is adjacent to the fluid nodes are needed in order to complete the streaming step. Different schemes have been proposed to obtain post-collision values of f at these solid nodes. The bounce-back method is very simple, efficient and easy to implement. On the other hand, the bounce-back scheme is in general only a first order treatment (Ginzbourg and Alder 1994) and can reduce the overall accuracy of the solution. Filippova and Hänel (1998) developed a curved boundary condition treatment using Taylor series expansion in both space and time for f_α near the wall. This boundary condition gives a second order accurate treatment for a curved solid wall. In addition, two other boundary treatments for curved wall, one by Mei *et al.* (1999) and the other by Bouzidi *et al.* (2001) have also been proposed. All of those methods need to treat the boundary condition separately for $\Delta \leq \frac{1}{2}$ and $\Delta > \frac{1}{2}$ in which Δ is the fraction of an intersected node-to-node link in the fluid region. This will cause non-uniformity in f when Δ changes from below $\frac{1}{2}$ to above $\frac{1}{2}$ (or *vice versa*) in dealing with curved boundaries. A unified scheme for curved wall is preferred.

When a solid boundary is moving, the issue is more complicated. A special concern emerges when a solid boundary moves across a node so that it leaves behind a new fluid node on one side of the body and it may transform a neighboring fluid node into a solid node on the other side of the body. The specification of f on the newly generated fluid

node may create spurious pressure oscillations which can degrade the solution at higher Reynolds number.

2.5.2 Reconciliation of Resolution Requirement

High resolution is often needed in the high gradient region, such as the near wall flow of a high Reynolds number flow. This requires a small grid size near the wall. For external flows, the far field boundary often needs to be placed far away from the solid wall while the resolution can be lower. This immediately creates a difficulty for the standard LBE method, since it inherently requires the grid size to be constant. Since the grid size is first chosen to honor the high gradient region near the wall, it requires enormously large numbers of grid point to be able to reach the far field. On the other hand, since the gradients of physical variables are small, the use of fine grids near the far field is a waste of computational effort. In the NS equation-based solvers, this issue is easily resolved by using grid stretching techniques, often in a curvilinear coordinate system. To increase the numerical efficiency while maintaining accuracy in LBE, non-uniform grid has been introduced. He *et al.* (1996) developed a time-dependent interpolation scheme, which increases grid resolution in the high shear rate region. Mei and Shyy (1999) used a curvilinear coordinate system in LBE using a finite difference formulation.

To maintain the inherent advantage of LBE, one prefers to employ the uniform lattice. Thus to reconcile the different requirements of grid resolution, it is desirable to divide computational domain into different regions. In each region, a different lattice space can be used. In practical application, there are two different treatments. One is that the whole computational domain is covered with coarse grids. The patches with fine grids are placed at the desired regions. The other is that there is only one layer of grids at each

region. Such a multi-block approach has been actively employed in the NS equation-based solution methods with both Cartesian and curvilinear coordinates. A similar multi-block strategy in LBE will enhance the capability of the LBE method.

2.5.3 Force Evaluation

The evaluation of the force on a body in a flow field is a common task in fluid mechanics research efforts. This is also the case for computations using the LBE method. Different force evaluation schemes, including momentum exchange (Behrend, 1995, Ladd, 1994a, 1994b) and integration of stress (He *et al.* 1996), have been used to evaluate the fluid dynamic force on a curved body in the context of the LBE method. The method of integration of stress requires knowledge of the details of the surface geometry and can be laborious for 3-D problems. On the other hand, the accuracy of the momentum exchange method needs to be examined at higher Reynolds numbers.

2.5.4 Computational Stability and Dispersion

Computational instability and dispersion are issues of concern in many practical computation. The simplest lattice Boltzmann equation is based on the BGK model, which involves the single-relaxation-time (SRT) approximation. In contrast with the SRT approximation, the multi-relaxation-time (MRT) lattice Boltzmann equation method has been examined by d’Humières (1992) and more recently by Lallemand and Luo (2000). The basic idea is that in the SRT model, the bulk and shear viscosity are both determined by the same relaxation time. The MRT model attempts to relax different modes with different relaxation time. In the MRT method bulk and shear viscosity are determined by different relaxation time, so bulk viscosity can be adjusted independently. It is inevitable to generate pressure wave (acoustic wave) in computation because of initial condition or singularity. Large bulk viscosity is helpful to damp such kind of wave. Numerically, this

could reduce substantially the amount of energy associated with the pressure wave and thus improve the accuracy of the unsteady solution or the convergence toward steady state.

Lallemand and Luo (2000) performed detailed linear analyses on the dispersion, dissipation, and stability characteristics of a generalized lattice Boltzmann equation model (d’Humières, 1992). It was found, through the investigation of simple flow problems, that the multiple relaxation times in the generalized lattice Boltzmann equations leads to better computational stability due to the separation of the relaxations of the various kinetic modes. However, their theoretical study indicates that there is little difference in the performances on the high wavenumber range. Many fluid flow problems possess singularities. Inadequate resolutions in such regions have often resulted in spatial oscillations in the solution. In nonlinear problems, such dispersion errors tend to promote numerical instability. A key issue is whether the MRT model can improve the numerical stability via reduce the dispersion errors (or wiggles) without increasing the computational cost.

2.6 Scope of the Research

A multi-block method will be developed to reconcile the vastly different requirement on the resolution in different flow regions. Derivations for the interface information exchange will be presented to highlight issues associated with both formal order of accuracy and physical conservation laws. The performance of the present multi-block method will be assessed by examining the solution accuracy in various flow problems and by examining the conservation of mass, momentum, and stresses across the block interface.

The force evaluation schemes using momentum exchange for curved boundary will be examined in flow problems involving simple and complex geometry. The momentum exchange method will be shown to offer better accuracy and to be much more robust to use than the stress integration method.

The detailed comparison of computational performance by using the MRT and SRT models will be presented for several flow problems possessing either flow singularity or geometric singularity. A multi-block method in conjunction with MRT model will also be presented in which the interface information exchange is specifically derived for the MRT model.

Finally, various issues related to the computational boundary conditions are examined. The interaction between the inlet boundary and the fluid nodes in the interior of the computational domain will be studied along with a strategy to reduce such interactions. For solid wall boundary condition, a unified expression for treating the solid boundary will be developed and assessed. Special attention will also be paid to further improve the boundary condition for moving walls.

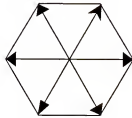


Figure 2.1 A hexagonal lattice

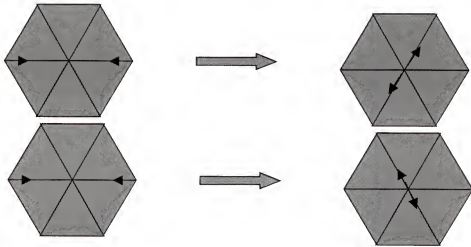


Figure 2.2 Two possible results of a head-on collision in lattice gas

CHAPTER 3 DEVELOPMENT OF MULTI-BLOCK METHODS IN THE LBE METHOD

3.1 Introduction

Accuracy, stability, and efficiency determine whether the application of a particular scheme is successful or not. In the LBE method, the limitation to the numerical efficiency is that the discretization of LBE was constrained on a special uniform lattice. A challenge of the uniform grid is to offer high resolution near a solid body and to place the outer boundary far away from the body without wasting the grid resolution elsewhere. In order to use the regularly spaced lattice while developing the capability to place the outer boundary far away, it is desirable to divide the computational domain into a number of grid blocks so that within each block uniform lattice spacing can be used. Again, such a multi-block approach has been actively employed in the Navier-Stokes equation methods with both Cartesian and curvilinear coordinates.

To enhance the numerical efficiency and accuracy, the non-uniform grid has been introduced into the LBE. He *et al.* (1996) developed a time-dependent interpolation scheme, which increases grid resolution in the high shear rate region. Mei and Shyy (1999) used the curvilinear coordinate system in LBE using finite difference formulation. Bouzidi *et al.* (2001) presented LBE on the two-dimensional rectangular grid. All BGK scheme based methods need some kinds of interpolations during the computation which may increase numerical viscosity and reduce accuracy.

Filippova and Hänel (1998) proposed a local refinement method where the post-collision distribution function passing the interface was rescaled to satisfy the

conservation of mass and momentum and continuity of stresses across the interface joining two grid systems. Patches of fine grids are used in certain regions, for examples, around a solid body. Values of the distribution functions on the coarse grid, which are coming from regions of finer patches, with a large gradient of hydrodynamic variables, are calculated with second-order interpolations in space and time in the boundary nodes of the fine grid.

In the presently developed method the flow field is divided into blocks. In each block, the grid spacing is uniform with desired resolution. An accurate interface treatment between neighboring blocks is derived to ensure the continuity of mass, momentum, and stresses across the interface. Furthermore, a systematic effort has been made to evaluate the performance of the present multi-block method, including both accuracy and efficiency aspects. Several test cases have been employed. A lid-driven cavity flow is computed using a single block with uniform grid and the present multi-block method. The results are compared with published benchmark results. A channel flow with a parabolic velocity profile at the inlet over an asymmetrically placed cylinder at $Re=100$ (based on the average incoming velocity) is computed next using the multi-block method. Finally, flow over NACA0012 airfoil at $Re=500-5000$ is computed. The present study shows that the multi-block strategy can greatly improve the computational efficiency of the LBE method.

After the completion of the present work, two papers were published: one by Lin and Lai (2000), the other by Kandhai *et al.* (2000). In Lin and Lai's method, the coarse base grid covers the entire physical domain, and the finer grid blocks are placed at regions where local grid refinement is desirable. The simulation is first carried out on the base

grid level at a smaller relaxation time, allowing a rapid propagation of boundary information throughout the entire domain. At a later time, the computation of the fine grid variables is initiated. The dependent variables on both grid levels are, then, advanced in time simultaneously with the fine grid boundary conditions obtained from the base grid solution at the grid interface. The method of Kandhai *et al.* (2000) is based on multiple nested lattices with increasing resolution. The discrete velocity Boltzmann equation is solved numerically on each sub-lattice and interpolation between the interfaces is carried out in order to couple the computations in different blocks.

Compared with the above-cited references, in the present method, the different grid size blocks are not overlapped between each other, and blocks are connected only thorough interface. Also details related to the conservative properties and block-to-block coupling are investigated more directly.

3.2 Basics of the Multi-Block Strategy in the LBE Method

To illustrate the basic idea, a two-block system (a coarse and a fine, as shown in Figure 3.1) is considered in the derivation for the interfacial information exchange. The ratio of the lattice spacing between the two-grid system is

$$m = \bar{\alpha}_c / \bar{\alpha}_f \quad (3.1)$$

For a given lattice size $\bar{\alpha}$, the viscosity of the fluid is

$$\nu = (2\tau - 1)\bar{\alpha}_c^2 / 6 \quad (3.2)$$

In order to keep a consistent viscosity, and thus Re , in the entire flow field involving different lattice sizes, the relation between relaxation times, τ_f , on the fine grid, and τ_c , on the coarse grid, must obey the following rule:

$$\tau_f = \frac{1}{2} + m\left(\tau_c - \frac{1}{2}\right) \quad (3.3)$$

To keep the variables and their derivatives continuous across an interface between two different grids, a consistent and accurate relationship for the probability density function in the neighboring grid blocks must be developed. The following summarizes the key elements in the derivation for the information exchange across the interface.

It is noted that

$$f_a(\mathbf{x}, t) = f_a^{(eq)}(\mathbf{x}, t) + f_a^{(neq)}(\mathbf{x}, t) \quad (3.4)$$

where $f^{(neq)}$ is the non-equilibrium part of the distribution function based on which the deviatoric stresses are evaluated. The collision step gives

$$\tilde{f}_a(\mathbf{x}_i, t + \delta t) = (1 - \frac{1}{\tau})f_a(\mathbf{x}_i, t) + \frac{1}{\tau}f_a^{(eq)}(\mathbf{x}_i, t) \quad (3.5)$$

Substituting Eq. (3.4) into Eq. (3.5) leads to

$$\begin{aligned} \tilde{f}_a(\mathbf{x}_i, t + \delta t) &= (1 - \frac{1}{\tau})[f_a^{(eq)}(\mathbf{x}_i, t) + f_a^{(neq)}(\mathbf{x}_i, t)] + \frac{1}{\tau}f_a^{(eq)}(\mathbf{x}_i, t) \\ &= f_a^{(eq)}(\mathbf{x}_i, t) + \frac{\tau - 1}{\tau}f_a^{(neq)}(\mathbf{x}_i, t) \end{aligned} \quad (3.6)$$

Denoting the coarse-grid quantities with the superscript c and fine-grid quantities with the superscript f , the post-collision step gives

$$\tilde{f}_a^{(c)} = f_a^{(eq,c)} + \frac{\tau_c - 1}{\tau_c}f_a^{(neq,c)} \quad (3.7)$$

Similarly,

$$\tilde{f}_a^{(f)} = f_a^{(eq,f)} + \frac{\tau_f - 1}{\tau_f}f_a^{(neq,f)} \quad (3.8)$$

Since the velocity and density must be continuous across the interface between the two grids, from Eq.(1.6), it is seen that

$$f_a^{(eq,c)} = f_a^{(eq,f)} \quad (3.9)$$

To maintain continuity in the deviatoric stresses, in the 2-D case,

$$\tau_{ij} = (1 - \frac{1}{2\tau}) \sum_{a=1}^8 f_a^{(neq)} (e_{ai} e_{aj} - \frac{1}{2} e_a \cdot e_a \delta_{ij}) \quad (3.10)$$

it is required that

$$(1 - \frac{1}{2\tau_c}) f_a^{(neq,c)} = (1 - \frac{1}{2\tau_f}) f_a^{(neq,f)} \quad (3.11)$$

or

$$f_a^{(neq,c)} = m \frac{\tau_c}{\tau_f} f_a^{(neq,f)} \quad (3.12)$$

Substituting Eq. (3.12) into Eq. (3.7) one obtains

$$\tilde{f}_a^{(c)} = f_a^{(eq,c)} + m \frac{\tau_c - 1}{\tau_f} f_a^{(neq,f)} \quad (3.13)$$

Using Eqs. (3.8-3.10), the above becomes

$$\tilde{f}_a^{(c)} = f_a^{(eq,f)} + m \frac{\tau_c - 1}{\tau_f} \frac{\tau_f}{\tau_f - 1} [\tilde{f}_a^{(f)} - f_a^{(eq,f)}] = f_a^{(eq,f)} + m \frac{\tau_c - 1}{\tau_f - 1} [\tilde{f}_a^{(f)} - f_a^{(eq,f)}] \quad (3.14)$$

In transferring the data from the coarse grids to the fine grids, one similarly obtains

$$\tilde{f}_a^{(f)} = f_a^{(eq,c)} + \frac{\tau_f - 1}{m(\tau_c - 1)} [\tilde{f}_a^{(c)} - f_a^{(eq,c)}] \quad (3.15)$$

Equations (3.14-3.15) were first given by Filippova and Hänel (1998). On the interface between two blocks, there are m values of $\tilde{f}_a^{(f)}$ needed for each $f_a^{(eq,c)}$ and $\tilde{f}_a^{(c)}$. Thus, spatial and temporal interpolation procedures for the values of $f_a^{(eq,c)}$ and $\tilde{f}_a^{(c)}$ on the fine-grid lattice are used to complete the evaluation of $\tilde{f}_a^{(f)}$.

3.3 Interface Structure and Computational Procedure

The typical interface structure is shown in Figure 3.1. The line \overline{MN} is the fine block boundary, while the line \overline{AB} is the coarse block boundary. The coarse block boundary is

in the interior of the fine block, and the fine block boundary is in the interior of the coarse block. This arrangement of the interface is convenient for the information exchange between two neighboring blocks. For example, grid Q is an interior lattice node of the coarse block. After the collision step, the values of incoming distribution functions $\tilde{f}_2(t^{n+1}, X_D)$, $\tilde{f}_3(t^{n+1}, X_E)$, and $\tilde{f}_4(t^{n+1}, X_F)$ from boundary nodes D, E, and F, respectively, are needed in order to obtain $f_2(t^{n+1}, X_Q)$, $f_3(t^{n+1}, X_Q)$, and $f_4(t^{n+1}, X_Q)$ at the end of streaming step, since other components of $f_a(t^{n+1}, X_Q)$, ($a=1, 5, 6, 7, 8$) are obtained from advecting the neighboring post-collision values of \tilde{f}_a in the interior nodes of the coarse block. For the same reason, the fine block boundary \overline{MN} is located in the interior of the coarse block. However, on the fine block boundary \overline{MN} , there is no information on the nodes denoted by the solid symbol \bullet in Figure 3.1; it must be obtained through spatial interpolation based on the information at the nodes denoted by the open symbol \circ on the line \overline{MN} . To eliminate the possibility of spatial asymmetry caused by interpolations, a symmetric, cubic spline fitting is used for spatial interpolation of \tilde{f}_a on the fine block boundary,

$$\tilde{f}(x) = a_i + b_i x + c_i x^2 + d_i x^3, \quad x_{i-1} \leq x \leq x_i, \quad i = 1, \dots, n \quad (3.16)$$

where the constants (a_i, b_i, c_i, d_i) are determined by using the continuity of the nodal conditions of f, f', f'' and suitable end conditions (such as zero second derivative for f). We found that it is very important to maintain the spatial symmetry in the interpolation along the interface.

Figure 3.2 shows the flow chart of the computational procedure for the multi-block calculation. It is noted that in addition to the spatial interpolation, there is a need for temporal interpolation on all nodes at the fine block boundary \overline{MN} in order to obtain $\tilde{f}_\alpha(t^{n+\frac{1}{2}}, \overline{MN})$. Here a 3-point Lagrangian formula is used:

$$y(x) = \sum_{k=1}^3 y_k \left(\prod_{\substack{j=1 \\ j \neq k}}^3 \frac{x - x_j}{x_k - x_j} \right) \quad (3.17)$$

3.4 Results and Discussions

Several well-documented flow problems are selected to highlight the performance of the present method. In all cases, the boundary condition for f_α in the solid region near a wall is obtained using the formulations given by Mei *et al.* (1999) for a curved geometry.

3.4.1 Lid-Driven Cavity Flow

The lid-drive cavity flow has been extensively used as a benchmark solution to test the accuracy of a numerical method. In this flow, two singular points at the upper corners of the lid require high resolution to obtain satisfactory stress distribution near the corner points. To assess the LBE results, the benchmark solutions by Ghia *et al.* (1982) are used for comparison.

The computations are carried out using (i) a single-block with uniform lattice (129x129) with the walls placed halfway between lattices, and (ii) a multi-block whose layout is shown in Figure 3.3. For the multi-block case, in the two upper corner regions, the grid resolution is increased by a factor of 4. For $Re=100$, the relaxation time is $\tau_c=0.56$ for the coarse-grid block and $\tau_f=0.74$ for the fine-grid block. The upper wall velocity is $U=0.0156$. The initial condition for density is unity and that for velocity is zero. The streamlines shown in Figure 3.4 are obtained from the single block solution

and the pattern is not discernable from those of the multi-block solution. The positions of the centers of the primary vortices are (0.6154, 0.7391) and (0.6172, 0.7390) for uniform grid and multi-block solutions respectively, compared well with the value (0.6172, 0.7344) from Ghia *et al.* (1982). The u - and v -components of the velocity along the vertical line and horizontal line through the geometry center are shown in Figure 3.5a and Figure 3.5b, respectively. It is seen that while the single block method with 129×129 lattices can capture most of physical variables satisfactorily, the multi-block method can improve the quality of the solution. Figure 3.6 shows the pressure contour from the single-block computation. Because of the singularity at the upper corners, the density contours exhibit noticeable oscillations due to the insufficient resolution near singularities. Figure 3.7 shows the pressure contours obtained from the multi-block solution. Significant improvement in the smoothness of the solution for the pressure field over that of the single block solution is observed.

In an NS solver for incompressible flows, because of the decoupling of thermodynamic pressure and velocity field, it is crucial to maintain the mass conservation of the entire flow domain. This issue becomes more critical when the multi-block method is used (Shyy 1997, Shyy *et al.* 1999). Also for incompressible flows, the pressure is arbitrary up to a constant. Hence coupling the pressure term while maintaining the mass flux conservation is very important. Generally speaking, it is difficult to maintain simultaneously the continuity of mass, momentum, and stresses across the interface between neighboring blocks because interpolations are applied to each dependent variable. In the present multi-block LBE method, the continuities of mass and stresses are ensured through the use of Eqs. (3.14-3.15). The most important

point is that interpolations are only applied to \tilde{f}_i 's along the interface and this automatically ensures the consistency in the transfer of various flux terms across the interface.

To validate the above arguments, pressure, shear stress, mass flux and momentum flux near the block interfaces are examined next. Figure 3.8 shows a local, enlarged view of the pressure contour around an interface corner point indicated by the circle in Figure 3.7. Clearly, the pressure is rather smooth across the interface with the coarse-to-fine grid size ratio of $m=4$. Figure 3.9-Figure 3.11 show the contours of shear stress, mass flux, and momentum flux ρu_x^2 . It is seen that these physical quantities are all smooth across the interface.

To demonstrate this issue more clearly, macroscopic physical quantities on one part of the interface (i.e. line A-B in Figure 3.3) are plotted in Figure 3.12-Figure 3.17. After the streaming step there is no physical value on the interface for the fine grid. Here we use a second order extrapolation to obtain the fine grid value on the interface. Figure 3.12-Figure 3.15 show that mass and momentum fluxes match very well between the fine- and coarse-grid. Figure 3.16 shows the shear stress profile. In most part of the interface the fine- and coarse- grid solutions agree very well with each other. The discrepancy appears near the upper wall. It is noted that for in the fine-grid blocks, the top moving wall is located half-way between two horizontal, fine-grid lattices with a distance of $\Delta_f \tilde{\alpha}_f = 0.5 \tilde{\alpha}_f$. In the coarse-grid block, the distance between the wall to the nearest lattice in the fluid region is $\Delta_c \tilde{\alpha}_c = 0.5 \tilde{\alpha}_f = 0.5 \tilde{\alpha}_c / 4 = 0.125 \tilde{\alpha}_c$ for $m=4$. This mismatch ($\Delta_f \neq \Delta_c$) will result in different errors in the boundary condition for f_i 's. This subsequently affects the accuracy of the shear stress near the corner of the block interface and the wall. The

same problem also appears in Figure 3.17 for pressure. The behavior of the solution, however, can be easily improved by using a set of uniform-sized fine grids for the fluid region near the entire upper wall.

3.4.2 Channel Flow over an Asymmetrically Placed Cylinder at $Re=100$

Schäfer and Turek (1996) reported a study of a laminar flow over a circular cylinder placed asymmetrically inside a channel. The cylinder center to the upper wall distance is 4.2 cylinder radii, and the cylinder center to the lower wall distance is 4.0 radii. In the present LBE computation, two grid sizes are used with the coarse-to-fine lattice spacing ratio $m=4$ and the flow domain is divided into five blocks. The finer grid block is placed around the cylinder as shown in Figure 3.18. The radius of the cylinder, r , equals 20 lattice spacing in the fine block. The total number of lattices in coarse-grid blocks is 8854, and the fine block has $81 \times 81 = 6561$ lattices. The relaxation times for the coarse- and fine- grids are $\tau_c = 0.52$ and $\tau_f = 0.58$, respectively. The average inlet velocity \bar{U} is 0.0666. The channel inlet has a parabolic velocity and is located at 4.0 radii upstream of the cylinder center. A zeroth-order extrapolation for f_α is used at the outlet. The Reynolds number based on the average inlet velocity and the diameter of the cylinder is $Re=100$.

At this Reynolds number, the flow becomes unsteady and periodic vortex shedding is observed. The numerical value of Strouhal number ($St = D/\bar{U}T$) is 0.300 and it agrees very well with the range of values (0.2995-0.305) given by Schäfer and Turek (1996). Here D is the diameter of cylinder and T is the peak-to-peak period of the lift force which is 500 in lattice unit based on the coarse block. An instantaneous streamline plot is shown in Figure 3.18 after the dynamically periodic solution is established. The

variations of the drag and lift coefficients are shown in Figure 3.19. It is noted that $C_D(t)$ has two peaks ($C_{D,\max 1} = 3.23$, $C_{D,\max 2} = 3.22$). A closer examination of $C_L(t)$ reveals that $C_L(t)$ is not symmetric with respect to the x-axis ($C_{L,\max} = 1.01$, $C_{L,\min} = -1.03$). This result is reasonable because the flow is not symmetric with respect to the horizontal line drawn through the center of the cylinder. The mean velocity of the flow passing the upper region of cylinder is lower than that passing the lower region (Schäfer and Turek, 1996). Careful examination of the computational flow field indicates that the local pressure in the upper region is higher than that in the lower region at similar stages of the vortex shedding. There is no report of the existence of two peaks of $C_D(t)$ and asymmetry of $C_L(t)$ in Schäfer and Turek's paper. Only the ranges of $C_{D,\max}$ (3.22-3.24) and $C_{L,\max}$ (0.99-1.01) were given. The present results for $C_{D,\max}$ and $C_{L,\max}$ are well within those ranges.

3.4.3 Steady Flow over the NACA0012 Airfoil

The NACA 0012 airfoil (Figure 3.20) is a popular wing model, which has been used extensively. Flow fields at $Re=500$, 1000, 2000, and 5000 are computed with the multi-block LBE scheme. Figure 3.21 shows the entire computational domain and the schematic of the multi-block arrangement. There are 300 lattices (grids) along the chord in the finest block. The largest grid size ratio between neighboring blocks is 4. At the inlet, upper, and lower boundaries, the equilibrium values are used for f_i 's according to Eq. (1.4) based on the free-stream velocity. At the downstream boundary a zeroth order extrapolation for f_i 's is used.

Figure 3.22 shows the density contour, streamlines and velocity vector of the converged solution at $Re=2000$ and zero angle of attack. To investigate the effect of grid resolution, two sets of grid systems are used for the flow field at $Re=500$: a fine grid system and a coarse grid system (with resolution reduced by a factor of 2 in every block). Figure 3.23 shows the velocity profiles at $(x-x_{LE})/L=0.06$ where L is the chord length and x_{LE} is the location of the leading edge. These two sets of velocity profile agree well with each other, although the fine grid solution appears to have smoother u-component velocity profile, as expected.

Figure 3.24 compares the drag coefficient C_d between the present LBE simulation and those calculated from Xfoil, which is a coupled inviscid and boundary layer flow solver (Drela and Giles 1987). It can be seen that two sets of results agree with each other very well for the range of Reynolds numbers investigated in this study.

It is also noted that at $Re=500$, the present value of $C_d=0.1761$ compares very well with the results reported by Lockard *et al.* (2000): $C_d=0.1762$ obtained using a Navier-Stokes equation-based finite difference method, and $C_d=0.1717$ using Powerflow code developed by EXA Corporation, which is based on the lattice Boltzmann equation method. In addition, the present simulation for the symmetrical flow at $Re=500$ gives a lift coefficient of $|C_L| < 6 \times 10^{-14}$. Lockard reported $C_L=1.15 \times 10^{-7}$ using an NS equation-solver and $C_L=2.27 \times 10^{-4}$ using EXA's Powerflow code. This suggests that the present multi-block code preserve the symmetry very well.

It is worth pointing out that there is a significant saving in the computational cost using the multi-block method in LBE simulations. There are three different sizes of grids used for the NACA0012 airfoil simulation. There are $1025 \times 129 = 132225$ fine grids,

93200 intermediate grids with $m=4$, and 139628 coarse grids (with $m=8$ in reference to the finest grids). This gives a total of about 3.6×10^5 grids in the entire domain. If the fine grid system is used in the entire domain, the number of the grids would be $N_x \times N_y = 5698 \times 1153 \sim 6.57 \times 10^6$ which is 18 times more than in the multi-block case. This represents a saving of 18 times in the memory. Furthermore, since $\delta t = \delta x = \delta y$ in the LBE simulation, one time step in the coarsest grid system ($m=8$) requires 2 time steps in the intermediate grid blocks and 8 steps in the finest grid blocks. The ratio of the computational efforts required to carry out a single-block simulations to that for a multi-block simulation for a given period of physical time would be

$$6.57 \times 10^6 \times 8 / (132225 \times 8 + 93200 \times 2 + 139628) \sim 38.$$

Clearly, more saving can be achieved if more blocks of different sizes are used.

3.5 Conclusions

A multi-block strategy is developed for the lattice Boltzmann method. The interface condition is derived to ensure the mass conservation and stress continuity between neighboring blocks. Favorable computational results are obtained in selected test cases. With efficiency aspects greatly improved, there is a significant potential for the multi-block strategy in the LBE method for practical flow problems.

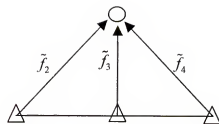
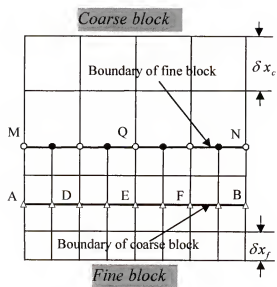


Figure 3.1 Interface structure between two blocks of different lattice spacing.

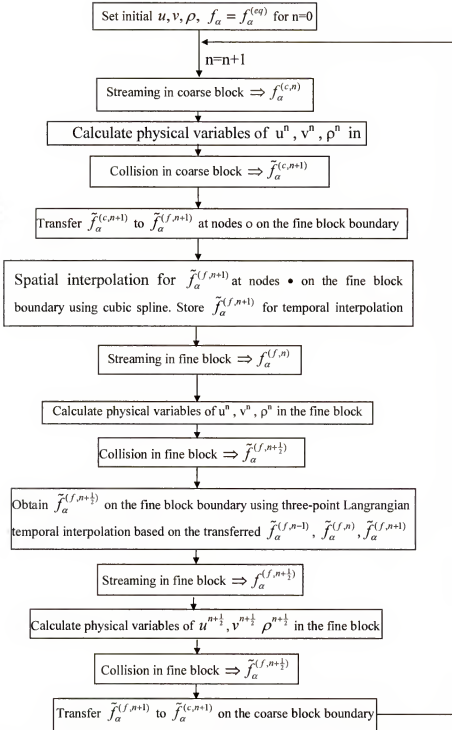


Figure 3.2 Flow chart of the computational procedure in the multi-block method.

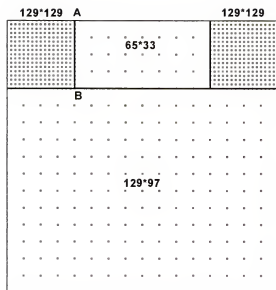


Figure 3.3 Block layout for a 2-D cavity. Lattice spacing is reduced by a factor of 8 for graphical clarity.

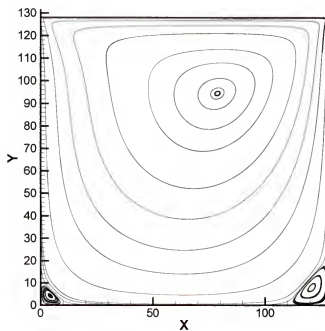


Figure 3.4 Streamlines in the cavity flow at $Re=100$.

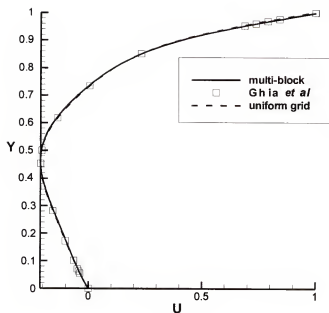


Figure 3.5a Comparison of u -velocity along the vertical line through geometric center.

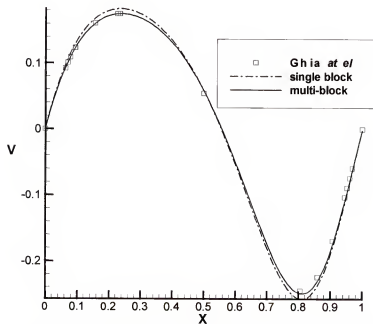


Figure 3.5b Comparison of v -velocity along the horizontal line through geometric center.

Figure 3.5 Comparison of velocity between present results and those by Ghia *et al.* (1982).

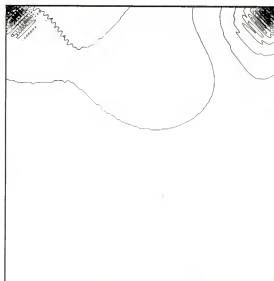


Figure 3.6 Pressure contours in the cavity flow from the single-block LBE simulation.

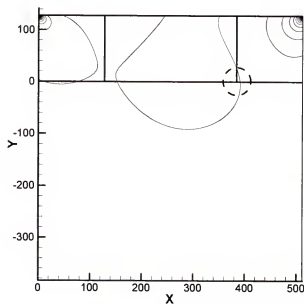


Figure 3.7 Pressure contours in the cavity from multi-block LBE solution. (For the circled region, see Figure 3.8)

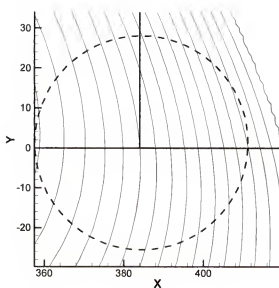


Figure 3.8 Enlarged view of pressure contour in the circled region in Figure 3.7 near the intersection of three blocks. The figure demonstrates that the block interface and corner are well handled.

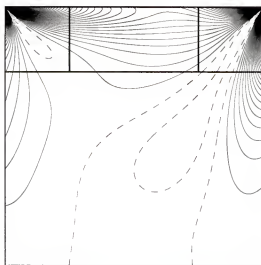


Figure 3.9 Shear stress contour. Solid and dash lines represent positive and negative values, respectively.

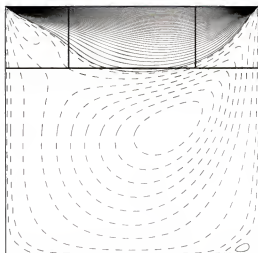


Figure 3.10 Contour of x-component mass flux ρu_x . Solid and dash lines represent positive and negative values, respectively.

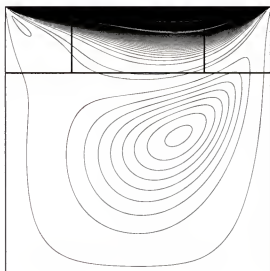


Figure 3.11 Contour of momentum flux in the x-direction ρu_x^2 .

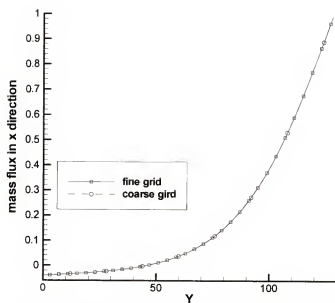


Figure 3.12 The x-component of the mass flux $\rho u_x / (\rho_0 U)$ on the interface AB. In Figure 3.12-Figure 3.15, $\rho_0=1$ and $U=0.0156$.

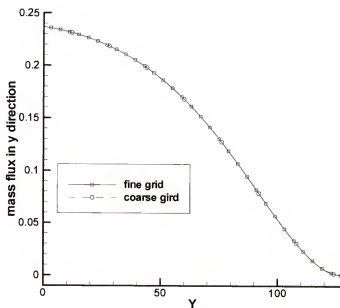


Figure 3.13 The y-component of the mass flux $\rho u_y / (\rho_0 U)$ on the interface AB.

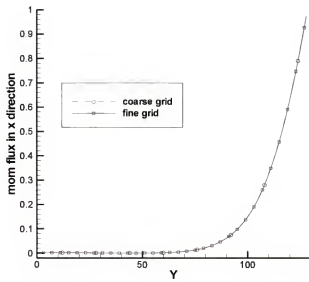


Figure 3.14 The x-component of the momentum flux, $\rho u_x^2 / \rho_0 U^2$, on the interface AB.

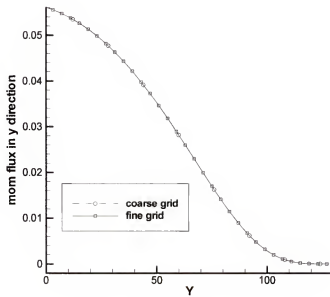


Figure 3.15 The y-component of the momentum flux, $\rho u_x u_y / \rho_0 U^2$, on the interface AB.

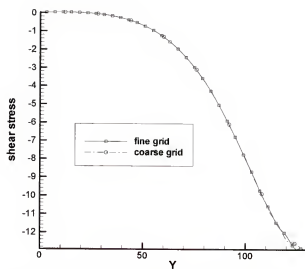


Figure 3.16 Shear stress $\tau_{xy}/(\mu U/H)$ on the interface AB.

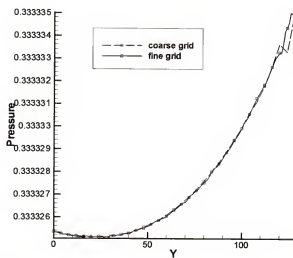


Figure 3.17 Pressure on the interface AB.

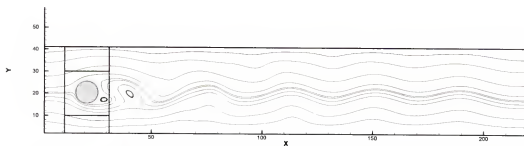


Figure 3.18 Instantaneous streamlines for channel flow over an asymmetrically placed cylinder at $Re=100$.

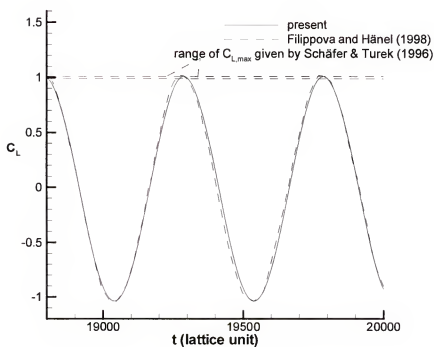
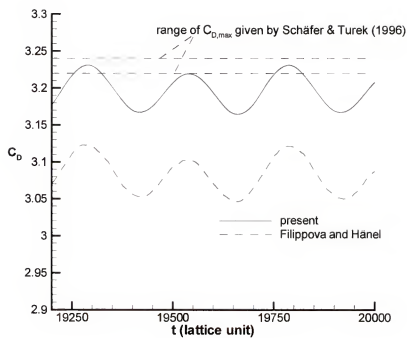


Figure 3.19 Unsteady drag and lift coefficients on the cylinder.

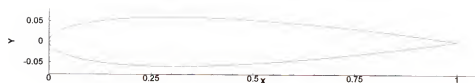


Figure 3.20 NACA 0012 airfoil.

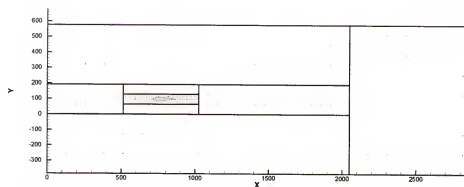


Figure 3.21 Block and lattice layout for flow over NACA 0012. The lattice spacing is reduced by a factor 32 for graphical clarity.

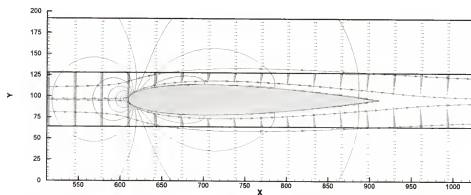


Figure 3.22 Streamlines, pressure contour, and velocity vectors for a uniform flow over NACA 0012 airfoil at $Re=2000$.

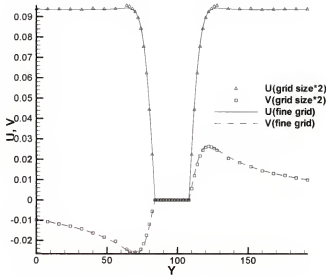


Figure 3.23 Grid-independence test of the velocity profiles near the leading edge at $(x-x_{LE})/L=0.06$ for flow over NACA0012 airfoil at $Re=500$.

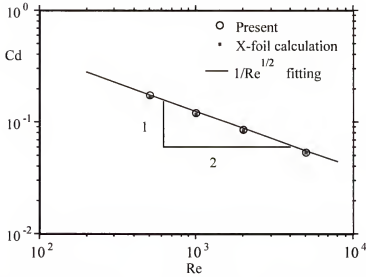


Figure 3.24 Comparison of C_d between the present simulation and Xfoil calculation as a function of Re for flow over NACA0012 airfoil. The straight line is the slope according to the laminar boundary layer theory.

CHAPTER 4 FORCE EVALUATION ON A SOLID BODY IN THE LBE METHOD

4.1 Introduction

4.1.1 Force Evaluation and Related Works

In spite of numerous improvement for the LBE method during the last several years, one important issue that has not been systematically studied is the accurate determination of the fluid dynamic force involving curved boundaries. Needless to say, accurate evaluation of the force is crucial to the study of fluid dynamics, especially in fluid-structure interaction. Several force evaluation schemes, including momentum exchange (Behrend, 1995, Ladd, 1994a) and integration of stress (He *et al.* 1996), have been used to evaluate the fluid dynamic force on a curved body in the context of the LBE method.

He and Doolen (1997) evaluated the force by integrating the total stress on the surface of the cylinder and the components of the stress tensor were obtained by taking respective velocity gradients. Even though a body-fitted grid was used, an extrapolation was needed to obtain the stress in order to correct the half-grid effect due to the bounce-back boundary condition. Filippova and Hänel (1998) developed a second-order accurate boundary condition for curved boundaries. However, the fluid dynamics force on a circular cylinder asymmetrically placed in a 2-D channel was obtained by integrating the pressure and deviatoric stresses on the surface of the cylinder by extrapolating from the nearby Cartesian grids to the solid boundary (Filippova and Hänel, 1998). To gain insight into the method of surface stress integration, it is instructive to examine the variation of the pressure on the surface of a circular cylinder at finite Reynolds number

obtained using LBE method for flow over a column of cylinders (Filippova and Hänel, 1998). Figure 4.1 shows the definition of boundary points, \mathbf{x}_w . Figure 4.2 shows the pressure coefficient, $c_p = (p - p_\infty) / (\frac{1}{2} \rho U^2)$, on the surface obtained by using 2nd order extrapolation where p_∞ is the far upstream pressure. Only those boundary points, \mathbf{x}_w , which are intersected by the horizontal or vertical lattice velocity vectors \mathbf{e}_α , ($\alpha=1, 3, 5$, and 7) are included in Figure 4.2. If the boundary points intersected by the links in the directions of $\mathbf{e}_2, \mathbf{e}_4, \mathbf{e}_6, \mathbf{e}_8$, are included, the variation of c_p would be more noisy. The components of the deviatoric stress tensor show a similar noisy pattern. It is not clear how the noise in the pressure and stresses affect the accuracy of the fluid dynamic force in the stress integration method. While the programming in the extrapolation and integration is manageable in 2-D cases, it is rather tedious in 3-D cases.

Instead of the stress integration method, Ladd (1994) used the momentum exchange method to compute the fluid force on a sphere in suspension flow. In the flow simulation using the bounce-back boundary condition, the body is effectively replaced by a series of stairs. Each segment on the surface has an area of unity for a cubic lattice. The force on each link (half-way between two lattices at \mathbf{x}_f and $\mathbf{x}_b = (\mathbf{x}_f + \mathbf{e}_\alpha \delta t)$ in which \mathbf{x}_b resides in the solid region) results from the momentum exchange (per unit time) between two opposing directions of the neighboring lattices, $[e_\alpha f_\alpha(\mathbf{x}_f, t) - e_{\bar{\alpha}} f_{\bar{\alpha}}(\mathbf{x}_b = \mathbf{x}_f + \mathbf{e}_\alpha \delta t)] / \delta t$ in which $\mathbf{e}_{\bar{\alpha}} = -\mathbf{e}_\alpha$. Whereas the momentum exchange method is very easy to implement computationally, its applicability and accuracy for a curved boundary have not been systematically studied.

To recapitulate, there are two major problems associated with the method of surface stress integration. First of all, the components of stress tensor are often noisy on a curved

surface due to limited resolution near the body and the use of Cartesian grids. The accuracy of such a method has not been addressed in the literature. Secondly, the implementation of the extrapolation for Cartesian components of the stress tensor to the boundary surface and the integration of the stresses on the surface of a 3-D geometry are very laborious in comparison with the intrinsic simplicity of the lattice Boltzmann simulations for flow field.

The problems associated with the method of the momentum exchange are as the following. (1) The scheme as proposed for the case with $\Delta = \frac{1}{2}$ at every boundary intersection x_w . Whether this scheme can be applied to the case with $\Delta \neq \frac{1}{2}$, when, for example, the geometry is not straight, needs to be investigated. (2) As in the case of stress integration method, the resolution near a solid body is always limited and the near wall flow variables can be noisy. If one uses the momentum exchange method to compute the total force, it is not clear what is the adequate resolution to obtain reliable fluid dynamic force on a bluff body at a given (moderate) value of Reynolds number, say, $Re \sim O(10^2)$.

4.1.2 Scope of the Present Work

In what follows, two methods for the force evaluation, *i.e.*, the stress integration and the momentum exchange methods, will be described in detail. The shear and normal stresses on the wall in a pressure driven channel flow will be first examined to assess the suitability of the momentum exchange method when $\Delta \neq \frac{1}{2}$ and analyze the errors incurred. The results on the drag force for flow over a column of circular cylinders using these two methods will be subsequently assessed for the consistency. The drag coefficient at $Re=100$ will be compared with the result of Fornberg (1991) obtained by

using a second order accurate finite difference method with sufficient grid resolution. For flow over an asymmetrically placed cylinder in a channel at $Re=100$, the unsteady drag and lift coefficients match well with literature results. The unsteady flow over The momentum exchange method is further evaluated for 3-D fully developed pipe flow and for a uniform flow over a sheet of spheres at finite Reynolds number. We found that the simple momentum exchange method for force evaluation gives fairly reliable results for 2-D and 3-D flows.

4.2 Methods for Force Evaluation in the LBE Method

4.2.1 Force Evaluation Based on Stress Integration

He and Doolen (1997) evaluated the force by integrating the total stresses on the surface of the cylinder,

$$\mathbf{F} = \int \mathbf{n} \cdot [-p \mathbf{I} + \rho \nu (\nabla \mathbf{u} + (\nabla \mathbf{u})^T)] dA \quad (4.1)$$

In He and Doolen's study, a body fitted coordinate system together with grid stretching was used such that a large number of grids can be placed near the body to yield reliable velocity gradient $\nabla \mathbf{u}$. In general, since \mathbf{u} is not the primary variable in the LBE simulations and the evaluation of \mathbf{u} using Eq.(1.7) based on f_α 's suffers the loss of accuracy due to the cancellation of two close numbers in f_α 's, the evaluation of the derivative $\nabla \mathbf{u}$ will result in further degradation of the accuracy. Fillipova *et al.* (1998) used similar integration scheme to obtain the dynamic force on the body for the force on a circular cylinder except that the deviatoric stresses were evaluated using the non-equilibrium part of the particle distribution function [see Eq. (4.3) below]. However, since Cartesian grid was used, the stress vectors on the surface of the body (with arbitrary Δ) have to be computed through an extrapolation procedure based upon the information

in the flow field. This leads to further loss of accuracy for finite lattice size δx when the shear layer near the wall is not sufficiently resolved.

In Eq. (4.1), the pressure p can be easily evaluated using Eq. (1.8). For D2Q9 and D3Q19 models $c_s^2=1/3$ so that $p=\rho/3$. The deviatoric stress for 2-D incompressible flow

$$\tau_{ij} = \rho \nu (\nabla_i u_j + \nabla_j u_i) \quad (4.2)$$

can be evaluated using the non-equilibrium part of the distribution function

$$\tau_{ij} = (1 - \frac{1}{2\tau}) \sum_{\alpha=1}^8 [f_{\alpha}(\mathbf{x}, t) - f_{\alpha}^{(eq)}(\mathbf{x}, t)] (e_{\alpha i} e_{\alpha j} - \frac{1}{2} e_{\alpha} \cdot e_{\alpha} \delta_{ij}) \quad (4.3)$$

In the above, $f_{\alpha}^{(neq)} = f_{\alpha} - f_{\alpha}^{(eq)}$ is the non-equilibrium part of particle distribution function f_{α} .

For flow over a circular cylinder, a separate set of surface points on the cylinder can be introduced in order to carry out the numerical integration given by Eq. (4.1). The values of the pressure and each of the six components of the symmetric deviatoric stress tensor on the surface points can be obtained using a second-order extrapolation scheme based on the values of p and τ_{ij} at the neighboring fluid lattices. The force is obtained as

$$\mathbf{F} = \int_{\text{surface}} \mathbf{n} \cdot [-p \mathbf{I} + \underline{\underline{\tau}}]_{\text{extrapolated}} dA. \quad (4.4)$$

It is worth commenting here that for the 2-D flow over the cylinder, nearly half of the entire code was taken up by the above force evaluation procedure. Following Fornberg (1991), the drag coefficient over a circular cylinder of radius r is defined as

$$C_D = \frac{|F_x|}{\rho U^2 r} \quad (4.5)$$

4.2.2 Force Evaluation Based on the Momentum Exchange

In order to employ the momentum exchange method efficiently, two scalar arrays, $w(i, j)$ and $w_b(i, j)$ are introduced. A value of 0 is assigned to $w(i, j)$ for the lattice site (i, j) that are occupied by fluid; a value of 1 is assigned to $w(i, j)$ for those lattice nodes inside the solid body. The array $w_b(i, j)$ is set to zero everywhere except for those boundary nodes, \mathbf{x}_b , where a value of 1 is assigned. For a given lattice direction \mathbf{e}_α ($\alpha=1, 2, \dots, 8$ in 2-D), its opposite direction is $-\mathbf{e}_\alpha$ (see Fig. (4.1)). For a given boundary node \mathbf{x}_b inside the solid region with $w_b(i, j)=1$ and $w(i, j)=1$, the momentum exchange with all possible neighboring fluid nodes over a time step $\Delta t=1$ is

$$\sum_{\alpha=1}^{N_d} \mathbf{e}_\alpha [\tilde{f}_\alpha(\mathbf{x}_b, t) + \tilde{f}_{-\alpha}(\mathbf{x}_b + \mathbf{e}_\alpha, t)] [1 - w(\mathbf{x}_b + \mathbf{e}_\alpha)]$$

where $N_d=8$ for 2-D and $N_d=18$ for 3-D cases. Simply summing the contribution over all boundary nodes \mathbf{x}_b belonging to the body, the total force (acted by the solid body on the fluid) is obtained as

$$\mathbf{F} = \sum_{\text{all } \mathbf{x}_b} \sum_{\alpha=1}^{N_d} \mathbf{e}_\alpha [\tilde{f}_\alpha(\mathbf{x}_b, t) + \tilde{f}_{-\alpha}(\mathbf{x}_b + \mathbf{e}_\alpha, t)] [1 - w(\mathbf{x}_b + \mathbf{e}_\alpha)] \quad (4.6)$$

In the momentum exchange method the force \mathbf{F} is evaluated after the collision step is carried out and the boundary value $\tilde{f}_{-\alpha}(\mathbf{x}_b, t)$ has been evaluated (Fillipova *et al.*, 1998, Mei *et al.*, 1999). The momentum exchange occurs during the subsequent streaming step when $\tilde{f}_{-\alpha}(\mathbf{x}_b, t)$ and $f_\alpha(\mathbf{x}_f, t)$ move to \mathbf{x}_f and \mathbf{x}_b , respectively. As mentioned in the introductory section, the effect of variable Δ is not explicitly included, but the effect of Δ is implicitly taken into account in the determination of $\tilde{f}_{-\alpha}(\mathbf{x}_b, t)$ (Fillipova *et al.*, 1998, Mei *et al.*, 1999). The applicability of Eq. (4.6) will be examined and validated.

Clearly, the force is proportional to the number of boundary nodes x_b in the above formulation and the number of the boundary nodes increase linearly with the size of the body in 2-D flow in the LBE method. However, since the force is normalized by $\rho U^2 r$ as in Eq. (4.5) in 2-D, the drag coefficient C_D should be independent of r .

4.3 Results and Discussions

For straight walls, there is no doubt that Eq. (4.1) together with Eq. (1.8) for pressure and Eq. (4.3) for τ_{ij} gives accurate result for the force provided that f_a 's are accurately obtained. To demonstrate the correctness of Eq. (4.6) based on the momentum exchange for an arbitrary Δ , consideration is given first to the pressure driven channel flow (Figure 4.3) for which exact solutions for the velocity and stresses are known. The values of the drag on the column of circular cylinder at 100 for $H/r=20$ computed using these two methods are then compared with the result of Fornberg (1991). The dependence of the drag on the radius r in the momentum exchange method is examined to assess the reliability of this method.

For 3-D flows, the pressure driven flows in a circular pipe have known exact solutions for both the velocity profile and wall shear stresses. The assessment for the momentum exchange method in 3-D flow will be made first in this case. Finally, the momentum exchange method will be evaluated by considering the drag on a sphere due to a uniform flow over a sphere in a finite domain. The details for flow field computation can be found in Mei *et al.* (1999) and Mei *et al.* (2000).

4.3.1 Pressure-Driven 2-D Channel Flow

In the case of the channel flow, the force on the top wall ($y=H$) at a given x location ($i=Nx/2+1$, say) can be evaluated using the momentum exchange method as follows. The

wall is located between $j=N_y$ and N_y-1 (Figure 4.3). The x-component force on the fluid at the wall near the i th node is

$$F_x = [\tilde{f}_6(i, j) + \tilde{f}_2(i-1, j-1)] e_{6x} + [\tilde{f}_8(i, j) + \tilde{f}_4(i+1, j-1)] e_{8x} \quad (4.7a)$$

$$F_y = [\tilde{f}_6(i, j) + \tilde{f}_2(i-1, j-1)] e_{6y} + [\tilde{f}_8(i, j) + \tilde{f}_4(i+1, j-1)] e_{8y} \\ + [\tilde{f}_7(i, j) + \tilde{f}_3(i, j-1)] e_{7y} \quad (4.7b)$$

Since $\tilde{\alpha}=1$, F_x and F_y are, effectively, the total shear and normal stresses, σ_{xy} and σ_{yy} , which include the pressure and the deviatoric stresses, on the fluid element at $y=H$.

Based on Eq. (4.3), the deviatoric component of the fluid shear stresses at $j=N_y-1$ (or $y=N_y-3+\Delta$) and N_y-2 (or $y=N_y-4+\Delta$) can be exactly evaluated based on the non-equilibrium part of the distribution functions f_α 's in the flow field if they are exactly given. A linear extrapolation of the deviatoric shear stresses to $y=H=N_y-3+2\Delta$ yields

$$\tau_{xy,w}^{neq} = \tau_{xy}(j=N_y-1) + \Delta [\tau_{xy}(j=N_y-1) - \tau_{xy}(j=N_y-2)] \quad (4.8)$$

where the superscript “*neq*” denotes that the value is based on using $f_\alpha^{(neq)}$, the subscript w refers to the value on the wall. The deviatoric normal stress, $\tau_{yy,w}^{neq}$, can be similarly found. In a fully developed channel flow, the normal component of the deviatoric stress $\tau_{yy}(y)$ is expected to be zero while the total normal stress $\sigma_{yy}(y)$ is equal to the pressure ($-p$). It needs to be pointed out that this method of evaluating $\tau_{xy,w}^{neq}$ given by Eq. (4.8) for 2-D channel flow is equivalent to the method of the surface stress integration based on the extrapolated pressure and the deviatoric stresses on the solid wall except that no numerical integration on the solid surface is needed.

After the velocity profile $u_x(y)$ is obtained from f_α using Eq. (1.7), the shear stress τ_{xy} on the wall can also be calculated using the near wall velocity profile as,

$$\mu \frac{du_x}{dy} \Big|_{y=H} = \rho \nu \frac{2+\Delta}{1+\Delta} \frac{0-u_x(j=Ny-1)}{\Delta} - \rho \nu \frac{\Delta}{1+\Delta} [u_x(j=Ny-1) - u_x(j=Ny-2)] \quad (4.9)$$

In the above, a linear extrapolation is employed to evaluate the velocity derivative

$$\frac{du_x}{dy} \Big|_{y=H} \text{ at the wall.}$$

Finally, the exact solution for the fluid shear stress on the wall ($y=H$) is

$$\tau_{xy,w}^{exact} = \frac{1}{2} \frac{dp}{dx} H \quad \text{with} \quad H = N_y - 3 + 2\Delta \quad (4.10)$$

based on the parabolic velocity profile or simple control volume analysis. This exact result can be used to assess the accuracy of the aforementioned method for the force evaluation.

In the LBE simulations, the pressure gradient is enforced through the addition of an equivalent body force (He *et al.* 1997, Mei *et al.* 2000) after the collision step. While the velocity field given by the LBE solution can be unique, the pressure field (thus the density field $\rho(x, y)$) can only be unique up to an arbitrary constant. In view of Eq. (4.9), it is difficult to compare the stresses for different cases if $\rho(i, j)$ converges to different values in each case. To circumvent this difficulty, the density field in the channel flow simulation is normalized by $\rho(i=2, j=Ny/2)$ at every time step. This normalization procedure results in $\rho(x, y)=1$ throughout the entire computational domain. It is also applied to the 3-D flows in the circular pipe.

Table 4.1 compares the numerical values of the shear stress for a typical case ($Ny=35$, $dp/dx = -10^{-6}$, and $\tau=0.6$) based on: $\tau_{xy,w}^{exact}$ given by Eq. (4.10), F_x given by Eq. (4.7a), $\tau_{xy,w}^{neq}$ given by Eq. (4.8), and $\mu \frac{du_x}{dy} \Big|_{y=H}$ given by Eq. (4.9). Also listed is the comparison between F_y (Eq. (4.7b)) and $-p$. All computations are carried out with double precision accuracy.

It is noted that $\tau_{xy,w}^{neq}$ is identical to $\tau_{xy,w}^{exact}$ for all values of Δ . Closer examination of the shear stress profile $\tau_{xy}^{neq}(y)$ using Eq. (4.3) across the channel reveals that $\tau_{xy}^{neq}(y)$ is also equal to the exact shear stress profile $\tau_{xy}^{exact}(y)$, which is linear, despite the errors in the velocity profile $u_x(y)$ for all values of Δ . A linear extrapolation, Eq. (4.8), for a linear profile therefore gives the exact wall shear stress. Thus, the exactness of $\tau_{xy,w}^{neq}$ in the LBE simulation of channel flow indicates the reliability of the LBE solution for the stress field $\tau_{ij}^{neq}(x, y)$ using Eq. (4.3). However, as Figure 4.2 indicated, the accuracy of integrating $\tau_{ij}^{neq}(x, y)$ to obtain the fluid dynamic force in non-simple geometries is not clear; this will be further addressed in the following sections.

For $0 < \Delta < 1$, the normal force F_y using Eq. (4.7b) based on the momentum exchange method agrees exactly with the pressure on the wall. This is a rather special quantity since deviatoric component of the force is identically zero. Nevertheless, the method of the momentum exchange does give a reliable value for the normal stress.

For the shear (tangential) force, it is observed from Table 1 that for fixed dp/dx , F_x does not change as Δ increases from 0.01 to 0.99. On the other hand, the exact result,

$\tau_{xy,w}^{exact} = \frac{1}{2} \frac{dp}{dx} (Ny - 3 + 2\Delta)$, increases linearly with Δ . Further computations were carried out over a range of Ny ($=35, 67, 99$, and 131) and τ ($=0.505, 0.51, 0.52, 0.6, 0.7, 0.8, 0.9, 1.0, 1.2, 1.4$, and 1.6). The results indicate that the momentum exchange method gives the shear stress on the top wall as

$$F_x = \frac{1}{2} \frac{dp}{dx} (Ny - 3 + \frac{2}{3}). \quad (4.11)$$

That is F_x is not sensitive to τ and Δ . The error in F_x is zero when $\Delta = 1/3$. The absolute error attains the maximum when $\Delta=1$ which gives the relative error of $\frac{4}{3H}$ for F_x . Although the frequently used momentum exchange method is a natural choice for the force evaluation in conjunction with the bounce-back condition for $\Delta = 1/2$, one must be aware that this method is not exact and the error in the force evaluation using the momentum exchange method depends on Δ and resolution.

Table 4.1 also shows that for the shear stress based on taking the derivative of the velocity, the loss of accuracy is quite significant for small values of Δ (≤ 0.05) for $\tau=0.6$. For other values of Δ (≥ 0.3), the accuracy is comparable with that of F_x . However, as shown in Figure 4.4, the accuracy of $\mu \frac{du_x}{dy} \big|_{y=H}$ based on the near-wall velocity derivative deteriorates as the relaxation time τ increases (from 0.51 to 1.6). To see the cause of the increasing error in $\mu \frac{du_x}{dy} \big|_{y=H}$, Figure 4.5 shows dimensionless wall velocity, u_w/u_c , obtained by a 3-point second-order Lagrangian extrapolation of the near wall $u_x(y)$ as a function of τ . The increasing slip, u_w , on the wall with the increasing relaxation

time, τ , was also observed by Noble *et al.* (1995). It is the result of increasing particle mean free path that causes the deviation of the microscopic based solution from the continuum-based solution. It is clear that the poor performance of $\mu \frac{du_x}{dy} \big|_{y=H}$ is associated with the increasing error in the near wall velocity profile as τ increases. Since the stress tensor $\underline{\tau}$ can be calculated directly from f_α (Eq. (4.3)) without the need for taking velocity derivatives, the force evaluation method based on the evaluation of the velocity gradient in the form of Eq. (4.2) is not recommended.

4.3.2 Steady Uniform Flow over a Column of Cylinders

For a uniform flow over a column of circular cylinders of radius r with center-to-center distance denoted by H (see the left part of Figure 4.9 for illustration), symmetry conditions for f_α 's are imposed at $y = \pm H/2$. Most of the details of flow field simulation can be found in Mei *et al.* (1999). The Reynolds Number is defined by the diameter of the cylinder d as $Re = Ud/\nu$, where U is the uniform velocity at the inlet. It must be noted that for a consistent determination of the force, the upstream boundary must be placed far upstream. A shorter distance between the cylinder and the boundary will result in higher drag. In this study, it is placed at about 20 radii to the left of the center of the cylinder. Reducing the distance between boundary and the cylinder to 12.5 radii while keeping the rest of the computational parameters fixed would increase the drag coefficient by about 1.8% at $Re=100$. The downstream boundary is located about 25-30 radii behind the cylinder to allow sufficient wake development. The simulation is terminated when the following criterion based on the relative L_2 -norm error in the fluid region Ω is satisfied,

$$E_2 = \frac{\left\{ \sum_{(x_i, y_j) \in \Omega} [u(x_i, y_j, t+1) - u(x_i, y_j, t)]^2 \right\}^{1/2}}{\left[\sum_{(y_j, z_k) \in \Omega} u^2(x_i, y_j, t+1) \right]^{1/2}} \leq \varepsilon. \quad (4.12)$$

In this case, $\varepsilon=10^{-6}$ was chosen for both $Re=10$ and 100 .

Following the Fornberg (1991), the drag coefficient over a circular cylinder of radius r is defined as

$$C_D = \frac{|F_x|}{\rho U^2 r} \quad (4.13)$$

Figure 4.6a compares C_D obtained from: momentum exchange method, surface stress integration, and finite difference result of Fornberg (1991) using a vorticity-stream function formulation at $Re=100$, $H/r=20$, for r ranging from 2.8 to 13.2. For $r>8$, both methods of momentum exchange and the stress integration give satisfactory results for C_D in comparison with the value of 1.248 given by Fornberg (1991). The small difference in C_D could be due to the fact that in Fornberg's study, the computational domain is much larger in downstream direction-the downstream boundary condition is imposed at 300 radii behind the cylinder, as opposed to 25-30 radii in present study. This adds credence to the validity of using Eq. (4.6) for evaluating the total force on a body. The values of C_D from the momentum exchange method have a little less scattering than that from the stress integration. Accepting an error of less than 5%, the reliable data for C_D can be obtained, using the momentum exchange method, for $r>5$. That is, 10 lattices cross the diameter of the cylinder are necessary to obtain reliable values of the force. This is consistent with the finding of Ladd (1991). In the range of $5<r<7$, the stress integration method gives more scattered result than the method of momentum exchange.

For smaller radius, *i.e.*, coarser lattice resolution, while both methods give poor results (due to insufficient resolution), the stress integration yields much larger errors.

Figure 4.6b compares C_D obtained from the methods of momentum exchange and the stress integration for $Re=10$. The momentum exchange method seems to give a converged result at larger r (>8). Based on the data for $r>8$, an average value of $C_D \sim 3.356$ is obtained. In contrast, the stress integration method has a larger scattering than the large r result from the momentum exchange method even for $r>8$. Averaging over the result for $r>8$, value, the stress integration gives $C_D \sim 3.319$. The difference between converged results of two methods is about 1%. For r less than or around 5, the scattering in C_D from the stress integration method is much larger than that in the momentum exchange method. The conclusions from the comparisons in Figure 4.7 are as follows: i) both methods for force evaluation can give accurate results; ii) the momentum exchange method gives more consistent drag; iii) in the range of $10 < Re < 100$, a resolution of 10 lattices across the diameter of the cylinder are needed in order to obtain consistent and reliable drag values. In other words, the lattice (grid) Reynolds number Re^* should be less than 10 in the calculations.

It is worth noting that the wall shear stress in the channel flow obtained using the method of momentum exchange has a relative error that is proportional to the resolution across the channel. For a resolution of 10 – 20 lattices across the diameter considered here, the relative error in the drag appears, however, smaller than in the channel flow case. At $Re=100$, with $r>10$, the average value of the drag using the method of momentum method has a 1.7% relative error comparing with Fornberg's data (1991). If the boundary layer thickness is estimated roughly to be $3x2r/Re^{1/2} \sim 6$, there are only

about 6 lattices across the boundary layer over which the velocity profile changes substantially. Based on the insight from the channel flow result, it is possible that the deviatoric shear stresses on the surface of the cylinder that are effectively incorporated in the method of momentum exchange suffer comparable level of error as in the channel flow. The effective error cancellation over the entire surface of the body may have contributed to the good convergence behavior in the drag shown in Figure 4.6a and Figure 4.6b.

4.3.3 Flow over an Asymmetrically Placed Circular Cylinder in Channel with Vortex Shedding

Schäfer and Turek (1996) reported some benchmark results for a laminar flow over a circular cylinder asymmetrically placed inside a channel. The ratio of the center-to-upper-wall is $h_+/r=2.1$ and the ratio of the center-to-lower-wall is $h_-/r=2.0$. In the LBE computation, $r=12.8$ is used. The computational domain is 564×105 . To preserve the geometric similarity, Δ of the upper boundary is set to 0.76 and Δ of the lower wall is 0.2. The relaxation time is $\tau=0.55$. The centerline velocity is 0.095. The channel inlet has a parabolic velocity and is specified at 2.5 radii upstream of the cylinder center; this results in $\Delta=0.2$ at for the inlet boundary. A zeroth-order extrapolation for f_α is used at the exit. The Reynolds number based on the average inlet velocity \bar{U} and cylinder diameter is $Re=100$.

At this Reynolds number, the flow becomes unsteady and periodic vortex shedding is observed. Figure 4.7a and Figure 4.7b compare the lift coefficient, $C_L = \frac{|F_{y_x}|}{\rho \bar{U}^2 r}$, and the drag coefficient C_D (see Eq. (4.13)) with the benchmark results (Schäfer and Turek, 1996). We first note that the numerical value of Strouhal number $St = 2r/(\bar{U}T)$ is 0.300

in which T is the period of the lift curve. This agrees very well with the range of value (0.2995-0.305) given in Schäfer and Turek (1996). We note that there is very small difference in C_L between the momentum exchange method and the surface stress integration method. For the drag coefficient $C_D(t)$, it is interesting to note that although there is about 0.25% difference between the results given by momentum exchange method and the surface stress integration method, both methods of force evaluation give two peaks in the $C_D(t)$ curves. Physically, these two peaks in $C_D(t)$ curve correspond to the a weaker vortex and a stronger vortex behind the cylinder. The difference in the strength of the vortices results from the difference: $h_+/r=2.1$ and $h_-/r=2.0$. There is no report on the occurrence of these two peak in Schäfer and Turek's work. Instead, a range of the $C_{D,max}$ (from 3.22 to 3.24) was given. The values of these two peaks are well within this range. The presence of two peaks may be the sources of the apparently wider range of $C_{D,max}$ than $C_{L,max}$. A further refined computation of the present problem using a multi-block procedure (D. Yu *et al.* 2001) with $r=40$ in the fine grid region yield nearly the same results for $C_D(t)$ and $C_L(t)$.

4.3.4 Pressure Driven Flow in a Circular Pipe

The steady state flow field was obtained (Mei *et al.*, 1999) using D3Q19 model with $\tau=0.52$. Eq. (4.6) is used to evaluate the force on the boundary points along the circumference of the pipe over a distance of one lattice in the axial direction. The resulting axial force, F_x , is, equivalently, the force given by $\tau_w(2\pi r \delta x)$ in which τ_w is the wall shear stress. For a fully developed flow inside a circular pipe, the exact fluid shear stress at the pipe wall is given by the following relation:

$$\tau_w^{exact}(\pi 2r) = \frac{dp}{dx} \pi r^2. \quad (4.14)$$

We examine the normalized axial force,

$$\eta = F_x / \left(\frac{dp}{dx} \pi r^2 \right) \quad (4.15)$$

Figure 4.8 shows the normalized coefficient η over a range of r : 3.5~23.5. Except for $r \leq 5$, η is quite close to 1. It was noticed in Mei *et al.* (2000) that the accuracy of LBE solution for the pipe flow is not as good as that for the 2-D channel flow due to the distribution of values of Δ 's around the pipe. The accuracy of the drag is dictated by the accuracy of the flow field if the force evaluation method is exact. For the pipe flow, the error in F_x results from the inaccuracy in the flow field and the errors in the force evaluation scheme based on momentum exchange (as seen in the previous section for the 2-D channel flow case). For $r > 5$, the largest error in F_x is about 3.5% and it occurs at $r = 15.5$. Again, there is no systematic error in F_x . Given the complexity of the boundary in this 3-D case, the results shown in Figure 4.8 are satisfactory in that it adds further credence to the momentum exchange method for force evaluation.

4.3.5 Steady Uniform Flow over a Sphere

To limit the computational effort, a finite domain: $-H/2 \leq y \leq H/2$ and $-H/2 \leq z \leq H/2$ with $H/r = 10$ is used to compute the flow over a sphere of radius r (Figure 4.9). Two cases are considered. One is to simulate an unbounded flow over the sphere. The other is to simulate flow over a planar array of sphere (all located at $x=0$) with the center of the spheres forming square lattices. In the former case, the boundary conditions at $jy=1$ ($y=H/2$ corresponds to $jy=2$) for f_α 's are given by the following linear extrapolation,

$$f_\alpha(jz, 1, jx) = 2f_\alpha(jz, 2, jx) - f_\alpha(jz, 3, jx) \quad (4.16)$$

The velocity at $jy=2$ is set as

$$\mathbf{u}(jz, 2, jx) = \mathbf{u}(jz, 3, jx). \quad (4.17)$$

Similar treatment is applied at $y=H/2$ and $z=\pm H/2$. In the latter case, symmetry conditions are posed on f_a 's at $jy=1$ using the values of f_a 's at $jy=3$ (see Mei *et al.* 1999) for the 2-D case). At the inlet, a uniform velocity profile is imposed at $jx=1.5$ (half way between the first and second lattices). The upstream boundary is located at 7.5 radii to the left of the sphere center in all simulations.

For flow over a sphere, the drag coefficient is often expressed as

$$C_D = \frac{-F_x}{\frac{1}{2}\rho U^2 \pi r^2} = \frac{24}{\text{Re}} \phi; \quad \text{or} \quad \phi = \frac{-F_x}{6\pi\mu U r} \quad (4.18)$$

where ϕ accounts for the non-Stokesian effect of the drag. For two types of the boundary conditions at $(y=\pm H/2, z=\pm H/2)$, ϕ_{sym} denotes the non-Stokesian correction for the case where the symmetry conditions are imposed at $(y=\pm H/2, z=\pm H/2)$ and ϕ_{unb} denotes the results for the case where the extrapolation for f_a 's is used at $(y=\pm H/2, z=\pm H/2)$ in order to simulate the unbounded flow.

Figure 4.10a shows the non-Stokesian coefficient ϕ_{unb} for $r=3.0, 3.2, 3.4, 3.6, 3.8, 4.0, 5.1, 5.2, 5.4, 5.6$ and 5.8 for $H/r=10$ at $\text{Re} = 10$. The relaxation time is $\tau=0.7$. With this range, the number of the boundary nodes on the surface of the sphere increases roughly by a factor of $(5.8/3)^2 \sim 3.74$; the actual counts of the boundary nodes x_b gives a ratio $2370/546=4.35$. The largest difference is 1.9% between $r=3.0$ and $r=3.2$ which have the least resolution in the series investigated. For a uniform flow over an unbounded sphere, an independent computation using finite difference method based on the vorticity-stream function formulation with high resolution gives a drag coefficient $\phi \sim 1.7986$ at $\text{Re}=10$. The largest difference between this result and the LBE results is 1.36% at $r=3.2$. If the

LBE data for the drag is averaged over the range of r , one obtains $\phi \sim 1.8086$ which differs from 1.7986 by 0.54%. Hence, the LBE solutions based on $r=3.0-5.8$ give quite consistent drag force.

Figure 4.10b shows the non-Stokesian correction factor ϕ_{sym} for a uniform flow over a planar array of spheres for $r=3.0-5.8$ for $H/r=10$ and $Re = 10$. It is important to note that with the improvement of the surface resolution by a factor of 4.35, there is little systematic variation in $\phi_{\text{sym}}(r)$. The largest deviation from the average value, $\phi_{\text{sym,ave.}} \sim 1.963$, is 1.1% at $r=5.0$. It is clear that the LBE solution gives reliable fluid dynamic force on a sphere at $r \sim 3.5$ for a moderate value of Re . The set of data for ϕ_{sym} is inherently more consistent than that for ϕ_{unb} since the boundary symmetry condition can be exactly specified at $(y=\pm H/2, z=\pm H/2)$ while the extrapolation conditions given by Eqs. 4.16-17 do not guarantee the free stream condition at $(y=\pm H/2, z=\pm H/2)$. Yet, both ϕ_{unb} and ϕ_{sym} exhibit remarkable self-consistency from coarse to not-so-coarse resolutions.

4.4 Conclusions

Two methods for evaluating the fluid force in conjunction with the method of lattice Boltzmann equation for solving fluid flows involving curved geometry have been examined. The momentum exchange method is very simple to implement. It is shown in the channel flow simulation that momentum exchange method is not an exact method. The error in the wall shear stress is inversely proportional to the resolution. In 2-D and 3-D flows over a bluff body, it can give accurate drag value when there are at least 10 lattices across the body at $Re \sim 100$. The method of integrating the stresses on the surface of the body gives similar result when there is sufficient resolution but a much larger uncertainty exists when the resolution is limited in comparison with the method of

momentum exchange. In addition, this method requires considerably more efforts in implementing the extrapolation and integration on the body surface in comparison with the method of momentum exchange. The method of momentum exchange is thus recommended for force evaluation on curved bodies.

Table 4.1 Comparison of fluid stresses at $y=H$ in a pressure driven 2-D channel flow with $dp/dx = -10^{-6}$, $Ny = 35$ and $\tau = 0.6$.

Δ	$-\tau_{xy,w}^{exact} \times 10^5$ Eq. (4.10)	$-F_x \times 10^5$ Eq. (4.7a)	$-\tau_{xy,w}^{non,eq} \times 10^5$ Eq. (4.8)	$-\mu \frac{du_x}{dy} \big _{y=H} \times 10^5$ Eq. (4.9)	$-F_y$ Eq. (4.7a)	p
0.01	1.601	1.6333	1.6010	3.5294	0.3333	0.3333
0.02	1.602	1.6333	1.6020	2.5555	0.3333	0.3333
0.03	1.603	1.6333	1.6030	2.2309	0.3333	0.3333
0.04	1.604	1.6333	1.6040	2.0685	0.3333	0.3333
0.05	1.605	1.6333	1.6050	1.9710	0.3333	0.3333
0.1	1.610	1.6333	1.6100	1.7760	0.3333	0.3333
0.2	1.620	1.6333	1.6200	1.6781	0.3333	0.3333
0.25	1.625	1.6333	1.6250	1.6583	0.3333	0.3333
0.3	1.630	1.6333	1.6300	1.6451	0.3333	0.3333
1/3	1.633	1.6333	1.6330	1.6385	0.3333	0.3333
0.35	1.635	1.6333	1.6350	1.6357	0.3333	0.3333
0.4	1.640	1.6333	1.6400	1.6285	0.3333	0.3333
0.5	1.650	1.6333	1.6500	1.6184	0.3333	0.3333
0.6	1.660	1.6333	1.6600	1.6214	0.3333	0.3333
0.7	1.670	1.6333	1.6700	1.6244	0.3333	0.3333
0.8	1.680	1.6333	1.6800	1.6274	0.3333	0.3333
0.9	1.690	1.6333	1.6900	1.6305	0.3333	0.3333
0.95	1.695	1.6333	1.6950	1.6321	0.3333	0.3333
0.99	1.699	1.6333	1.6990	1.6335	0.3333	0.3333

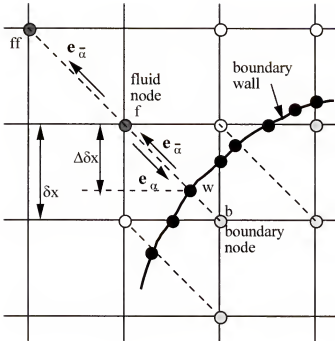


Figure 4.1 Layout of the regularly spaced lattices and curved wall boundary.

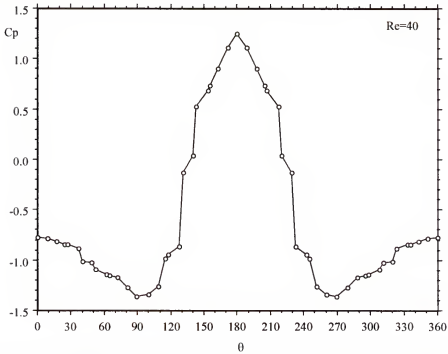


Figure 4.2 Variation of pressure coefficient on the surface of a circular cylinder at $Re=40$, $H/r=10$. The result is obtained using $\tau=0.6$, radius=6.6 lattice unit.

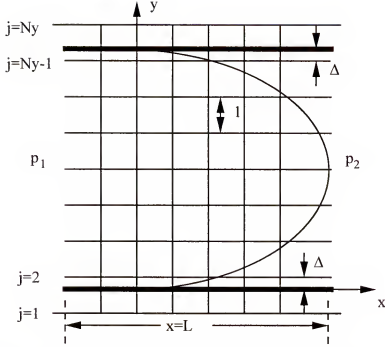


Figure 4.3 Lattice distribution in channel flow simulations with arbitrary Δ .

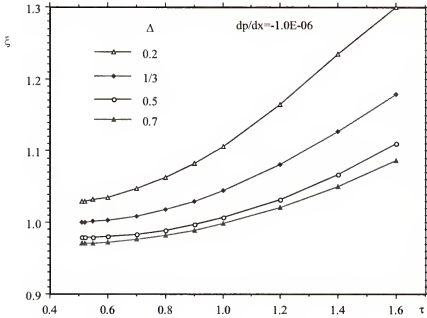


Figure 4.4 Ratio of the wall force evaluated using Eq. (4.9) to the exact value, $\xi = \mu \frac{du_x}{dy}|_{y=H} / [-\frac{1}{2} \frac{dp}{dx} H]$ in 2-D channel flow as a function of τ for $\Delta=0.2, 1/3, 0.5$, and 0.7 .

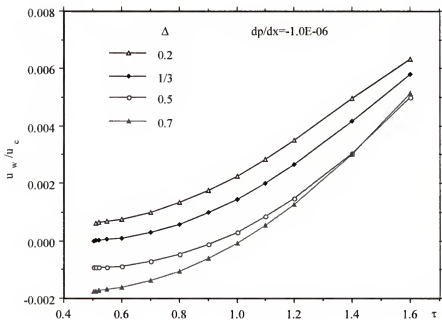


Figure 4.5 Dimensionless wall slip velocity in the 2-D channel flow as a function of τ for $\Delta=0.2, 1/3, 0.5$, and 0.7 .

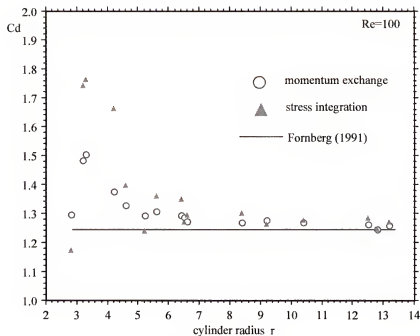


Figure 4.6a.

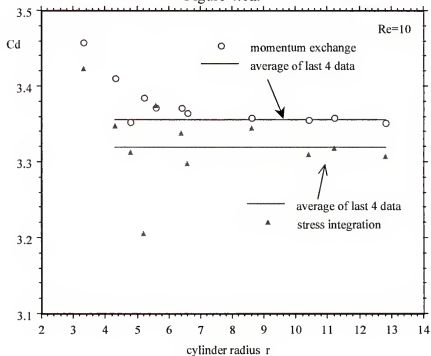


Figure 4.6b

Figure 4.6 Drag coefficient for a uniform flow over a column of cylinder over arange of radius r a) $Re=100$ and b) $Re=10$.

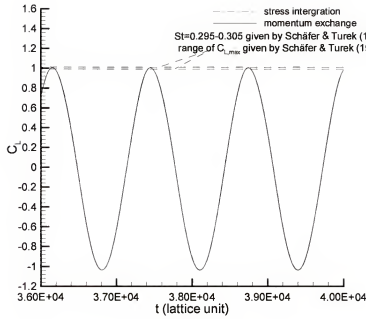


Figure 4.7a

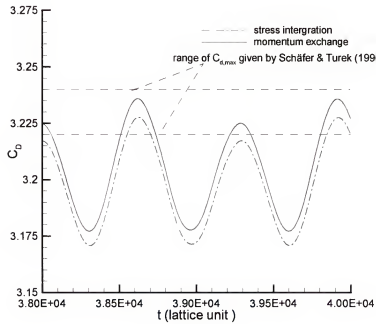


Figure 4.7b

Figure 4.7 Comparison of the lift coefficient (Figure 4.7a) and drag coefficient (Figure 4.7b) with the benchmark results given in Schäfer and Turek (1996).

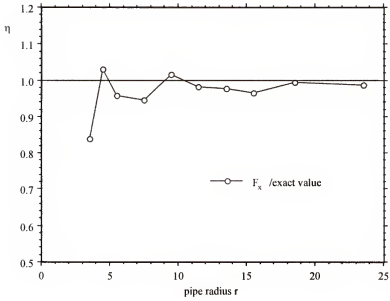


Figure 4.8 Ratio of the tangential force F_x on the pipe to the exact value ($\frac{dp}{dx} \pi r^2$) over a range of pipe radius r .

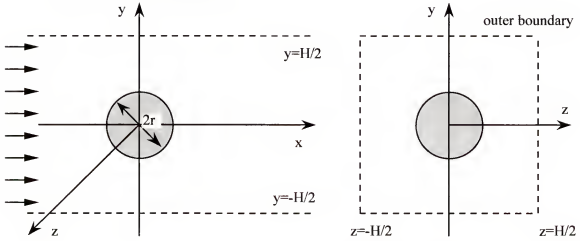


Figure 4.9 Schematic for uniform flow over a sphere.

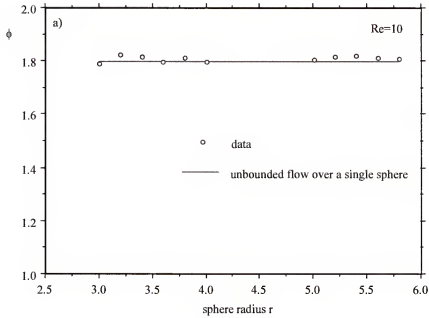


Figure 4.10a Simulation for a single sphere in an unbounded field

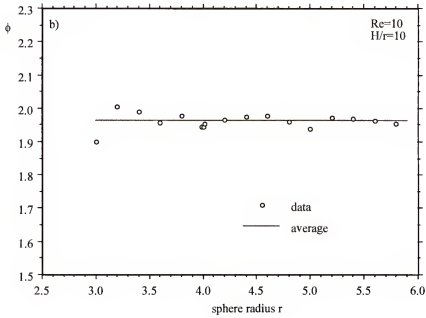


Figure 4.10b Simulation for flow over a planar array of spheres.

Figure 4.10 Variation of the non-Stokesian correction factor with sphere radius at $Re=10$.

CHAPTER 5 MULTI-TIME-RELAXATION MODELS IN THE LBE METHOD

5.1 Introduction

In Chapters 2 and 3, the single-relaxation-time (SRT) model was focused on. In attempting to obtain solutions for high Reynolds number flows using the LBE method, It was found that the solution field for (p, u, v) often exhibit spatial oscillations in regions of large gradients such as stagnation point and sharp convex corners. Especially near a sharp convex corner, because the pressure and the vorticity are singular locally, a large gradient in the density or pressure field exists. Since there usually is insufficient resolution near the corner, the large gradient is often accompanied by spatial oscillations. Depending on the geometry, such spatial oscillation can propagate into the flow to contaminate the macroscopic variables in a large region of interest. The spatial oscillation often adversely affect the computational stability and convergence rate.

Recently, Lallemand and Luo (2000) performed detailed analyses on the dispersion, dissipation, and stability characteristics of a generalized lattice Boltzmann equation model proposed by d’Humières (1992). It was found that by the use of multiple relaxation times in the generalized lattice Boltzmann equations, better computational stability can be achieved over the standard LBGK scheme due to the separation of the relaxations of the various kinetic modes in the generalized lattice Boltzmann equation model--hereinafter referred as the multi-relaxation-time (MRT) model. It was also found in Lallemand and Luo (2000) through the linearized analysis on the MRT model for various simple flows that the MRT model gives the same results, to the second order

accuracy, as the SRT LBGK model does. It seems that these two models are equivalent in the long wavelength limit for macroscopic variable of interest and the difference is a high order effect based on their linear analysis. Such high order differences, however, can be hardly detected in simple linear flows.

Many fluid flow problems possess mathematical singularities. Since a singularity often affects numerical solutions in high wavenumbers, it is expected that the results of the MRT model be noticeably different from that of the SRT model, at least locally near the geometric singularity. For convection-dominated problems, such local difference in the solution behavior can also lead to difference in the solutions over a larger scale. It is insightful to investigate how the solution based on the MRT model behaves in such flows in comparison with the standard LBGK model.

In this chapter, detailed comparison of the performance of these two LBE models for various flows with geometric and flow singularities are provided. A brief background on the MRT model will be described first. Computational results for the pressure, viscous stresses, vorticity, and velocity in regions of large gradient will be compared between the MRT and SRT models under otherwise identical computational and physical parameters for: 1) Stokes first problem, 2) steady uniform flow over a cascade of zero-thickness, finite length flat plates, 3) steady uniform flow over a cascade of finite-thickness, semi-infinite length plates, and 4) steady lid-driven cavity flow. The flow in the Stokes first problem is singular at $t=0$. The flow in a lid-driven cavity has two corners at the intersection of the moving and stationary walls in which the viscous stresses have non-integrable singularities. The flows over a plate and a step have singularities in the pressure and stresses, but they are weaker than in the lid-driven cavity flow. These flows

with varying degree of singularities allow for a detailed assessment of the two LBE models. As will be demonstrated, the MRT model performs better in flows involving large gradients than the SRT LBGK model. In all the simulations, the initial density is set to be $\rho_0=1$. The results for the density (and thus pressure) are presented only in terms of the deviation from ρ_0 or some upstream reference value. The results of the SRT model are obtained by running the same MRT code with $s_2=s_3=s_5=s_7=s_8=s_9=1/\tau$. Obviously, the relative performance between different LBE models depends on many factors including the solution characteristics, types of variables under investigation, and grid resolution. No exhaustive comparison will be made. Instead, we have chosen reasonable grid size in all cases to contrast the behavior of the two models.

5.2 Multi-Relaxation-Time (MRT) Model

In d'Humières (1992), a new set of variables $\underline{R}=(\rho, e, \varepsilon, j_x, q_x, j_y, q_y, p_{xx}, p_{xy})^T$ are introduced and \underline{R} is related to the set of $\underline{F}=(f_0, f_1, f_2, f_3, f_4, f_5, f_6, f_7, f_8)^T$ as follows,

$$\underline{R} = \begin{pmatrix} \rho \\ e \\ \varepsilon \\ j_x \\ q_x \\ j_y \\ q_y \\ p_{xx} \\ p_{xy} \end{pmatrix} = \begin{pmatrix} 1 & 1 & 1 & 1 & 1 & 1 & 1 & 1 & 1 \\ -4 & -1 & 2 & -1 & 2 & -1 & 2 & -1 & 2 \\ 4 & -2 & 1 & -2 & 1 & -2 & 1 & -2 & 1 \\ 0 & 1 & 1 & 0 & -1 & -1 & -1 & 0 & 1 \\ 0 & -2 & 1 & 0 & -1 & 2 & -1 & 0 & 1 \\ 0 & 0 & 1 & 1 & 1 & 0 & -1 & -1 & -1 \\ 0 & 0 & 1 & -2 & 1 & 0 & -1 & 2 & -1 \\ 0 & 1 & 0 & -1 & 0 & 1 & 0 & -1 & 0 \\ 0 & 0 & 1 & 0 & -1 & 0 & 1 & 0 & -1 \end{pmatrix} \begin{pmatrix} f_0 \\ f_1 \\ f_2 \\ f_3 \\ f_4 \\ f_5 \\ f_6 \\ f_7 \\ f_8 \end{pmatrix} = \underline{M} \underline{F} \quad (5.1)$$

where \underline{M} is the 9x9 matrix transforming \underline{F} to \underline{R} . In the vector \underline{R} , ρ is the fluid material density, e is the energy, ε is related to the square of the energy, j_x and j_y are the momentum density (or mass flux), q_x and q_y correspond to the energy flux, and p_{xx} and p_{xy} correspond to the diagonal and off-diagonal component of the viscous stress tensor. One

of the inherent disadvantage of the SRT LBGK model is that all variables are relaxed in the same manner as given by Eq. (1.10a). In lieu of Eq. (1.10a), the collision procedure of the MRT model is carried out as follows,

$$\tilde{e} = e - s_2(e - e^{eq}), \quad (5.2a)$$

$$\tilde{\varepsilon} = \varepsilon - s_3(\varepsilon - \varepsilon^{eq}), \quad (5.2b)$$

$$\tilde{q}_x = q_x - s_5(q_x - q_x^{eq}), \quad (5.2c)$$

$$\tilde{q}_y = q_y - s_7(q_y - q_y^{eq}), \quad (5.2d)$$

$$\tilde{p}_{xx} = p_{xx} - s_8(p_{xx} - p_{xx}^{eq}), \quad (5.2e)$$

$$\tilde{p}_{xy} = p_{xy} - s_9(p_{xy} - p_{xy}^{eq}) \quad (5.2f)$$

where \sim denotes the post-collision state and the equilibrium values were chosen to be

$$e^{eq} = -2\rho + 3(u^2 + v^2), \quad (5.3a)$$

$$\varepsilon^{eq} = \rho - 3(u^2 + v^2), \quad (5.3b)$$

$$q_x^{eq} = -u, \quad (5.3c)$$

$$q_y^{eq} = -v, \quad (5.3d)$$

$$p_{xx}^{eq} = u^2 - v^2, \quad (5.3e)$$

$$p_{xy}^{eq} = uv \quad (5.3f)$$

Before the streaming step, Eq. (1.10b) is solved. One needs to transform the post-collision values, $\tilde{\underline{R}}$, back to $\tilde{\underline{F}}$ by using

$$\tilde{\underline{F}} = \underline{\underline{M}}^{-1} \tilde{\underline{R}} \quad (5.4)$$

In practice, Eq. (5.4) can be combined with Eq. (5.2) to obtain a single expression

$$\tilde{\underline{F}} = \underline{F} - \underline{M}^{-1} \underline{S}(\underline{R} - \tilde{\underline{R}}) \quad (5.5)$$

where \underline{S} is the diagonal matrix:

$$\underline{S} = \text{diag}(0, s_2, s_3, 0, s_5, 0, s_7, s_8, s_9). \quad (5.6)$$

The streaming step in the MRT model is carried out exactly in the same manner for each component as in the standard LBGK model based on Eq. (1.10b).

In Lallemand and Luo (2000), it was shown that for the MRT model to give the same shear viscosity as given by Eq. (1.11) for the SRT model, one needs to set

$$s_8 = s_9 = 1/\tau. \quad (5.7)$$

It is more flexible to chose the rest of the relaxation parameters: s_2 , s_3 , s_5 , and s_7 . In general, these four parameters can be chosen to be slightly larger than 1. In our study, we set $s_2 = s_3 = s_5 = s_7 = 1.2$ for simplicity. Very little difference is observed in the flow field if a different value, say 1.1, is used for (s_2, s_3, s_5, s_7) . It is worth commenting here that by setting $s_2 = s_3 = s_5 = s_7 = s_8 = s_9 = 1/\tau$, the SRT model is recovered.

5.3 Results and Discussions

5.3.1 Stokes First Problem

For an infinitely long wall to move impulsively with a velocity U at $t=0^+$, the exact solution for the wall shear stress is given by

$$\tau_{xy,w} = -\frac{\mu U}{\sqrt{\pi \nu t}} \quad (5.8)$$

where ν is the dynamic viscosity of the fluid. Figure 5.1 shows the relative error of the LBE solutions for the wall shear stress,

$$E = \frac{|\tau_{xy,w}^{LBE} - \tau_{xy,w}^{exact}|}{|\tau_{xy,w}^{exact}|}. \quad (5.9)$$

The results are obtained using the relaxation time $\tau=1/s_8=0.55$. Near $t=0$, there is insufficient enough spatial resolution for the Stokes layer of the thickness $\sqrt{\nu t}$. Hence as illustrated in Figure 5.1 substantial oscillations are present near $t=0$. Clearly, the error in the MRT model is smaller than the SRT error for $t<100$ when the near-wall velocity gradient is large. Eventually, the effect of singularity diminishes and the two solutions approach each other.

5.3.2 Flow over a Cascade of Zero-Thickness, Finite Length Flat Plate

A schematic of the flow is shown in the insert of Figure 5.2. the symmetry condition is imposed at $y=\pm H$. The plate is placed half-way between two grid lines so that the conventional bounce-back condition can be used to update the wall condition for f_α 's. A zeroth-order extrapolation is used at the downstream exit plane for f_α 's. A constant uniform velocity condition is imposed at the inlet, $x/L=-2$. The plate length is 40 in lattice unit (by taking $\delta x=1$). The relaxation time controlling the shear viscosity is set to be $\tau=0.512$ and the Reynolds number based on the length is $Re=UL/\nu=1000$. The free stream velocity is thus $U=0.1$ and $H/L=2$ so that there 80 lattices from the plate to the symmetry line.

Figure 5.2 compares the density deviation, $\rho-1$, as a function of y at $x/L=0.0125$, which is half grid away from the leading edge, based on both the MRT and SRT models under otherwise identical conditions. Due to the singularity in the flow at the leading edge, it is inevitable to have large gradients in pressure, stresses, and vorticity near the leading edge at high Re . When there is insufficient numerical resolution, an unphysical spatial oscillation develops near the leading edge. However, the MRT model is seen to be much more effective in suppressing the spatial oscillation for ρ or p near the leading

edge. Figure 5.3 compares $\rho-1$ as a function of y at $x/L=0.5125$ under the same condition. Surprisingly, the solution based on the SRT model still possesses a substantial level of spatial oscillations even in the middle of the plate for the whole cross-section while the solution from the MRT model has become sufficiently smooth. Figure 5.4 shows the viscous normal stress, τ_{xx} , normalized by $\mu U/L$, as a function of y at $x/L = 0.5125$. Similar level of oscillations is observed in the SRT based solution. In this work, the viscous stresses are obtained using the non-equilibrium part of the distribution function as,

$$\tau_{ij} = (1 - \frac{1}{2\tau}) \sum_{\alpha=1}^8 [f_{\alpha}(x, t) - f_{\alpha}^{(eq)}(x, t)] (e_{\alpha i} e_{\alpha j} - \frac{1}{2} e_{\alpha} \cdot e_{\alpha} \delta_{ij}) \quad (5.10)$$

Hence, no finite difference is employed for the evaluation of the viscous stresses. Figure 5.5 compares the dimensionless viscous shear stress, τ_{xy} , as a function of y at $x/L = 0.5125$. Again, the oscillations in the SRT based solution are noticeable outside the viscous boundary layer.

To develop a further, quantitative understanding of the performance of the two models for flow over a flat plate, the streamwise variation of various macroscopic quantities near the plate $y/L = 0.0125$, which is half-grid above the plate, are also examined. Figure 5.6 shows the variation of the pressure coefficient

$$C_p = \frac{p - p_{\infty}}{\rho_0 U^2 / 2}, \quad (5.11)$$

at $y/L=0.0125$ as a function of x for solutions based on these two models where p_{∞} is the pressure at the centerline of the inlet. It is noted that the singularity at $x=0$ resulted in oscillation in C_p for about 4-5 grid points after the leading edge in the MRT model. However, C_p in the SRT-based solution continues to oscillate across the entire plate.

Figure 5.7 shows variation of the viscous normal stress, τ_{xx} , normalized by $\mu U/L$, at $y/L = 0.0125$. The superiority of the MRT model over the SRT model can be clearly observed in regions before and after the leading edge. Figure 5.8 compares the dimensionless wall vorticity, $\partial u/\partial y$, normalized by U/L , between the two models. Little oscillation is observed for the MRT based solution while the SRT based solution continues to show oscillatory behavior up to $x/L = 0.4$, which cannot be considered as the local region of the leading edge.

5.3.3 Lid-Driven Cavity Flow

The insert in Figure 5.9 shows the coordinate system for the flow inside the cavity. The first line of the grid in the fluid region is at a distance $\Delta\delta x$ from the wall. In this study, $\Delta = 0.3$ is used. The boundary treatment is based on that given in Mei *et al.* (2000) for curved geometries. The height of the cavity is $H/\delta x = 64 + 2\Delta$. With $\tau = 0.52$ and $Re = 1000$, the velocity of the moving wall needs to be $U = 0.1032$.

The velocity field is discontinuous at the two corners on the moving wall. Thus the flow singularity is stronger than in the previous two cases where the velocity is continuous near the convex corner. Figure 5.9 compares the x-component velocity as a function of y at $x/H = 0.00464$ which is on the first grid away from the left vertical wall. Oscillations are observed in both SRT-based and MRT-based velocity profiles due to insufficient resolution for the singularity. However, the oscillation in the MRT solution has smaller amplitude and is limited to a region of 5-6 grids. The oscillation in the SRT solution has larger amplitude and propagates further into the flow field. Figure 5.10 shows the vertical component of the velocity as a function of y at $x/H = 0.00464$. Again, the SRT solution has a much larger amplitude and larger region of the oscillation. Figure

5.11 compares the velocity profiles of the x -component of the two solutions at the centerline ($x/H=0.5$) in the lower half of the cavity with a finite difference solution based on the vorticity-stream-function formulation. It is worth noting that the MRT-based solution is noticeably more accurate than the SRT-based solution even in regions where one considers far away from the singularities.

As a final comment, by taking advantage of many zero elements in $\underline{\underline{M}}^{-1}\underline{\underline{S}}$ and recognizing various common factors in the expressions for the vector $\underline{\underline{M}}^{-1}\underline{\underline{S}}(\underline{\underline{R}} - \underline{\underline{R}}^*)$, the algorithm for the collision step in the MRT model can be coded quite efficiently. For the entire computation of the collision, streaming, and the evaluation of macroscopic variables, the code for the MRT model takes only about 10% more CPU time per time step than an SRT code does. However, this extra 10% work is greatly compensated by the improved convergence of the MRT model in suppressing efficiently the transient oscillation associated with the high-frequency pressure (acoustic) waves, the much improved quality of the results, and the reduced demand for higher resolution.

5.4 Implementation of MRT Model in the Multi-Block Method

In Chapter 3, a multi-block method has been developed for the single-relaxation-time (SRT) model in the LBE method. The scheme for information transfer was derived to ensure the continuity of mass, momentum, and stress across the interface between the coarse and fine blocks.

In the preceding section, it has been shown that the MRT model can reduce pressure oscillation in the solution. A recent study for the 3-D MRT shows that it can improve the stability in computation (d'Humieres *et al.* 2002).

In what follows, a scheme for data exchange is presented for the multi-block MRT model and computational assessments are given.

5.4.1 Basics of the Multi-Block Strategy for MRT Model

In Chapter 3, a multi-block method was developed based on consistency of viscous coefficients on different blocks, the mass, momentum conservation across the interface, and continuity of stress at the interface. Consistency of viscous coefficients requires that the three relaxation time s_2 , s_8 , s_9 need to be rescaled according the same rule (Eq. (3.3)) in Chapter 3. They are the parameters determined the viscosity of the fluid. s_2 is relaxation time for the energy mode, and s_3 , s_5 , and s_7 are relaxation times for energy square, and energy fluxes. Because s_2 is rescaled, it is required that s_3 , s_5 , and s_7 are also need to be rescaled. Thus all the relaxation times are need to be rescaled. The mass and momentum conservation require $f_\alpha^{(eq)}$ to be kept unchanged across the interface and stress continuity requires that $f_\alpha^{(neq)}$ to be rescaled at the interface. For the MRT model to be incorporated in the multi-block method, a similar strategy for the transferring of information at the interface needs to be developed. However there is no explicit expression for $f_\alpha^{(eq)}$ in the MRT model. The values of $(e, \varepsilon, q_x, q_y, p_{xx}, p_{xy})^{(eq)}$ are known and relationship of these variables to velocity and density are given by Eq. (5.3). To implement the multi-block method base on the MRT strategy, the relations between $f_\alpha^{(eq)}$ and $(\rho, e, \varepsilon, j_x, q_x, j_y, q_y, p_{xx}, p_{xy})^{(eq)}$ must be obtained.

Substituting $f = f_\alpha^{(eq)}$ into Eq. (5.1), one obtains

$$\begin{pmatrix} \rho \\ e \\ \varepsilon \\ j_x \\ q_x \\ j_y \\ q_y \\ p_{xx} \\ p_{xy} \end{pmatrix}^{(eq)} = \begin{pmatrix} 1 & 1 & 1 & 1 & 1 & 1 & 1 & 1 & 1 \\ -4 & -1 & 2 & -1 & 2 & -1 & 2 & -1 & 2 \\ 4 & -2 & 1 & -2 & 1 & -2 & 1 & -2 & 1 \\ 0 & 1 & 1 & 0 & -1 & -1 & 0 & 1 & 1 \\ 0 & -2 & 1 & 0 & -1 & 2 & -1 & 0 & 1 \\ 0 & 0 & 1 & 1 & 1 & 0 & -1 & -1 & -1 \\ 0 & 0 & 1 & -2 & 1 & 0 & -1 & 2 & -1 \\ 0 & 1 & 0 & -1 & 0 & 1 & 0 & -1 & 0 \\ 0 & 0 & 1 & 0 & -1 & 0 & 1 & 0 & -1 \end{pmatrix} \begin{pmatrix} f_0 \\ f_1 \\ f_2 \\ f_3 \\ f_4 \\ f_5 \\ f_6 \\ f_7 \\ f_8 \end{pmatrix}^{(eq)} \quad (5.12)$$

Suppose that the equilibrium distribution function $f_\alpha^{(eq)}$ satisfy the following

$$f_\alpha^{(eq)} = w_\alpha \left[\rho + \frac{3}{c^2} \mathbf{e}_\alpha \cdot \mathbf{u} + \frac{9}{2c^4} (\mathbf{e}_\alpha \cdot \mathbf{u})^2 - \frac{3}{2c^2} \mathbf{u} \cdot \mathbf{u} \right] \quad (5.13)$$

which is an incompressible version for $f_\alpha^{(eq)}$ (He and Luo, 1997c) over the conventional version given by Eq. (1.4) for the SRT model.

Substitution of Eq. (5.12) into (5.13) yields the same relation between $(e, \varepsilon, q_x, q_y, p_{xx}, p_{xy})^{(eq)}$ and the velocity and density as given by Eq. (5.3). Hence, it is found that

$$\begin{aligned} \rho^{(eq)} &= \rho \\ j_x^{(eq)} &= u \\ j_y^{(eq)} &= v \end{aligned} \quad (5.14)$$

From Eq. (5.3) and Eq. (5.14), it can be seen that to maintain the continuity of u , v , and ρ across the interface, one needs,

$$(\rho, e, \varepsilon, j_x, q_x, j_y, q_y, p_{xx}, p_{xy})^{(eq,c)} = (\rho, e, \varepsilon, j_x, q_x, j_y, q_y, p_{xx}, p_{xy})^{(eq,f)} \quad (5.15)$$

Substituting Eq. (5.2) into Eq. (5.4), one obtains

$$\tilde{\underline{F}} = \underline{\underline{M}}^{-1} \underline{\underline{R}} - \underline{\underline{M}}^{-1} \underline{\underline{S}} (\underline{\underline{R}} - \underline{\underline{R}}^{(eq)}) \quad (5.16)$$

where \sim denotes the post-collision state of the \underline{F} vector

Using $\underline{R} = \underline{R}^{(eq)} + \underline{R}^{(neq)}$, it is seen that

$$\underline{\tilde{F}} = \underline{\underline{M}}^{-1} \underline{R}^{(eq)} + \underline{\underline{M}}^{-1} (\underline{I} - \underline{\underline{S}}) \underline{R}^{(neq)} \quad (5.17)$$

where

$$\underline{R}^{(neq)} = \begin{bmatrix} \rho - \rho^{(eq)} \\ e - e^{(eq)} \\ \varepsilon - \varepsilon^{(eq)} \\ j_x - j_x^{(eq)} \\ q_x - q_x^{(eq)} \\ j_y - j_y^{(eq)} \\ q_y - q_y^{(eq)} \\ p_{xx} - p_{xx}^{(eq)} \\ p_{xy} - p_{xy}^{(eq)} \end{bmatrix} = \begin{bmatrix} 0 \\ e - e^{(eq)} \\ \varepsilon - \varepsilon^{(eq)} \\ 0 \\ q_x - q_x^{(eq)} \\ 0 \\ q_y - q_y^{(eq)} \\ p_{xx} - p_{xx}^{(eq)} \\ p_{xy} - p_{xy}^{(eq)} \end{bmatrix} \quad (5.18)$$

In the vector $\underline{R}^{(neq)}$, density and momentum flux do not appear in the relaxation or collision procedure even if the corresponding relaxation parameter in \underline{S} is not zero. Thus these parameters can be any value and they will not affect the computational result.

Stresses are determined by

$$\tau_{xy} = (1 - \frac{s_8}{2})(p_{xy} - p_{xy}^{(eq)}) = (1 - \frac{s_8}{2})p_{xy}^{(neq)} \quad (5.19)$$

$$\tau_{xx} = (1 - \frac{s_9}{2})(p_{xx} - p_{xx}^{(eq)}) = (1 - \frac{s_9}{2})p_{xx}^{(neq)} \quad (5.20)$$

To maintain the shear stress continuity across the interface, in the 2-D case, it requires that

$$(1 - \frac{s_8^{(c)}}{2})p_{xy}^{(neq,c)} = (1 - \frac{s_8^{(f)}}{2})p_{xy}^{(neq,f)} \quad (5.21)$$

$$\text{or } p_{xy}^{(neq,c)} = m \frac{s_8^{(f)}}{s_8^{(c)}} p_{xy}^{(neq,f)} \quad (5.22)$$

Other components in the vector $(\rho, e, \varepsilon, j_x, q_x, j_y, q_y, p_{xx}, p_{xy})^{(neq)}$ remain unchanged across the interface except for p_{xx} and p_{xy} . Thus the non-equilibrium terms in the coarse grid can be expressed using the fine grid results as:

$$\underline{R}^{(neq,c)} = \begin{bmatrix} 0 \\ e - e^{(eq)} \\ \varepsilon - \varepsilon^{(eq)} \\ 0 \\ q_x - q_x^{(eq)} \\ 0 \\ q_y - q_y^{(eq)} \\ m \frac{s_8^{(f)}}{s_8^{(c)}} (p_{xx} - p_{xx}^{(eq)}) \\ m \frac{s_9^{(f)}}{s_9^{(c)}} (p_{xy} - p_{xy}^{(eq)}) \end{bmatrix}^{(f)} = \underline{T}^{(f)} \begin{bmatrix} 0 \\ e - e^{(eq)} \\ \varepsilon - \varepsilon^{(eq)} \\ 0 \\ q_x - q_x^{(eq)} \\ 0 \\ q_y - q_y^{(eq)} \\ (p_{xx} - p_{xx}^{(eq)}) \\ (p_{xy} - p_{xy}^{(eq)}) \end{bmatrix}^{(f)} \quad (5.23)$$

where

$$\underline{T}^{(f)} = \text{diag}(1, 1, 1, 1, 1, 1, m \frac{s_8^{(f)}}{s_8^{(c)}}, m \frac{s_9^{(f)}}{s_9^{(c)}}) \quad (5.24)$$

Now consideration is given to the post-collision state. In coarse grid block,

$$\underline{\tilde{F}}^{(c)} = \underline{M}^{-1} \underline{R}^{(eq,c)} + \underline{M}^{-1} (\underline{I} - \underline{S}^{(c)}) \underline{R}^{(neq,c)} \quad (5.25)$$

Using the condition that $\underline{R}^{(eq,c)} = \underline{R}^{(eq,f)}$ and Eq. (5.23), one obtains

$$\underline{\tilde{F}}^{(c)} = \underline{M}^{-1} \underline{R}^{(eq,f)} + \underline{M}^{-1} (\underline{I} - \underline{S}^{(c)}) \underline{T}^{(f)} \underline{R}^{(neq,f)} \quad (5.26)$$

The non-equilibrium part of the distribution function in fine grid is given by

$$\underline{R}^{(neq,f)} = (\underline{I} - \underline{S}^{(f)})^{-1} \left[\underline{M} \underline{\tilde{F}}^{(f)} - \underline{R}^{(eq,f)} \right] \quad (5.27)$$

Substituting Eq. (5.27) into Eq. (5.25) yields

$$\underline{\tilde{F}}^{(c)} = \underline{M}^{-1} \underline{R}^{(eq,f)} + \underline{M}^{-1} (\underline{I} - \underline{S}^{(c)}) \underline{T}^{(f)} (\underline{I} - \underline{S}^{(f)})^{-1} \left[\underline{M} \underline{\tilde{F}}^{(f)} - \underline{R}^{(eq,f)} \right] \quad (5.28)$$

In transferring the data from a coarse grid to a fine grid, one similarly obtains

$$\underline{\widetilde{F}}^{(f)} = \underline{\underline{M}}^{-1} \underline{\underline{R}}^{(eq,c)} + \underline{\underline{M}}^{-1} (I - \underline{\underline{S}}^{(f)}) \underline{\underline{T}}^{(c)} (I - \underline{\underline{S}}^{(c)})^{-1} [\underline{\underline{M}} \underline{\widetilde{F}}^{(c)} - \underline{\underline{R}}^{(eq,c)}] \quad (5.29)$$

where

$$\underline{\underline{T}}^{(c)} = diag(1,1,1,1,1,1, \frac{s_8^{(c)}}{ms_8^{(f)}}, \frac{s_9^{(c)}}{ms_9^{(f)}}) \quad (5.30)$$

5.4.2 Computational Assessment

5.4.2.1 Steady flow over the NACA0012 airfoil

Flows over the NACA 0012 airfoil (Figure 3.20) at $Re=5000$ are computed with the present multi-block LBE scheme. The computational domain and block configuration are the same as the ones in Chapter 3. In the first case, $s_8=s_9=1/0.502$, $s_2=1.81$, and $s_3=s_5=s_7=1.2$ are given in coarsest blocks. s_2 , s_8 , and s_9 are rescaled in different blocks. s_3 , s_5 , and s_7 are kept unchanged. Figure 5.12 shows the result of drag coefficient. It can see that the computation is not converged. Lallemand and Luo (2000) suggest that s_3 , s_5 , and s_7 should be chosen slightly larger than 1 to reduced the over-relaxation effects of these modes. To test if that requirement is necessary in multi-block method, a second case is computed. In the second case, $s_8=s_9=1/0.502$, $s_2=1.81$, and $s_3=s_5=s_7=1.2$ are given in the coarsest grid. All the relaxation times are rescaled. We have $s_3=s_5=s_7=0.85$ in the intermediate grid and $s_3=s_5=s_7=0.32$ in the finest grid. Figure 5.16 shows the non-convergent drag coefficient. In the final case $s_8=s_9=1/0.502$, and $s_2=s_3=s_5=s_7=1.8$ are given in the coarsest grid. All the relaxation times are rescaled. s_2 , s_3 , s_5 , and s_7 are equal to 1.09 in the finest block. Figure 5.14 shows the convergent history of drag coefficient. In this case, computation converges to steady state. The final value of drag is 0.05379 comparing with the value of 0.05409 by Drela

and Giles (1987). It can be concluded from above cases that all relaxation times are need to be rescaled and s_3, s_5 , and s_7 are need to be larger than 1 when different values are assigned to different relaxation times.

5.4.2.2 Lid-driven cavity flow

The lid-drive cavity flow is used to assess the present multi-block strategy with the MRT model, especially for the interface conditions. The computational domain and parameter are identical to the ones used in Chapter 3. The relaxation parameter are $s_2 = s_3 = s_5 = s_7 = 1.8$. The position of the center of the primary vortices is (0.6172, 0.7350) for $Re=100$, compared well with the value (0.6172, 0.7344) from Ghia *et al.* (1982). The u - and v -components of the velocity along the vertical line and horizontal line through the geometry center are shown in Figure 5.15a and Figure 5.15b, respectively. It is seen that the velocity profile by both MRT and SRT models agree well with results from Ghia *et al.* (1982). Figure 5.16 shows the pressure contours obtained from the multi-block solution. Figure 5.17 shows a local, enlarged view of the pressure contour around an interface corner point indicated by the circle in Figure 5.16. Clearly, the pressure is smooth across the interface. Figure 5.18-Figure 5.20 show the contours of shear stress and velocity components, which are also smooth across the interface.

To demonstrate more clearly the conservation and continuity characteristics at the interface, the velocity, density, and shear stress along the interface AB in Figure 5.16 are shown. Again, the values of physical variables from the fine block on interface AB are obtained by second order extrapolation from inside the fine grid domain. Figure 5.21 and Figure 5.22 show the velocity on the interface. It can be seen that the velocity profiles between coarse and fine grids agree very well. Figure 5.23 shows pressure on the

interface which are smoother in both coarse and fine blocks than those using the SRT model, shown in Figure 3.17. However there is a larger discrepancy of pressure on interface between fine and coarse grid near the upper wall. It is believed that the source of this discrepancy is from the treatment of the upper wall boundary. As mentioned in Chapter 3, the different Δ at the intersection of two blocks at upper wall may cause inaccuracy in the boundary treatment. It is also interesting to note that the oscillation of pressure in coarse grid did not transfer into fine grid.

5.5 Conclusions

Based on the detailed examination of the flow fields in selected cases, it is clear that the MRT model has substantial advantages over the SRT model in handling the geometric singularities. The MRT model in general provides smoother variations of the macroscopic quantities and has much smaller regions of the oscillation near a singularity. Since the spatial oscillation is often accompanied by the high frequency pressure waves in transient simulations, the MRT model also offers a better convergence toward steady state as well. The MRT model is strongly recommended.

A multi-block scheme is developed for the MRT model in the LBE method. The interface condition for the MRT model is derived to ensure the mass conservation and stress continuity between neighboring blocks. This new treatment retains the inherent advantages of both MRT model and the multi-block methods.

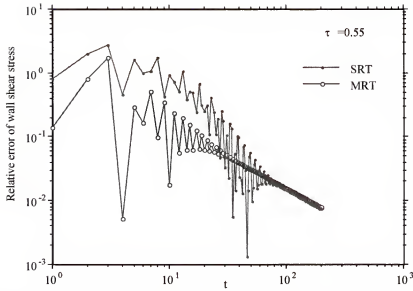


Figure 5.1 Comparison of the relative error in the evolution of the wall shearstress for Stokes first problem between the SRT and MRT models.

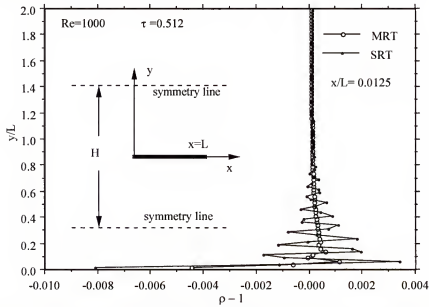


Figure 5.2 Comparison of the density profiles near the leading edge ($x/L=0.0125$) between the SRT model and MRT model at $Re=1000$.

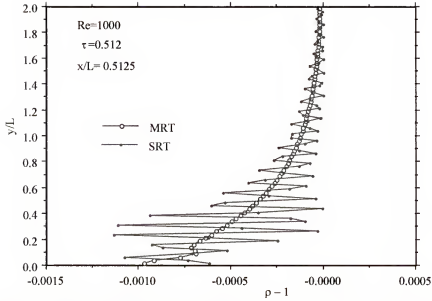


Figure 5.3 Comparison of the density profiles at $x/L=0.5125$ between the SRT model and MRT model at $Re=1000$.

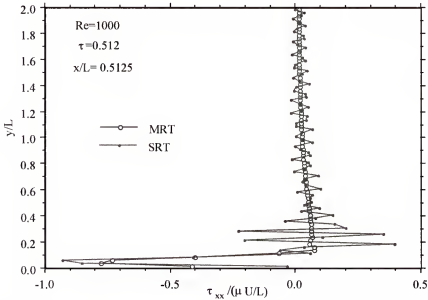


Figure 5.4 Comparison of the viscous normal stress profiles at $x/L=0.5125$ between the SRT model and MRT model at $Re=1000$.

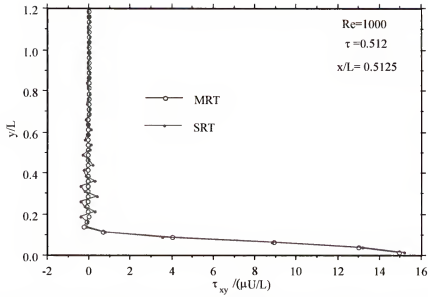


Figure 5.5 Comparison of the viscous shear stress profiles at $x/L=0.5125$ between the SRT model and MRT model at $Re=1000$.

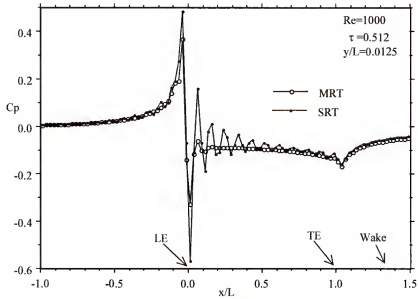


Figure 5.6 Comparison of pressure coefficient as a function of x at $y/L=0.0125$ between the SRT model and MRT model.

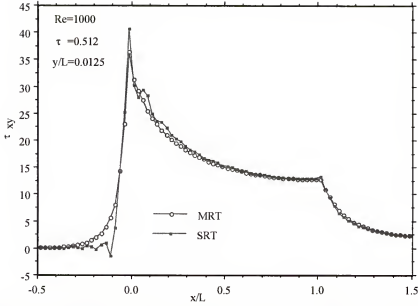


Figure 5.7 Comparison of viscous shear stress as a function of x at $y/L=0.0125$ between the SRT model and MRT model.

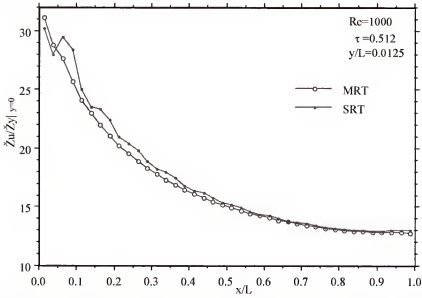


Figure 5.8 Comparison of wall vorticity as a function of x between the SRT model and MRT model.

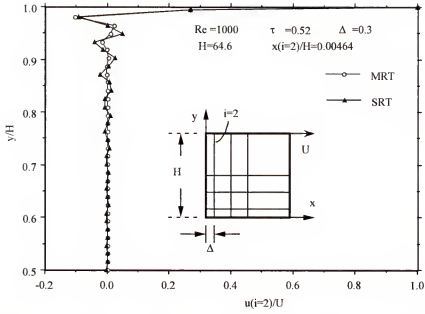


Figure 5.9 Comparison of the velocity profiles of x-component at $x=\Delta$ ($i=2$).

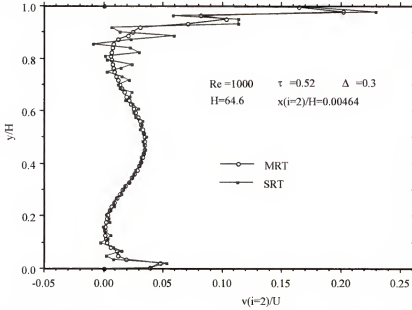


Figure 5.10 Comparison of the velocity profiles of y-component at $x=\Delta$ ($i=2$).

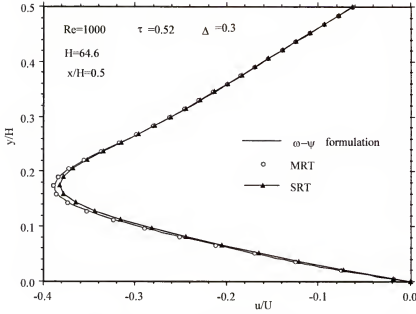


Figure 5.11 Comparison of the velocity profiles of x-component at $x/H=0.5$ in the lower region of the cavity.

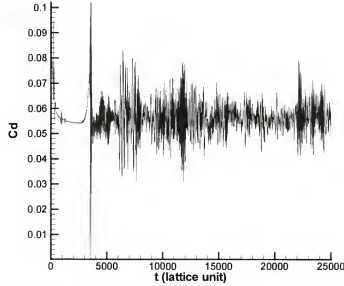


Figure 5.12 Convergent history of drag coefficient, here $s_8=s_9=1/0.502$, $s_2=1.81$, $s_3=s_5=s_7=1.2$ in coarsest block. s_3 , s_5 , and s_7 are not rescaled.

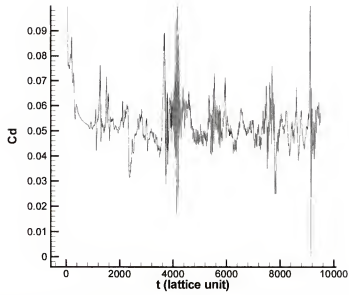


Figure 5.13 Convergent history of drag coefficient, here $s_8=s_9=1/0.502$, $s_2=1.81$, $s_3=s_5=s_7=1.2$ in coarsest block. All parameters are not rescaled.

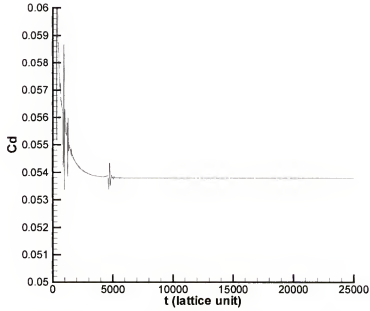


Figure 5.14 Convergent history of drag coefficient, here $s_8=s_9=1/0.502$, $s_2=s_3=s_5=s_7=1.81$ in coarsest block. All parameters are not rescaled.

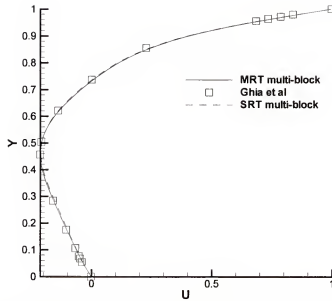


Figure 5.15a Comparison of u -velocity along the vertical line through geometric center.

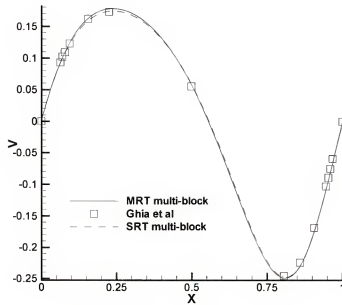


Figure 5.15b Comparison of v -velocity along the horizontal line through geometric center.

Figure 5.15 Comparison of velocity between SRT model, MRT model and those by Ghia *et al.* (1982).

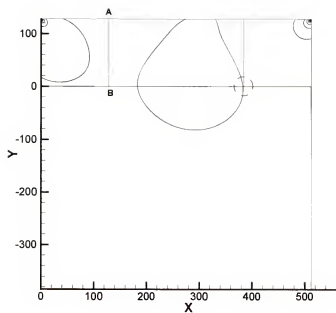


Figure 5.16 Pressure contours in the cavity from the multi-block MRT LBE solution. (For the circled region, see Figure 5.17)

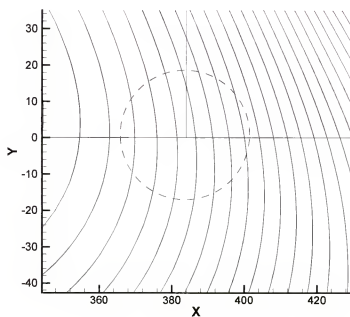


Figure 5.17 Enlarged view of pressure contour in the circled region in Figure 5.16 near the intersection of three blocks. The figure demonstrates that the block interface and corner are well handled in MRT model.

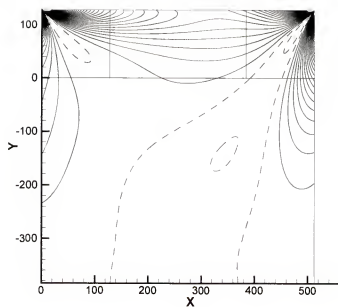


Figure 5.18 Shear stress contour based on the MRT model. Solid and dash lines represent positive and negative values, respectively.

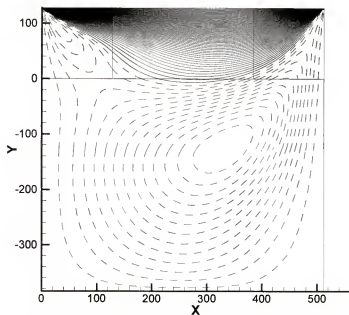


Figure 5.19 Contour of x-component of velocity based on the MRT model. Solid and dash lines represent positive and negative values, respectively

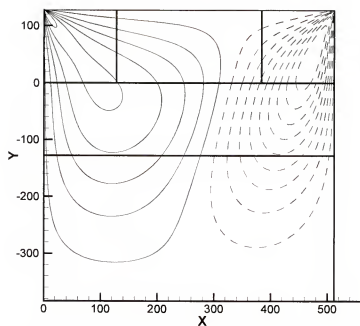


Figure 5.20 Contour of y-component of velocity based on the MRT model. Solid and dash lines represent positive and negative values, respectively

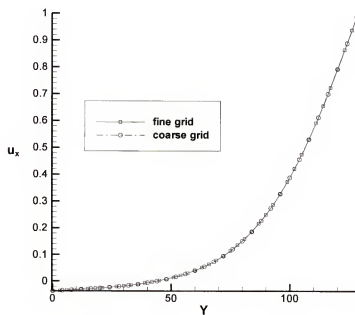


Figure 5.21 The x-component of the velocity u_x/U on the interface AB based on the MRT model. In Figure 5.21-Figure 5.22, $U=0.0156$.

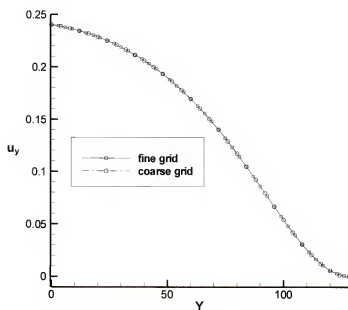


Figure 5.22 The x-component of the velocity u_y/U on the interface AB based on the MRT model.

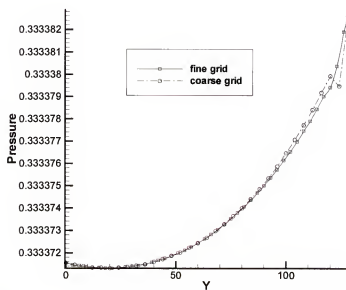


Figure 5.23 Pressure on the interface AB based on the MRT model.

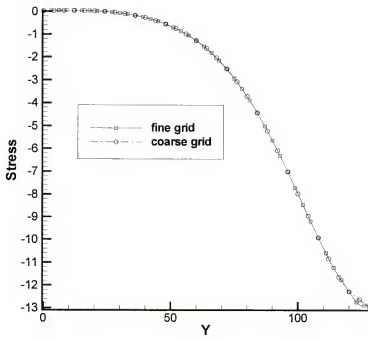


Figure 5.24 Shear stress $\tau_{xy} / (\mu U / H)$ on the interface AB based on the MRT model.

CHAPTER 6

IMPROVEMENT OF BOUNDARY TREATMENTS IN THE LBE METHOD

Two classes of boundaries in LBE simulation are considered here: the open boundary and solid wall boundary. Most of the previous research efforts have focused on the treatment of the solid wall boundary. Here we first give a brief description on the development of solid wall boundary conditions.

The bounce-back condition originated from lattice gas automata has been extensively used in LBE simulation (Ziegler 1993, Ginzbourg and Alder 1994). The bounce-back scheme in the LBE method is intuitively derived from LGA. In this scheme, the particle (the basic variable in LGA) hits the wall and bounces back opposite to its incoming direction. In LBE, the particle number is replaced with a real variable f_α . This scheme is very simple, efficient and easy to implement. On the other hand, the bounce-back scheme is only a first order treatment in general (Ginzbourg and Alder 1994). In simulating suspension flow, Ladd (1994) placed the wall halfway between the nodes and it has been shown that this treatment has the second order accuracy for the straight wall.

The bounce-back scheme has been modified to reduce the wall slip velocity by Nobel *et al.* (1995), Inamuro *et al.* (1995), and Maier *et al.* (1996). Zou and He (1997) extend the bounce-back condition to non-equilibrium part of distribution function.

To improve the numerical accuracy, Skordos (1992) suggest adding a first order non-equilibrium distribution in the equilibrium distribution at the wall nodes. Chen *et al.*

(1996) placed the wall at the node and used extrapolation of f_α on the fluid side to obtain the f_α at \mathbf{x}_b .

All the boundary treatments mentioned above modeled curved wall as zig-zag steps, which results in geometric discontinuities and affect the computational accuracy. This error is amplified when Re increases.

Filippova and Hänel (1998) presented a curved boundary condition using Taylor series expansion in both space and time for f_α near the wall. This boundary condition provides a second order accurate treatment for a curved solid wall boundary. In addition, two other boundary treatments, one by Mei *et al.* (1999) and the other by Bouzidi *et al.* (2001) have also been presented. The details of above three boundary conditions will be provided in Section 6.2 along with a new solid wall boundary treatment.

In general, open boundaries refer to lines (or planes) of symmetry, periodic boundary, infinity, and inlet and outlet. For symmetric and periodic boundaries, the condition can be given exactly. There is not much attention given to the impact of the inlet condition on the quality of the solution in LBE. Usually the solid wall boundary condition is used to provide the distribution functions at inlet. This treatment can cause instability in the computation, because the fluctuation inside the computational domain will be reflected back from the inlet. In Section 6.1, a new inlet treatment is presented to address this issue.

When a boundary moves, new issues arise. For example a fluid node can experience the change of phase. These issues will be discussed in Section 6.3 with presenting a moving wall boundary condition.

6.1 The Open Boundary Treatment

6.1.1 Introduction

Different methods have been implemented to obtain the distribution function f_α at the inlet, from which the specified velocity or pressure can be recovered. The most commonly used approach is based on the bounce-back of the distribution function or non-equilibrium part of distribution function (Cornubert *et al.* 1991, Ziegler 1993, Behrend 1995). Typically one places the inlet boundary half way between the inlet boundary grid and the grid after the inlet with a known velocity profile specified at the inlet. The standard bounce-back scheme for f_α at the inlet gives:

$$\tilde{f}_{\bar{\alpha}}_{inlet} = \tilde{f}_\alpha + 2w_\alpha \rho_{internal} \frac{3}{c^2} \mathbf{e}_{\bar{\alpha}} \cdot \mathbf{u}_{inlet} \quad (6.1)$$

where w_α is the weighting factor, and $\mathbf{e}_{\bar{\alpha}} = -\mathbf{e}_\alpha$.

Grunau (1993) placed the inlet at the lattice node as opposed to the lattice link half-way between the grids. He then assigned equilibrium distribution function to be the desired f at the inlet. For the 2-D, 9-velocity model, this method gives:

$$f_{\bar{\alpha}}_{inlet} = f_\alpha^{(eq)} = w_\alpha \rho_{inlet} \left[1 + \frac{3}{c^2} \mathbf{e}_\alpha \cdot \mathbf{u}_{inlet} + \frac{9}{2c^4} (\mathbf{e}_\alpha \cdot \mathbf{u}_{inlet})^2 - \frac{3}{2c^2} \mathbf{u}_{inlet}^2 \right] \quad (6.2)$$

This method was considered to have a larger error than the one using Eq. (6.1) (Zou and He 1997).

Skordos (1992) presented a scheme to calculate f_α from a given initial velocity and density field (1992). In this scheme the boundary is placed at the lattice nodes and the first order term in the Chapman-Enskog expansion $f^{(1)}$, is added to $f^{(eq)}$, to obtain the desired distribution function,

$$f_{\bar{\alpha}_{inlet}} = f_{\bar{\alpha}_{inlet}}^{(eq)} + f_{\bar{\alpha}_{inlet}}^{(l)} \quad (6.3)$$

In computing $f^{(l)}$, the gradients of velocity and density are required. For computational purpose, the gradient was obtained by using finite difference inside the computational domain near the inlet. If the inlet velocity derivative is known, there is no need to use finite difference to obtain $f^{(l)}$. This method can result in very stable computation if the analytical value, instead of the finite difference, for the gradient is used. When finite difference is used in constructing $f^{(l)}$, since the value inside the computational domain is used computational stability may be compromised.

In Eq. (6.1), f_{α} at the inlet is determined using the variables of f 's inside the computational domain. Hence,

$$f_{\alpha_{inlet}} = Function(f_{\alpha_{internal}}, \rho_{internal}, \mathbf{u}_{inlet}) \quad (6.4)$$

In Eq. (6.3) the equilibrium part of distribution function is determined by the values of known density and velocity at the inlet,

$$f_{\bar{\alpha}_{inlet}}^{(eq)} = Function(\rho_{inlet}, \mathbf{u}_{inlet}) \quad (6.5)$$

If the gradients for the density and velocity are evaluated using finite difference, the non-equilibrium part is related to the values the velocity and density inside the computational domain so that:

$$f_{\bar{\alpha}_{inlet}}^{(l)} = Function(\rho_{internal}, \mathbf{u}_{internal}) \quad (6.6)$$

If the gradients are given analytically, $f_{\bar{\alpha}_{inlet}}^{(l)}$ does not vary with the flow variables inside the domain. However, this can result in over-specification of the boundary conditions (for macroscopic variables) as one needs both the value and derivative of the

variable on one side of the domain. When the inlet velocity is uniform, Eq. (6.3) can be further simplified to

$$f_{\bar{\alpha}_{inlet}} = f_{\bar{\alpha}_{inlet}}^{(eq)} \quad (6.7)$$

We refer to Eq. (6.7) as the equilibrium inlet condition.

We now can see that equations (6.1) and (6.3) are different in one major aspect. In Eq. (6.1), $f_{\bar{\alpha}_{inlet}}$ is the function of ρ and f_{α} 's of the interior nodes whereas in Eq. (6.4), $f_{\bar{\alpha}_{inlet}}$ is only function of gradient of the ρ and f_{α} 's.

In Skordos's approach, the specification of the gradients of density and velocity analytically eliminates the interaction/coupling between the boundary nodes and the interior nodes, but the coupling can get stronger when the finite difference is used to evaluate the derivatives since the values at the interior points are used. Such a strong coupling often results in strong pressure wave to originate from the inlet.

In most calculations using Eq. (6.1) to specify the inlet condition, the pressure field exhibits fluctuation during calculation. This can be understood now since the bounce-back condition given by Eq. (6.1) allows for strong coupling/interaction between the interior and the inlet boundary. This kind of interaction/coupling will become a serious problem when computing high Reynolds number flow. Figure 6.1 shows the pressure contour for a flow over NACA0012 airfoil at $Re=2000$. The boundary conditions at inlet, upper and lower boundaries are given using bounce-back condition. It can easy see that there is a strong interaction between inlet and interior field. This interaction is intensified at the two corners near the inlet, because at this region the interaction comes from both the inlet and the upper or lower boundary.

6.1.2 The Proposed Inlet Treatment

Equation (6.3) gives an inlet condition, which does not reflect the pressure oscillation back into computational domain, but the finite difference used to obtain $f^{(1)}$ can cause computational instability (Skordos, 1992). Here we propose an inlet boundary condition that retains the basic characteristic of Eq. (6.3); that is the equilibrium part of the distribution function at inlet is obtained using the known inlet velocity and density, while $f^{(1)}$ is replaced with non-equilibrium part of distribution function $f^{(noneq)}$:

$$f_{\bar{\alpha}_{inlet}} = f_{\bar{\alpha}_{inlet}}^{(eq)} + f_{\bar{\alpha}_{inlet}}^{(noneq)} \quad (6.8)$$

Here a 1-D example is used to clarify the how to find the values of $f_{\bar{\alpha}_{inlet}}^{(eq)}$ and $f_{\bar{\alpha}_{inlet}}^{(noneq)}$ in Eq. (6.8), which correspond the $f_{1,B}^{eq}$ and $f_{1,B}^{noneq}$ in Figure 6.3 . Considering post streaming stage at the inlet, boundary conditions need to be given to specified $f_{1,B}$, which include two components: $f_{1,B}^{eq}$ and $f_{1,B}^{noneq}$. At the inlet fluid density and velocity are known, thus the equilibrium distribution function $f_{1,I}^{(eq)}$ at inlet can be determined. Knowing the $f_{1,I}^{eq}$ and $f_{1,C}^{eq}$, $f_{1,B}^{eq}$ can be obtained easily using liner interpolation:

$$f_{1,B}^{(eq)} = f_{1,I}^{(eq)} + (f_{1,C}^{(eq)} - f_{1,I}^{(eq)}) \frac{\Delta}{1 + \Delta} \quad (6.9)$$

The inlet can be placed arbitrary. It takes a little bit more effort to find $f_{1,B}^{noneq}$. To avoid using an extrapolation to find $f_{5,I}^{noneq}$, such as

$$f_{5,I}^{noneq} = f_{5,B}^{noneq} + (f_{5,B}^{noneq} - f_{5,C}^{noneq}) \cdot \Delta \quad (6.10)$$

which maybe lead the instability in computation, we let

$$f_{5,I}^{noneq} = f_{5,B}^{noneq} \quad (6.11)$$

Then momentum balance requires

$$f_{1,J}^{noneq} = f_{1,S}^{noneq} \quad (6.12)$$

Finally an interpolation is used to obtain $f_{1,B}^{noneq}$:

$$f_{1,B}^{noneq} = f_{1,J}^{noneq} + (f_{1,C}^{noneq} - f_{1,J}^{noneq}) \cdot \frac{\Delta}{1 + \Delta} \quad (6.13)$$

Using this method, the non-equilibrium part of the distribution function can be added to the equilibrium distribution function. We call this inlet boundary condition as local inlet condition

6.1.3 Computational Assessment

In the computational cases to be presented and discussed, the following questions are addressed:

1. Will the local inlet condition give the same accurate results as those of bounce-back if both conditions lead to converged results?
2. How does the inlet/free-stream boundary condition impact: the convergence of the solution and the quality of the flow field? Flows over a column of circular cylinders under different initial condition and different Reynolds numbers and a flow over an airfoil are used to assess these issues.

6.1.3.1 Steady uniform flow over a column of cylinders under $Re=40$

For a uniform flow over a column of circular cylinders of radius r with center-to-center distance denoted by H , symmetry conditions for f_a 's are imposed at $y = \pm H/2$. At the inlet, the uniform velocity, $u=V$, is specified using bounce-back boundary condition and the local inlet condition.

At the exit, a simple extrapolation is used,

$$f_d(N_x, j) = 2f_d(N_x-1, j) - f_d(N_x-2, j) \quad \text{for } \alpha=4, 5, \text{ and } 6. \quad (6.14)$$

On the surface of the circular cylinder, FH's boundary condition is used to update the f_α 's; see Figure 6.2 for the computational domain. In the computation $\tau=0.52$, $u_{inlet}=0.0127$. The drag coefficient is calculated using the momentum exchange method.

Figure 6.4a shows the convergence histories of the drag coefficient using these two inlet conditions. It is seen that the local inlet condition results in much smaller oscillation and faster convergence towards the steady state than that using bounce-back inlet condition. Furthermore, C_d based on the local inlet condition possesses much smaller oscillation than that using bounce-back inlet condition when the solution is near convergence. This means that the pressure oscillation in the flow field is much small when local condition is used. The average values of two converged results are nearly the same with $C_d \approx 1.6485$ (Figure 6.4b).

6.1.3.2 Steady uniform flow over a column of cylinders under $Re=100$ with initial velocity equal inlet velocity

In this case all other parameters are kept the same as those in the first case, except that Reynolds number is increased to 100 by increasing the inlet velocity. Figure 6.5 shows the convergence results after vortex beginning to shed. The bounce-back condition gives:

$$C_{d_average}=1.411$$

$$C_{L_max}=0.335$$

The local inlet condition gives:

$$C_{d_average}=1.407$$

$$C_{L_max}=0.334$$

We obtain $St=0.33$ for both cases. This case shows that both bounce-back and local inlet condition can produce same results if convergence is achieved.

6.1.3.3 Steady uniform flow over a column of cylinders under $Re=100$ with initial velocity =0

All computational parameters are the same as those in case 2, except that the initial velocity is set to 0, which means that there will be a strong interaction between inlet and the interior of the flow field. Figure 6.6 shows drag and lift coefficients using inlet condition based on the bounce-back condition. Irregular pattern appears in C_l curve after vortex shedding starts. It does not die out with time. It suggests that strong interaction exists between inlet boundary and interior field. Figure 6.7 shows results using local inlet condition. The lift coefficient C_l behaves quite well. It suggests a much weaker interaction between inlet boundary and interior field.

6.1.3.4 A steady flow over NACA0012 airfoil

The NACA 0012 airfoil is a popular wing model, which has been used extensively. Flow fields at $Re=500$, 1000, 2000, and 5000 have been computed using the multi-block LBE scheme. Details have been given in Chapter 3. At the inlet, upper and lower boundaries, local inlet condition are used for f_i 's based on the free-stream velocity. At the downstream boundary a zeroth order extrapolation for f_i 's is used.

The bounce-back inlet condition yields unphysical, large scale spatial-temporal oscillation in the flow field when $Re=2000$ and $Re=5000$ ($\tau=0.5025$ and 0.50125 respectively). Figure 6.8 shows the variation of drag with time under $Re=2000$ using bounce-back condition. It can easily see that flow soon become unsteady after the computation starts. Figure 6.9 shows the variation of drag with time under $Re=2000$ using local inlet condition. Using local inlet condition computation convergences very

faster to the steady state. $C_d=0.8601$ is very close to the value of 0.8373 by Xfoil. Figure 6.10 shows the density contour of flow field using bounce-back at time equaling to 30000 lattice unit. The irregular and large scale density oscillation shows that flow field has become unphysical. Figure 6.11 shows density contour using local inlet condition at time equaling to 30000 lattice unit. It can see that there is no oscillation of density in the flow field. Thus the local inlet condition is demonstrated to be superior over the bounce-back type of inlet condition. It greatly improved the computational stability and the quality of the solution.

6.1.3.5 Channel flow over an asymmetrically placed cylinder at $Re=20$

Schäfer and Turek (1996) reported a study of a laminar flow over a circular cylinder placed asymmetrically inside a channel. In the present study, the computational domain and parameters are the same as the ones in Section 4.3.3, except that Re equals to 20 present case. At inlet bounce-back and local inlet conditions are used. Both inlet conditions give $C_d=5.59$ which is in the range of 5.57-5.59 by Schäfer and Turek (1996). Figure 6.12 shows the comparison of velocity profiles along the y-direction for both inlet conditions at nodes, which are 0.2 lattices to the right of inlet. Figure 6.13 shows shear stress profiles along the same direction at same position as Figure 6.12. It can see that local inlet condition can successfully specifies the stress at the inlet. In Figure 6.13, shear stress profiles are not linear distributions along y-direction because of the affect of cylinder.

6.1.4 Conclusions

Computations based on the bounce-back inlet condition and equilibrium inlet conditions are performed for various cases. Bounce-back inlet condition results in slower

convergence toward steady or dynamically steady state and causes stronger interaction between the inlet and interior field. Such interaction may affect the long-term behavior of the solution, especially at higher Re . Using the local equilibrium value at the inlet can reduce the impact of the boundary-interior interaction on the unsteady development of the flow field, improves the convergence rate, improves the computational stability, and improves quality of the overall solution.

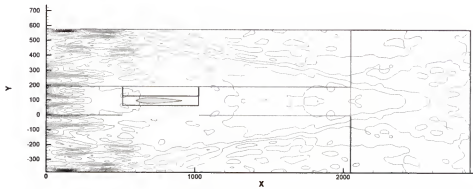


Figure 6.1 Density contour at $Re=2000$ using bounce-back condition at inlet, upper and lower boundaries

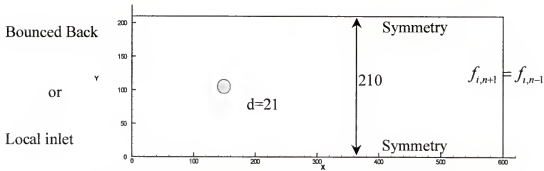


Figure 6.2 Computational domain and boundary conditions.

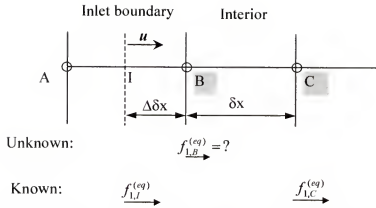


Figure 6.3b Configuration of equilibrium distribution at inlet.

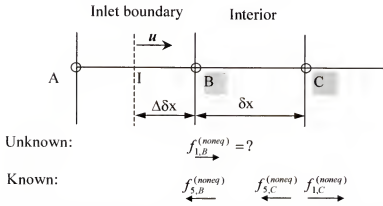


Figure 6.3a Configuration of non-equilibrium distribution at inlet.

Figure 6.3 Configuration of distribution functions which are used to construct inlet boundary condition.

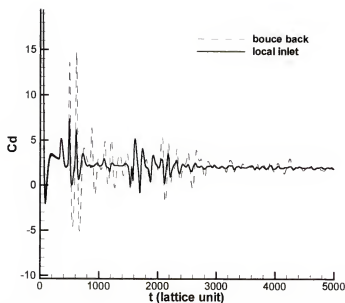


Figure 6.4a Convergence history of the drag coefficient.

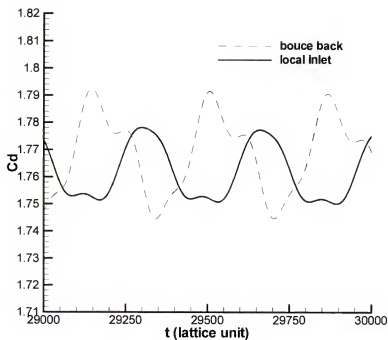


Figure 6.4b Drag coefficient near convergent state.

Figure 6.4 Convergence history of drag coefficient and value of drag near convergent state.

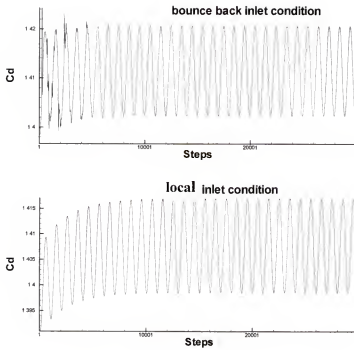


Figure 6.5 Drag coefficient after vortex shedding for both inlet conditions.

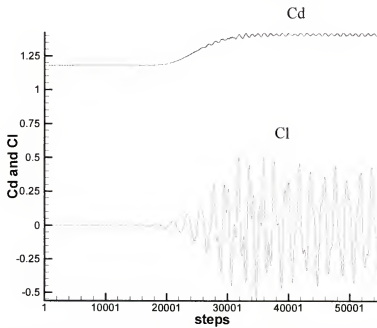


Figure 6.6 Convergence history of drag and lift coefficient using bounce-back inlet condition.

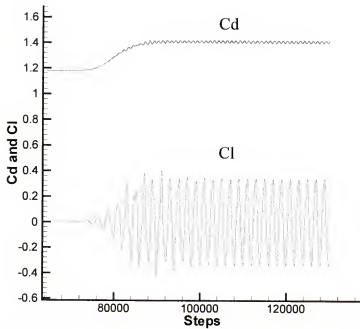


Figure 6.7 Convergence history of drag and lift coefficient using local inlet condition.

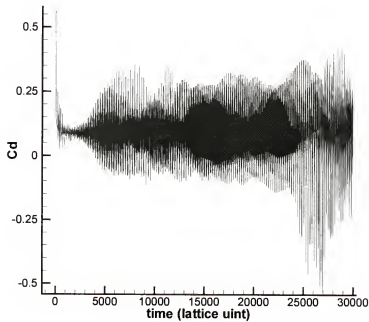


Figure 6.8 Convergence history of Drag coefficient at $Re=2000$ using bounce-back condition at inlet, upper and lower boundaries.

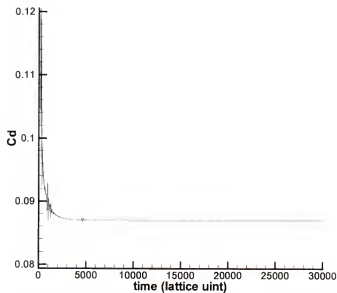


Figure 6.9 Convergence history of Drag coefficient at $Re=2000$ using local inlet condition at inlet, upper and lower boundaries

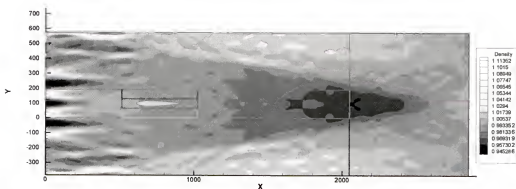


Figure 6.10 Density contour at time equaling to 30000 lattice unit at $Re=2000$ using bounce-back condition at inlet, upper and lower boundaries.

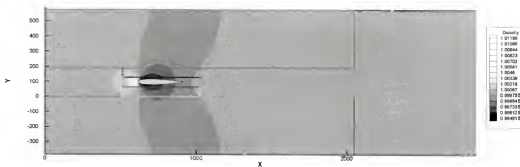


Figure 6.11 Density contour at time equaling to 30000 lattice unit at $Re=2000$ using local inlet condition at inlet, upper and lower boundaries

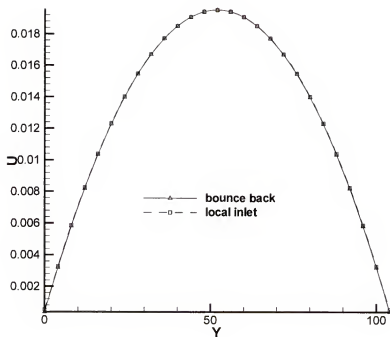


Figure 6.12 Velocity profile along y- direction at nodes which are 0.2 lattice unit to the right of inlet.

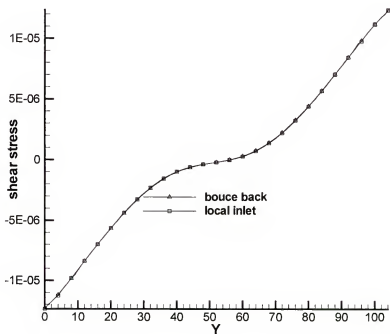


Figure 6.13 Shear stress profile along y-direction at nodes which are 0.2 lattice unit to the right of inlet.

6.2 A Unified Treatment for Solid Wall Boundary Condition in LBE

Recent development in solid wall boundary conditions can be found in Filippova and Hänel (1998), Mei *et al.* (1999), and Bouzidi *et al.* (2001). In order to establish the necessary background, these three treatments will be reviewed in the following.

The lattice nodes on the solid and fluid side are denoted as x_b and x_f , respectively, in Figure 6.14. The filled small circles on the boundary, x_w , denote the intersections of the wall with various lattice links. The boundary velocity at x_w is u_w . The fraction of an intersected link in the fluid region is Δ , that is:

$$\Delta = \frac{|x_f - x_w|}{|x_f - x_b|} \quad (6.15)$$

Obviously, $0 \leq \Delta \leq 1$ and the horizontal or vertical distance between x_b and x_w is $\Delta \tilde{\Delta}x$ on the square lattice. Suppose the particle momentum moving from x_f to x_b is e_α and the reversed one from x_b to x_f is $e_{\bar{\alpha}} = -e_\alpha$. Denoting the post-collision properties using \sim , it is seen that after the collision step, \tilde{f}_α on the fluid side is known, but not on the solid side. Using $e_{\bar{\alpha}}$ and $f_{\bar{\alpha}}$ to denote the velocity and the distribution function coming from a solid node to a fluid node, it is noted that $f_{\bar{\alpha}}$ is the unknown to be determined. That is, to finish the subsequent streaming step, $\tilde{f}_{\bar{\alpha}}(x_b, t)$ is needed. To construct $\tilde{f}_{\bar{\alpha}}(x_b, t)$ based upon some known information in the surrounding, Filippova and Hänel (1998) proposed to use the following linear interpolation:

$$\tilde{f}_{\bar{\alpha}}(x_b, t) = (1 - \chi) \tilde{f}_\alpha(x_f, t) + \chi f_\alpha^{(*)}(x_b, t) + 2W_\alpha \rho \frac{3}{c^2} e_{\bar{\alpha}} \cdot u_w \quad (6.16)$$

with

$$f_\alpha^{(*)}(x_b, t) = w_\alpha(x_f, t) \left[1 + \frac{3}{c^2} e_\alpha \cdot u_{bf} + \frac{9}{2c^4} (e_\alpha \cdot u_f)^2 - \frac{3}{2c^2} u_f \cdot u_f \right] \quad (6.17)$$

In the above, $\mathbf{u}_f \equiv \mathbf{u}(\mathbf{x}_f, t)$ is the fluid velocity near the wall and \mathbf{u}_{bf} is to be chosen.

$$\mathbf{u}_{bf} = (\Delta - 1)\mathbf{u}_f/\Delta + \mathbf{u}_w/\Delta \quad \text{and} \quad \chi = (2\Delta - 1)/\tau \quad \text{for} \quad \Delta \geq 1/2 \quad (6.18a)$$

$$\mathbf{u}_{bf} = \mathbf{u}_f \quad \text{and} \quad \chi = (2\Delta - 1)/(\tau - 1) \quad \text{for} \quad \Delta < 1/2. \quad (6.18b)$$

Mei *et al.* (1999) suggested using different nodes to obtain f_α when $\Delta < 0.5$ to improve the numerical stability over the scheme of Filippova and Hänel for the channel flow when τ is near 0.5. Bouzidi *et al.* (2001) presented a simpler boundary condition based on bounce-back at arbitrary position. In their work, a linear scheme and a quadratic scheme are given to obtain f_α at node inside the solid wall. The linear version is given as following:

$$f_{\bar{\alpha}}(\mathbf{r}_f, t + 1) = 2\Delta f_\alpha(\mathbf{r}_f + \mathbf{e}_\alpha) + (1 - 2\Delta)f_\alpha(\mathbf{r}_f) \quad \Delta < \frac{1}{2} \quad (6.19a)$$

$$f_{\bar{\alpha}}(\mathbf{r}_f, t + 1) = \frac{1}{2\Delta}f_\alpha(\mathbf{r}_f + \mathbf{e}_\alpha) + \frac{2\Delta - 1}{2\Delta}f_{\bar{\alpha}}(\mathbf{r}_f + \mathbf{e}_{\bar{\alpha}}) \quad \Delta < \frac{1}{2} \quad (6.19b)$$

They also reported numerical results for a circular Couette flow and flow over a periodical array of cylinders.

The above three boundary condition treatments all have second-order accuracy for curved boundary. The difference is that the first two need to construct a fictitious fluid point inside the solid wall, and perform a collision step at that node, while the scheme of Bouzidi *et al* only requires the known values of f_α on the fluid side. It is emphasized that three methods need to treat the boundary condition separately for $\Delta \leq 0.5$ and $\Delta > 0.5$.

In this effort, a unified scheme for curved boundary condition is presented, and tested along with those by Filippova and Hänel (1998), and Bouzidi *et al.* (2000) for several fluid flow problems: 2-D channel flow with constant pressure gradient, the Stokes first

problem, and uniform flow over a column of circular cylinder. Finally the results of flow over an oscillation plate are given.

6.2.1 The Unified Boundary Condition for Solid Wall Boundary

When simulating the evolution of f_α with the collision and streaming steps, one needs to address several issues. For example, to finish the streaming step, f_α at solid boundary node \mathbf{x}_b must be specified. Usually we consider obtaining the required boundary condition based on the value of f_α after the collision step. We can also perform a streaming step with a null boundary value f_α , and then add the null boundary value with appropriate f_α after the streaming. There is a difference between these two approaches, because the streaming redistributes f_α in space. Referring to Figure 6.14, after streaming, f_{f4} at the fluid node \mathbf{f} is needed while the values of f_{b8} and f_{j8} are known. Using a linear interpolation, f_{w8} can be easily found as:

$$f_{w8} = f_{j8} + (f_{b8} - f_{j8}) * \Delta \quad (6.20)$$

Here f_{w8} is the distribution function at the point on the wall where the link along \mathbf{e}_8 direction intersects with the solid wall. To ensure the no-slip boundary condition ($\mathbf{u}_w = 0$ here) on the wall, *considering the momentum balance in each direction*, we set

$$f_{w4} = f_{w8} \quad (6.21)$$

Using the f_{w4} and f_{ff4} (which is f_{ff4} at the fluid node \mathbf{ff}), f_{f4} can be obtained using a linear interpolation:

$$f_{f4} = f_{w4} + (f_{ff4} - f_{w4}) / (1 + \Delta) * \Delta \quad (6.22)$$

This simple, unified formula for the boundary condition is valid for both $\Delta \geq 0.5$ and $\Delta < 0.5$.

The extension can be easily made using a high order interpolation. Take the second order formulation for example.

Let:

$$\begin{aligned} y_1 &= f_{b8}; \quad y_2 = f_{f8}; \quad y_3 = f_{ff8} \\ x_1 &= 1 \quad ; \quad x_2 = 2 \quad ; \quad x_3 = 3 \\ x &= 1 - \Delta \end{aligned} \quad (6.23)$$

The following three-point Lagrange interpolation is used to obtain f_{w8} :

$$f_{w8} = \sum_{k=1}^3 \left(\prod_{\substack{j=1 \\ j \neq k}}^3 \frac{x - x_j}{x_k - x_j} \right) \cdot y_k \quad (6.24)$$

By requiring

$$f_{w4} = f_{w8} \quad (6.25)$$

the no-slip boundary condition on the wall is ensured.

Letting:

$$\begin{aligned} y_1 &= f_{w4}; \quad y_2 = f_{ff4}; \quad y_3 = f_{fff4} \\ x_1 &= 1 \quad ; \quad x_2 = 2 + \Delta; \quad x_3 = 3 + \Delta \\ x &= \Delta \end{aligned} \quad (6.26)$$

and employing three point Lagrange interpolation again, the distribution function f_f at node f can be readily obtained. In Eq. (6.26), “fff4” donates the node which is one lattice unit away from the node ff along the e_4 -direction.

For non-zero wall velocity, \mathbf{u}_w , it can be easily incorporated into the present unified formulation by adding an additional momentum to f_{w4} : given in (6.25)

$$f_{w\alpha} = f_{w\alpha} + 2w_\alpha \rho \frac{3}{c^2} e_\alpha \cdot \mathbf{u}_w, \quad \text{for } \alpha=4 \quad (6.27)$$

where ρ is the fluid density at the wall which can be obtained by using the extrapolation from the nearby fluid nodes. To avoid computational instability, we simply set $\rho = \rho_f$ for nearly incompressible flow.

6.2.2 Computational Assessment

The flow over a column of circular cylinders is the case used to assess the impact of the boundary treatment on the accuracy of the flow field around a curved boundary. The flow over an oscillating zero-thickness plate is used to assess the temporal continuity of the solution after the application of the presently proposed boundary treatment.

6.2.2.1 Pressure driven channel flows

The grid structure for the 2-D channel computation is shown in Figure 4.3. A constant pressure gradient ∇p along the x-direction is applied as a body force, which is added after the collision step (He *et al.* 1997):

$$\tilde{f}_\alpha(x_i, t) = \tilde{f}_\alpha(x_i, t) - w_\alpha \frac{3}{c^2} \frac{dp}{dx} \mathbf{e}_\alpha \cdot \hat{x} \quad (6.28)$$

where \hat{x} is the unit vector along the x-direction. At steady state, the exact solution for the x-velocity profile is

$$u_{exact}(y) = -\frac{1}{2} \frac{dp}{dx} \frac{H^2}{\rho\nu} (\eta^2 - \eta) \quad (6.29)$$

where $H = N_y - 3 + 2\Delta$ and $\eta = y/H = (j - 2 + \Delta)/H$. To assess the computational error of the LBE solution of the velocity, $u_{LBE}(y)$, the following relative L_2 -norm error is defined

$$E_2 = \frac{\{ \int_0^H [u_{LBE}(y) - u_{exact}(y)]^2 dy \}^{1/2}}{[\int_0^H u_{exact}^2(y) dy]^{1/2}}. \quad (6.30)$$

In the LBE, $\Delta t = \Delta x = \Delta y = 1$. Using the channel height $H = N_y - 3 + 2\Delta$, the dimensionless grid size (or grid resolution) is H^{-1} .

The periodic boundary condition is used at the left and right boundaries of the computational domain. At the lower and upper walls, three wall boundary conditions are used: i) Fillipova and Hänel's method, ii) Bouzidi *et al*'s method and iii) the present method. For the computations reported here, $\nabla p = 10^{-8}$, $\tau = 0.51$ with double precision.

The wall slip velocity $u_w = u_x(y=0)$ is evaluated using a second-order extrapolation based on $u_x(y=\Delta)$, $u_x(y=1+\Delta)$ and $u_x(y=2+\Delta)$. Here we suppose that the velocity profile of the solution is parabolic so that this second order extrapolation will not cause additional extrapolation error. Since the true wall velocity in the pressure driven channel flow is exactly zero, the wall slip velocity u_w provides a measure of the accuracy for the treatment of the wall velocity. Figure 6.15 shows the dependence of wall slip velocity to the H (or the grid resolution H^{-1}). Here u_w is normalized by the centerline velocity

$$u_{max} = - \frac{H^2}{8\rho\nu} \frac{dp}{dx}. \quad (6.31)$$

The second-order convergence of u_w with increasing H is observed clearly in the Figure 6.15 for $\Delta = 0.01, 0.5$, and 0.99 . It is worth noting that although both the present linear and quadratic formulae show the second-order convergence, the magnitude of error of the quadratic form is much smaller.

Figure 6.16 shows the dependence of the relative L_2 -norm error on the channel height H for $\Delta = 0.01, 0.5$, and 0.99 . The second-order accuracy is clearly demonstrated in the range of H investigated. It has been well established that the accuracy of the LBE method for the interior points is of second order. The fact that the overall accuracy is of

second order in the present case means that the accuracy in the boundary condition is at least of second order. This is entirely consistent with the results shown in Figure 6.15, which shows local convergence ($y=0$).

A careful examination of the relative errors in Figure 6.15 and Figure 6.16 indicates that the wall slip velocity in the LBE may be responsible for the error in the flow field. It is thus instructive to compare the shifted velocity profile,

$$u'_{LBE}(y) = u_{LBE}(y) - u_w \quad (6.32)$$

with the exact velocity profile since the error on the wall in the shifted profile is exactly zero now. The relative L_2 -norm error of $u'_{LBE}(y)$ is

$$E_2 = \frac{\left\{ \int_0^{\ell y} [u'_{LBE}(y) - u_{exact}(y)]^2 dy \right\}^{1/2}}{\left[\int_0^{\ell y} u_{exact}^2(y) dy \right]^{1/2}} \quad (6.33)$$

Figure 6.17 shows the result of L_2 -norm error using the Eq. (6.33). The variation of E_2 is non-monotonic because the absolute error is already at the level of machine accuracy. In computation, we use double precision and u_{exact} is around 10^{-4} . From Figure 6.17, it is seen that LBE does not generate any error in the computation for the channel flow; the error is entirely from the boundary treatment. Hence the L_2 -norm error given by the Eq. (6.30) can be used to characterize the error associated with the boundary condition. Figure 6.18 shows the relative error by Eq. (6.31) as a function of Δ using the present method, FH's method, and method of Bouzidi *et al.*, for $0 \leq \Delta \leq 1$. It can be seen that the present linear scheme, linear scheme of Bouzidi *et al.*, and FH's boundary condition have the same order of error for $0 \leq \Delta \leq 1$. Bouzidi *et al.*'s quadratic form gives a large range of error for $0 \leq \Delta \leq 1$, from 10^{-7} to 10^{-2} . The present quadratic formula yields a more uniformly distributed error in the whole range of Δ . It is interesting to note that the error

goes down when Δ increase for the present quadratic formula, which is opposite to the trends shown in other boundary conditions. The present linear and Bouzidi linear boundary conditions have very similar characteristics. Unlike the FH boundary condition, the present boundary conditions suffers no computational instability for $\tau > 0.5$ and any value of Δ between 0 and 1. Even for $\tau=5.0 \times 10^{-4}$, the present boundary condition gives a correct converged result.

6.2.2.2 Stokes first problem: flow due to an impulsively started wall

For a wall located at $y=0$ that is impulsively started, an unsteady Stokes layer of thickness $O(\sqrt{\nu t})$ develops near the wall. For a fixed-grid computation, the error at small time is expected to be large due to insufficient spatial resolution. In the LBE method, this is also compounded by the use of fixed $\tilde{\alpha}$ ($=\tilde{\alpha}=\tilde{\delta}y=1$). In the computation the wall velocity is set as $V=0.1$. Two boundary conditions are used on the wall in the computation, FH boundary condition and present boundary condition. The relaxation time $\tau=0.7$ gives a kinematic viscosity $\nu=0.067$. The Stokes layer is about 0.26 and 0.82 $< \delta y=1$ respectively when $t=1.0$ and 10 (lattice unit). Hence there is not enough spatial resolution when t is small and this will typically cause spatial and temporal oscillation in the solution.

Figure 6.19 shows the velocity profiles at $t=9.5$, 49.5, and 99.5 (in lattice unit). When $t=9.5$, the velocity has large relative error and it becomes negative when y is larger than 4. The oscillation of velocity is not shown in the Figure 6.19 because its absolute value is less than 10^{-3} . Only the result of present linear boundary treatment is shown in Figure 6.19.

Figure 6.20a and Figure 6.20b shows the temporal variation of the relative L_2 -norm error defined as

$$E_2 = \frac{\{\int_0^\infty [u_{LBE}(y,t) - u_{exact}(y,t)]^2 dy\}^{1/2}}{[\int_0^\infty u_{exact}^2(y,t) dy]^{1/2}} \quad (6.34)$$

for $A=0.01, 0.5$, and 0.99 . The large relative errors in the beginning are due to lack of resolution for small time. It should be emphasized that this flow at small time is difficult to deal with for any computational technique due to the singular acceleration and large spatial gradient. It is interesting to note that the present quadratic boundary condition treatment converge to the same magnitude of error while the FH and the present linear boundary formulas diverge at a different level. In such a transient flow, the computational accuracy in the near-wall region is typically dictated by the near-wall spatial resolution which must be smaller than the Stokes layer thickness in order to resolve the local flow field. In a finite difference calculation for such a flow, δt and δx can be independently chosen. If δx is not sufficiently small, further reduction in δt will not lead to improvement in accuracy. As the Stokes layer grows to a certain thickness, the spatial resolution becomes adequate and the accuracy then improves.

6.2.2.3 Steady uniform flow over a column of cylinders

For a uniform flow over a column of circular cylinders of radius r with center-to-center distance denoted by H , symmetry conditions for f_α 's are imposed at $y=\pm H/2$. At the inlet, the uniform velocity, $u=V$, is specified using FH boundary condition. At the exit, a simple extrapolation is used,

$$f_\alpha(N_x, j) = 2f_\alpha(N_x-1, j) - f_\alpha(N_x-2, j) \quad \text{for } \alpha=4, 5, \text{ and } 6. \quad (6.35)$$

On the surface of the circular cylinder, the FH's and the present methods are both used to update the f_a 's. To reduce the effect of the inlet disturbance, the cylinder is placed 20 radii downstream of the inlet. The outlet is placed 35 radii to the right of center of cylinder. In the computation $\tau=0.52$, $u_{inlet}=0.0513$. $Re=100$ based on the diameter of the cylinder and inlet velocity. The drag coefficient is calculated using the momentum exchange method for both boundary condition at two different cylinder center positions (130.0, 65.0) and (130.2, 65.0). Different positions of the cylinder center give different Δ configurations in the boundary description.

Table 6.1 shows the results of drag coefficient using the FH, the present linear, and the present quadratic formulae. The present quadratic formula gives a closer value in comparison with the value of 1.248 given by Fornberg (1991) for both cylinder positions. Figure 6.21 shows the centerline velocity variations before and after the cylinder obtained using two kinds of boundary conditions for the case with the center of the cylinder at (130.0,65). The present linear form and FH's method give very similar velocity profiles in regions with sharp gradient near the front stagnation point, very similar values for the length of the separation bubble, the maximum of the separation bubble velocity, and the recovery of the wake velocity. This result is expected because the results of C_D of the two cases are very close. The present quadratic formula gives slightly different length of the separation bubble, and hence the recovery of the wake velocity.

Table 6.1 Comparison of Drag coefficient using three kinds boundary

X	Present Linear	Present quadratic	FH	C_D , (Fornberg,1991)
130.0	1.275	1.247	1.271	1.248
130.2	1.290	1.251	1.274	

6.2.2.4 Flow over a vertically oscillating zero-thickness flat plate

The computational domain is shown in Figure 6.22. The inlet, lower, upper, and outlet boundary condition are set to be the same as those for flow over a cylinder discusses in the above section. There are 40 grids along the plate. To avoid the crossing of the nodes by the plate, the plate is moving according to:

$$y_{plate} = y_{middle} + 0.49 \cdot \sin(t/1000)$$

In the computation, $\tau=0.52$; $Re=20$ based on the length of plate; $u_{inlet}=0.0083$. FH's method, Bouzidi *et al*'s form, and present linear from boundary conditions are used on the surface of the plate. Figure 6.23a and Figure 6.23b show the variation of drag when plate moves up and down. We can see that there is a discontinuity in the results using FH's and Bouzidi *et al*'s formulae when the plate crosses the middle of the lattice. The present boundary condition gives a treatment results in a smooth temporal variation.

6.2.3 Conclusion

In this work a second-order accurate boundary condition treatment for the lattice Boltzmann equation is proposed. A series of studies are conducted to systematically validate the accuracy and examine the robustness of the proposed boundary condition in steady and unsteady flows involving flat and curved walls. Compared with the existing method for treating boundary condition in the lattice Boltzmann method, the proposed treatment has the following advantages. (i) The scheme is unified for $\Delta \geq 0.5$ and $\Delta < 0.5$ and no discontinuity in boundary treatment. (ii) The boundary treatment is very robust and suffer no computational instabilities in the pressure driven channel flow for $\tau > 0.5$. (iii) Compared with the other curved boundary condition, the present quadratic condition

gives overall better result under otherwise identical computational parameters. (iv) The present scheme is very simple and easily extendable.

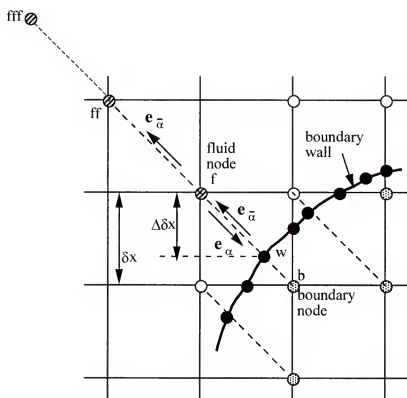


Figure 6.14 Layout of the regularly spaced lattices and curved wall boundary.

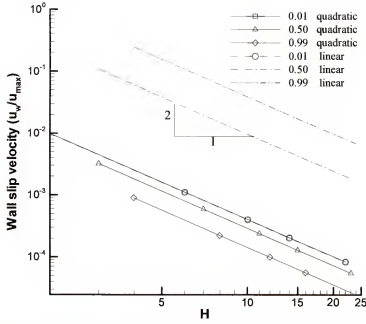


Figure 6.15 Quadratic convergence of the wall slip velocity for present boundary condition in constant pressure driven channel flow .

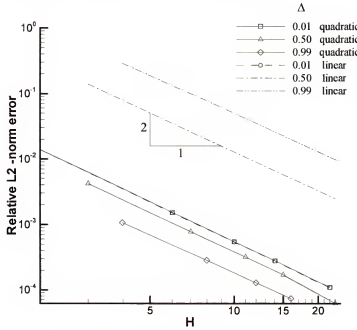


Figure 6.16 Dependence of relative L_2 -norm error using Eq. (6.30) for the present boundary conditions on the lattice resolution H in steady state pressure-driven channel flow simulations.

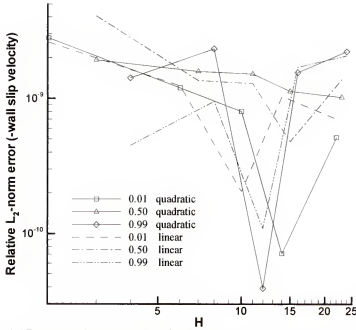


Figure 6.17 Dependence of relative L_2 -norm error using Eq. (6.33) for the present boundary conditions on the lattice resolution H .

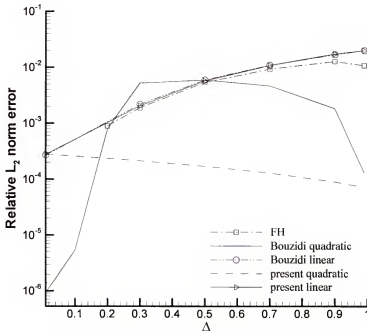


Figure 6.18 Relative L_2 -norm error using Eq. (6.30) as a function of Δ for different boundary conditions in steady state pressure-driven channel flow simulations.

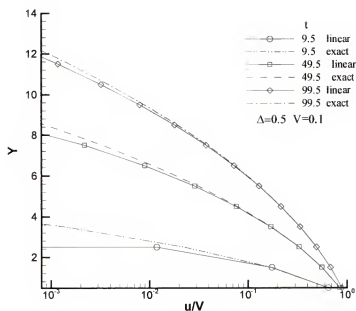


Figure 6.19 Velocity profiles at different time in an impulsively started plate ($\Delta = \frac{1}{2}$) using present linear boundary condition.

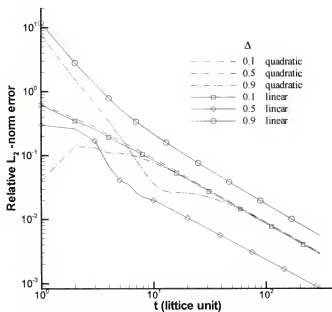


Figure 6.20a Relative L_2 -norm error of the velocity profile $u_x(y)$ during the initial transient of the impulsively started plate with various values of Δ for the present boundary conditions.

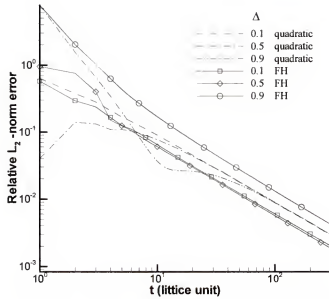


Figure 6.20b Relative L_2 -norm error of the velocity profile $u_x(y)$ during the initial transient of the impulsively started plate with various values of Δ for the present quadratic and FH boundary conditions.

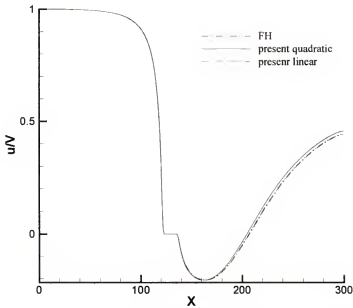


Figure 6.21 Centerline velocity variation for a uniform flow over a column of cylinders with FH, present quadratic, and present linear boundary conditions. Center of cylinder is at (130,65) lattice unit.

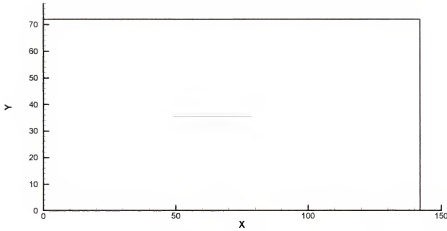


Figure 6.22 Computational domain of for flow over oscillating zero-thickness flat plate.

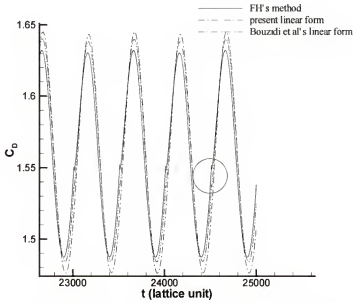


Figure 6.23a Drag coefficient C_D for flow over oscillating zero-thickness flat plate using three different boundary conditions: FH, Bouzidi *et al.* linear, and present linear scheme.

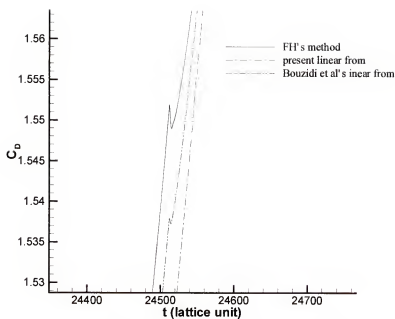


Figure 6.23b Enlarged view of C_D in the circled region in Figure 6.22a when plate crosses the middle of grids. The figure demonstrates the discontinuity in the temporal variation caused by the FH and Bouzidi *et al*'s boundary treatment.

6.3 An Improved Moving Wall Boundary Condition in LBE

6.3.1 Issues in the Moving Boundary Problems

Unlike the problems for flow over a stationary object, where the position and configuration of the boundary do not change with time, moving boundary problems generate additional difficulties during the course of the computation. To facilitate the discussion, a number of terminologies are introduced first. Here we first give some definitions for better description. A *fluid boundary node* (FBN) is a node neighboring the wall and residing the fluid. A *solid boundary node* (SBN) is the node neighboring the wall and inside the solid. A *pre-fluid boundary node* (PFBN) is a fluid node neighboring a fluid boundary node in one direction and will become a fluid boundary node in the future; see Figure 6.24 for details. When a boundary moves, there are two possible changes in the grid arrangement. The first is that a PFBN becomes a new FBN and a FBN becomes a new SBN. The second is that a SBN becomes a new FBN. In the second case information at the newly created FBN is not available directly. Suppose that wall velocity is small, when a PFBN becomes a FBN and directly exchange momentum with the wall, the physical variables at that new FBN node should not have a sudden jump.

To illustrate the issue related to a possible sudden jump in flow variables, a one-dimensional illustration is shown in Figure 6.25. At time t , the boundary is at position 1. After one time step ($t+1$), the boundary is at position 2. In this evolution, the PFBN A becomes a FBN and the FBN B becomes a SBN. Supposed that the wall velocity is small, the distance from the PFBN A to the solid wall at time t and the distance from FBN A to the solid wall at time $t+1$ should only have a very small change, so the physical variables at the PFBN A and FBN A must change smoothly. That means any

sudden jumps of the variables at the node A during this procedure are nonphysical. This is the first problem to be addressed in the moving boundary problem. If the bounce-back condition is used, one would not be surprised to see that the physical variables at node A exhibits a discontinuity when the solid boundary crosses a nodal location. The bounce-back scheme handles the curved wall as zig-zag steps. When the boundary crosses the node B, the real position of boundary will move from the middle of the nodes B and C to the middle of the nodes A and B. This sudden jump of boundary position causes a large jump of variables at the node A.

This kind of jump is not expected to arise when the integrity of curved boundary is honored to the second order accuracy for $0 \leq \Delta \leq 1$. In what follows the FH's boundary condition is analyzed to further illustrate how large the change in physical variables at node A would results from this procedure. For smooth transition, it is needed to maintain $\tilde{f}_5(\mathbf{x}_B)_{t+1} \approx \tilde{f}_5(\mathbf{x}_B)_t$ which will be streamed into node A at $t+1$ and t respectively.

At time t , the node B is the FBN and $\Delta \approx 0$. Using FH's boundary condition treatment, see Eq. (6.16):

$$\tilde{f}_5(\mathbf{x}_C, t-1) = (1-\chi)\tilde{f}_1(\mathbf{x}_B, t-1) + \chi\tilde{f}_1^*(\mathbf{x}_B, t-1) + 2w_5\rho_w\frac{3}{c^2}\mathbf{e}_5 \cdot \mathbf{u}_w \quad (6.36)$$

because of $\Delta \approx 0$, Using Eqs. (6.17) and (6.18)one has

$$\tilde{f}_1^*(\mathbf{x}_B, t-1) = f_1^{eq}(\mathbf{x}_B, t-1) \quad (6.37)$$

$$\chi = -1/(\tau-1) \quad (6.38)$$

Substituting Eq. (6.37) and (6.38) into Eq. (6.36), one obtains

$$\tilde{f}_5(\mathbf{x}_C, t-1) = \tilde{f}_1(\mathbf{x}_A, t-2) + 2w_s \rho_w \frac{3}{c^2} \mathbf{e}_s \cdot \mathbf{u}_w \quad (6.39)$$

The steaming step gives

$$f_5(\mathbf{x}_B, t) = \tilde{f}_5(\mathbf{x}_C, t-1) \quad (6.40)$$

After collision, $f_5(\mathbf{x}_B, t)$ becomes:

$$\tilde{f}_5(\mathbf{x}_B, t) = f_5(\mathbf{x}_B, t) \cdot (1 - \frac{1}{\tau}) + f_5^{eq}(\mathbf{x}_B, t) \cdot \frac{1}{\tau} \quad (6.41)$$

Substituting Eq. (6.40) into Eq. (6.41), one obtains:

$$\tilde{f}_5(\mathbf{x}_B, t) = \tilde{f}_5(\mathbf{x}_C, t-2) \cdot (1 - \frac{1}{\tau}) + f_5^{eq}(\mathbf{x}_B, t) \cdot \frac{1}{\tau} \quad (6.42)$$

The equilibrium distribution function in Eq. (6.42) can be determined as

$$f_\alpha^{eq}(\mathbf{x}_B, t) = w_\alpha \rho(\mathbf{x}_B, t) [1 + \frac{3}{c^2} \mathbf{e}_\alpha \cdot \mathbf{u}_B(t) + \frac{9}{2c^4} (\mathbf{e}_\alpha \cdot \mathbf{u}_B(t))^2 - \frac{3}{2c^2} (\mathbf{u}_B(t))^2] \quad (6.43)$$

where $\alpha=5$. Using equations (6.36)-(6.43) and the condition that $\mathbf{u}_B(t) \approx \mathbf{u}_w$, since $\Delta \approx 0$ one obtains:

$$\begin{aligned} \tilde{f}_5(\mathbf{x}_B, t) = & (\tilde{f}_1(\mathbf{x}_A, t-2) + 2w_s \rho_w \frac{3}{c^2} \mathbf{e}_s \cdot \mathbf{u}_w) \cdot (1 - \frac{1}{\tau}) + \\ & w_s \rho(\mathbf{x}_B, t) [1 + \frac{3}{c^2} \mathbf{e}_s \cdot \mathbf{u}_w + \frac{9}{2c^4} (\mathbf{e}_s \cdot \mathbf{u}_w)^2 - \frac{3}{2c^2} \mathbf{u}_w \cdot \mathbf{u}_w] \cdot \frac{1}{\tau} \end{aligned} \quad (6.44)$$

At time $t+\Delta$, the node A is the new FBN, and Δ changes from $\Delta \approx 0$ to $\Delta \approx 1$. From FH's boundary condition one obtains:

$$\tilde{f}_5(\mathbf{x}_B, t) = \tilde{f}_1(\mathbf{x}_A, t) \cdot (1 - \frac{1}{\tau}) + f_1^{(*)}(\mathbf{x}_B, t) \cdot \frac{1}{\tau} + 2w_s \rho_w \frac{3}{c^2} \mathbf{e}_s \cdot \mathbf{u}_w \quad (6.45)$$

and

$$f_1^{(*)}(\mathbf{x}_B, t) = w_H \rho(\mathbf{x}_A, t) \left[1 + \frac{3}{c^2} \mathbf{e}_I \cdot \mathbf{u}_w + \frac{9}{2c^4} (\mathbf{e}_I \cdot \mathbf{u}_A(t))^2 - \frac{3}{2c^2} (\mathbf{u}_A(t))^2 \right] \quad (6.46)$$

Using equations (6.45) and (6.46) one obtains:

$$\begin{aligned} \tilde{f}_5(\mathbf{x}_B, t) = \tilde{f}_1(\mathbf{x}_A, t) \cdot \left(1 - \frac{1}{\tau}\right) + (w_H \rho(\mathbf{x}_A, t) \left[1 + \frac{3}{c^2} \mathbf{e}_I \cdot \mathbf{u}_w \right. \\ \left. + \frac{9}{2c^4} (\mathbf{e}_I \cdot \mathbf{u}_A(t))^2 - \frac{3}{2c^2} (\mathbf{u}_A(t))^2 \right]) \cdot \frac{1}{\tau} + 2w_S \rho \frac{3}{c^2} \mathbf{e}_S \cdot \mathbf{u}_w \end{aligned} \quad (6.47)$$

Subtracting Eq. (6.44) from (6.47), one obtains:

$$\begin{aligned} \tilde{f}_5(\mathbf{x}_B, t+1) - \tilde{f}_5(\mathbf{x}_B, t) = [\tilde{f}_1(\mathbf{x}_A, t) - \tilde{f}_1(\mathbf{x}_A, t-2)] \left(1 - \frac{1}{\tau}\right) + \{-2w_S \rho \frac{3}{c^2} \mathbf{e}_S \cdot \mathbf{u}_w + \\ w_S \rho(\mathbf{x}_B, t) \left[1 + \frac{3}{c^2} \mathbf{e}_S \cdot \mathbf{u}_w + \frac{9}{2c^4} (\mathbf{e}_S \cdot \mathbf{u}_w)^2 - \frac{3}{2c^2} \mathbf{u}_w \cdot \mathbf{u}_w \right] - \\ w_H \rho(\mathbf{x}_A, t+1) \left[1 + \frac{3}{c^2} \mathbf{e}_I \cdot \mathbf{u}_w + \frac{9}{2c^4} (\mathbf{e}_I \cdot \mathbf{u}_A(t+1))^2 - \frac{3}{2c^2} (\mathbf{u}_A(t+1))^2 \right]\} \cdot \frac{1}{\tau} \end{aligned} \quad (6.48)$$

In the ideal case, as the solid moves crossing the node B, variables at position A should not experience a sudden jump. This implies that the LHS terms are small and would require the following conditions in Eq. (6.48):

$$\rho(\mathbf{x}_A, t+1) \approx \rho(\mathbf{x}_B, t) ; \quad \mathbf{u}_A(t+1) \approx \mathbf{u}_w \quad (6.49)$$

In the actual computation, these conditions cannot be satisfied because variables appearing in Eq. (6.49) belong to the different grids at time t and $t+1$.

The second problem in moving boundary problems is about the creation of new fluid nodes (see Figure 6.26). The SBN at the location E at time t becomes a new FBN at time $t+1$. At time $t+1$, the information for f 's at the node E does not exist and need to be specified using the information from the nodes around the new FBN E. There are different ways to specify the distribution function at the node E. Here we first use a

linear extrapolation to give all distribution functions at node D. An additional step is then taken to reduce the possible oscillation caused by this linear extrapolation. This additional step can be described as placing an additional collision in the fluid nodes neighboring the new FBN and then streaming \tilde{f}_α from the neighboring nodes to the new FBN E. Then a boundary condition is needed to supply $f_{\bar{\alpha}}$, where $e_{\bar{\alpha}} = -e_\alpha$. In the second step only the value of f_α at the new FBN is changed. Although a collision step has been added at the nodes neighboring the new FBN, the values of f_α at those nodes do not change. The post-collision values are used only to stream to the new FBN E.

The third problem appearing in the moving boundary problem is the way the singularity is handled. For the stationary boundary condition, the ability to handle the spatial and temporal accuracy and geometric singularity is very important. With the geometric singularity such as a sharp convex corners, the solution may possess spatial oscillation and cause computational instability as well as reduced accuracy of the solution. In the moving boundary problem, the geometric singularity causes even a bigger problem because the moving boundary changes the position of the singularity and redistributes the Δ in space.

6.3.2 Formulation for the Moving Boundary Condition

In LBE, the evolution of f_α 's involves collision and streaming steps. To complete the streaming step, \tilde{f}_α at solid boundary node \mathbf{x}_b in Figure 6.24 must be specified. Referring to Figure 6.24, after the streaming step, f_{f4} at the fluid node \mathbf{f} needs to be assigned while f_{b8} and f_{f8} are known. Using linear interpolation, f_{w8} can be found as:

$$f_{w8} = f_{f8} + (f_{b8} - f_{f8}) * \Delta \quad (6.50)$$

where f_{w8} is the distribution function at the point on the wall and the link along the e_8 direction intersects with the solid wall. To ensure the no-slip boundary condition at w, an additional term is need to account for the momentum exchange with the solid:

$$f_{w4} = f_{w8} + 2w_4\rho_w \frac{3}{c^2} e_4 \cdot \mathbf{u}_w \quad (6.51)$$

where ρ_w is the fluid density at the wall, which can be obtained using a suitable extrapolation.

The key step in designing this moving boundary condition is to add an additional collision step corresponding to the boundary velocity \mathbf{u}_w on the wall to obtain \tilde{f}_{w4} and then to stream it by one lattice in the direction of e_4 .

$$\tilde{f}_{w4} = f_{w4} \cdot (1 - \frac{1}{\tau}) + f_{w4}^{eq} \cdot \frac{1}{\tau} \quad (6.52)$$

where

$$f_{w4}^{eq} = w_4 \rho_w [1 + \frac{3}{c^2} e_4 \cdot \mathbf{u}_w + \frac{9}{2c^4} (e_4 \cdot \mathbf{u}_w)^2 - \frac{3}{2c^2} (\mathbf{u}_w)^2] \quad (6.53)$$

Based on the assumption of the slow flow, an interpolation is used to obtain to f_{f4} as,

$$f_{f4} = f_{w4} + (\tilde{f}_{w4} - f_{w4}) \cdot \Delta \quad (6.54)$$

In this approach, the boundary condition does not need to be treated differently for $\Delta \geq 0.5$ and $\Delta < 0.5$. However this additional collision step is the key difference between this scheme and the one described in Section 6.2.

6.3.3 An Analysis on the Pressure Change near the Wall and Momentum Exchange between Fluid and Solid

When a boundary crosses a nodal location, it is desirable to keep the physical variables at the new FBN and the momentum flux between the fluid and the solid continuous. To

illustrate that the present boundary condition can meet both requirements, the one dimension example is again used.

First we show that physical variables at new FBN can be maintained continuous (see Figure 6.25) when the solid boundary crosses a node. As shown in Section 6.3.1, $\tilde{f}_5(\mathbf{x}_B)$ needs to be examined to see if the temporal changes of variables at node A are smooth. At time t , the node B is the FBN and $\Delta \approx 0$. Using the present boundary condition, from Eq. (6.50) one has:

$$f_1(\mathbf{x}_w, t) \approx f_1(\mathbf{x}_B, t) \quad (6.55)$$

From Eq. (6.51), one has

$$f_5(\mathbf{x}_w, t) = f_1(\mathbf{x}_B, t) + 2w_\alpha \rho \frac{3}{c^2} \mathbf{e}_\alpha \cdot \mathbf{u}_w \quad (6.56)$$

Equation (6.54) gives

$$\tilde{f}_5(\mathbf{x}_B, t) = \tilde{f}_1(\mathbf{x}_A, t-1) + 2w_\alpha \rho \frac{3}{c^2} \mathbf{e}_\alpha \cdot \mathbf{u}_w \quad (6.57)$$

After one collision step:

$$\begin{aligned} \tilde{f}_5(\mathbf{x}_B, t) &= f_5(\mathbf{x}_B, t) \cdot (1 - \frac{1}{\tau}) + f_5^{eq}(\mathbf{x}_B, t) \cdot \tau \\ &= (\tilde{f}_1(\mathbf{x}_A, t-1) + 2w_\alpha \rho \frac{3}{c^2} \mathbf{e}_\alpha \cdot \mathbf{u}_w) \cdot (1 - \frac{1}{\tau}) + f_5^{eq}(\mathbf{x}_B, t) \cdot \tau \end{aligned} \quad (6.58)$$

The equilibrium distribution in Eq. (6.58) is determined as:

$$f_\alpha^{eq}(\mathbf{x}_B, t) = w_\alpha \rho(\mathbf{x}_B, t) [1 + \frac{3}{c^2} \mathbf{e}_\alpha \cdot \mathbf{u}_B(t) + \frac{9}{2c^4} (\mathbf{e}_\alpha \cdot \mathbf{u}_B(t))^2 - \frac{3}{2c^2} (\mathbf{u}_B(t))^2] \quad (6.59)$$

At time $t+1$, the node A is the new FBN and $\Delta \approx 1$. Using the present boundary condition, one obtains:

$$f_5(\mathbf{x}_W, t+1) = \tilde{f}_1(\mathbf{x}_A, t+1) + 2w_\alpha \rho_w \frac{3}{c^2} \mathbf{e}_\alpha \cdot \mathbf{u}_w \quad (6.60)$$

After one collision step at the wall, we obtain:

$$\begin{aligned} \tilde{f}_5(\mathbf{x}_W, t+1) &= f_5(\mathbf{x}_W, t+1) \cdot (1 - \frac{1}{\tau}) + f_5^{eq}(\mathbf{x}_W, t+1) \cdot \tau \\ &= \tilde{f}_1(\mathbf{x}_A, t) + 2w_\alpha \rho \frac{3}{c^2} \mathbf{e}_\alpha \cdot \mathbf{u}_w \cdot (1 - \frac{1}{\tau}) + f_5^{eq}(\mathbf{x}_B, t+1) \cdot \tau \end{aligned} \quad (6.61)$$

where the equilibrium distribution function is given by:

$$f_\alpha^{eq}(\mathbf{x}_W, t+1) = w_\alpha \rho(\mathbf{x}_W, t+1) [1 + \frac{3}{c^2} \mathbf{e}_\alpha \cdot \mathbf{u}_w + \frac{9}{2c^4} (\mathbf{e}_\alpha \cdot \mathbf{u}_w)^2 - \frac{3}{2c^2} \mathbf{u}_w \cdot \mathbf{u}_w] \quad (6.62)$$

Subtracting Eq. (6.58) from (6.61), one obtains

$$\begin{aligned} \tilde{f}_5(\mathbf{x}_B, t+1) - \tilde{f}_5(\mathbf{x}_B, t) &= [\tilde{f}_1(\mathbf{x}_A, t+1) + \tilde{f}_1(\mathbf{x}_A, t-1)] \cdot (1 - \frac{1}{\tau}) \\ &\quad + [f_5^{eq}(\mathbf{x}_w, t+1) - f_5^{eq}(\mathbf{x}_B, t)] \cdot \tau \end{aligned} \quad (6.63)$$

Since $\mathbf{x}_B \approx \mathbf{x}_W$, $\mathbf{u}_B(t) \approx \mathbf{u}_W$ and $\rho(\mathbf{x}_W, t+1) \approx \rho(\mathbf{x}_B, t)$, one has

$$\tilde{f}_5(\mathbf{x}_B, t+1) \approx \tilde{f}_5(\mathbf{x}_B, t) \quad (6.64)$$

This shows that the present boundary condition can ensure smooth variation of f 's at node A.

In LBE, the momentum exchange is used to find the force acted on the object. The momentum exchange should not experience an artificially large fluctuation when a solid boundary crosses anodal line. Indeed, as will be presented next, the present boundary condition can satisfy this requirement as well. In the derivation the node A is used as the reference point (see Figure 6.25). At time t , the momentum exchange $F_5(t)$ in directions \mathbf{e}_1 and \mathbf{e}_5 is:

$$F_5(t) = \tilde{f}_1(\mathbf{x}_B, t) + \tilde{f}_1(\mathbf{x}_A, t-1) + 2w_5\rho\frac{3}{c^2}\mathbf{e}_5 \cdot \mathbf{u}_w \quad (6.65)$$

where $\tilde{f}_1(\mathbf{x}_B, t)$ is determined by:

$$\tilde{f}_1(\mathbf{x}_B, t) = \tilde{f}_1(\mathbf{x}_A, t-1) \cdot (1 - \frac{1}{\tau}) + f_1^{eq}(\mathbf{x}_B, t) \cdot \tau \quad (6.66)$$

Substituting Eq. (6.66) into (6.65), we obtain:

$$F_5(t) = \tilde{f}_1(\mathbf{x}_A, t-1) + \tilde{f}_1(\mathbf{x}_A, t-1) \cdot (1 - \frac{1}{\tau}) + f_1^{eq}(\mathbf{x}_B, t) \cdot \tau + 2w_5\rho\frac{3}{c^2}\mathbf{e}_5 \cdot \mathbf{u}_w \quad (6.67)$$

At time $t+1$, the momentum exchange is:

$$F_5(t+1) = \tilde{f}_1(\mathbf{x}_A, t+1) + (\tilde{f}_1(\mathbf{x}_A, t+1) + 2w_5\rho\frac{3}{c^2}\mathbf{e}_5 \cdot \mathbf{u}_w) \cdot (1 - \frac{1}{\tau}) + f_5^{eq}(\mathbf{x}_w, t+1) \cdot \tau \quad (6.68)$$

Adding $f_1^{eq}(\mathbf{x}_w, t+1) \cdot \tau$ on both sides of Eq. (6.68), we obtain

$$F_5(t+1) = \tilde{f}_1(\mathbf{x}_A, t+1) + \tilde{f}_1(\mathbf{x}_A, t+1) \cdot (1 - \frac{1}{\tau}) + f_1^{eq}(\mathbf{x}_w, t+1) \cdot \tau + 2w_5\rho\frac{3}{c^2}\mathbf{e}_5 \cdot \mathbf{u}_w \quad (6.69)$$

Subtracting Eq. (6.67) from (6.69), one obtains,

$$F_5(t+1) - F_5(t) = [\tilde{f}_1(\mathbf{x}_A, t+1) - \tilde{f}_1(\mathbf{x}_A, t-1)](2 - \frac{1}{\tau}) + f_1^{eq}(\mathbf{x}_w, t+1) \cdot \tau - f_1^{eq}(\mathbf{x}_B, t) \cdot \tau \quad (6.70)$$

Since $f_1^{eq}(\mathbf{x}_w, t+1) \approx f_1^{eq}(\mathbf{x}_B, t)$ and $\tilde{f}_1(\mathbf{x}_A, t+1) \approx \tilde{f}_1(\mathbf{x}_A, t-1)$, one obtains

$$F_5(t+1) \approx F_5(t) \quad (6.71)$$

This demonstrates that the momentum exchange can be maintained continuous from t to $t+1$ when a lattice node is crossed by the solid boundary.

6.3.4 Computational Assessment

In what follows, we consider flow problems without singularity to test the accuracy of the present boundary condition. First we consider a channel flow under constant pressure gradients with analytic solutions to assess the spatial accuracy. In this case the wall velocity is zero. Flow over impulsively started cylinder and flow over stationary cylinder in a channel are then used to test the accuracy of moving boundary treatments and Galilean invariance. Finally flow due to a vertically oriented, infinitely long plate moving sinusoidally in the x -direction is considered. The present boundary condition and FH's boundary condition are used for comparison.

6.3.4.1 Pressure driven channel flows

The configuration and parameters of this computation are the same as those of the case in Section 6.2.3.1. The second order convergence of u_w is observed for $\Delta=0.01, 0.5$, and 0.99 in Figure 6.27.

6.3.4.2 Flow over a impulsively started cylinder in a channel

The channel has the dimension $L \times W = 401 \times 141$. The initial position of the cylinder center is at the middle point of the domain in the y direction. The radius of cylinder is 15.5 lattice unit. At $t=0$, the cylinder is at rest. Then the cylinder is impulsively started with a constant velocity $U=0.00215$ moving in the negative x -direction. On the left, upper and lower boundaries the velocity is set to be zero. On the right side boundary, the zeroth order extrapolation is applied for f_a 's. With $\tau=0.52$, the Reynolds number based on the diameter of the cylinder is 10. When the distance crossed by moving cylinder exceeds 1 unit of lattice, the entire grid and cylinder is moved back to the right by one unit to ensure that the distance from the left side

remains constant with a lattice. This configuration of the flow is nearly equivalent to the flow with the following initial and boundary conditions: the fluid and cylinder is at rest at $t=0$; then the fluid, the upper wall and lower wall start to move impulsively with velocity $U=0.00215$ with the velocity of the left boundary is also set to $U=0.00215$. However there is still a major computational difference. For the stationary cylinder, the number of solid boundary nodes is fixed. For the moving cylinder, the number changes with time. Thus, it is expected that there will be larger transient variation in the moving cylinder case.

Figure 6.28a shows the history of the drag on the cylinder for both cases. It is seen that the transient drag with two boundary treatments agree with each other very well. Figure 6.28b shows the final stage of computation when steady state is expected. The oscillation caused by the moving boundary is about 4% of the mean value. In the force evaluation, the momentum exchange is used. In this case, it is estimated that the method of force evaluation and the introduction of the new fluid nodes are responsible for most part of the oscillation. Figure 6.29a and Figure 6.29b show the density contour in the region near the cylinder with the density being normalized by the largest density in front of the cylinder. The same density level is set for both cases. The oscillation in density contour is very small in both cases, but the spatial distributions of density in space are not exactly the same. This difference is attributed to the change of the number of the boundary nodes in the moving cylinder case.

6.3.4.3 A flow due to a sinusoidally oscillating Plate

The computational domain is shown in Figure 6.30. The velocity $V=0.0$ is set as the initial condition. A periodic boundary condition is imposed at the upper and lower

boundaries. The zeroth order extrapolation is used at the left and right boundaries. The plate is moving at the velocity:

$$u=U*\sin(6.28/1000*t), U=0.01 \quad (6.72)$$

The height of plate is 11 lattice unit. On the surface of plate, the FH's boundary condition and present moving wall boundary condition are used. The number of new FBNs generated by moving plate equals to the height of the plate in the lattice unit.

Figure 6.31 and Figure 6.32 show the history of pressure at a point in the fluid field that is one grid away to the left of the plate in x-direction using two different boundary condition treatments. The pressure at this specified point is obtained by linearly interpolating the values from the FBN and PFBN on the left side of the plate. The present boundary condition produces little artificial small-scale fluctuations as the plate crosses a nodal line. However, FH's treatment results noticeable small scale, large-amplitude disturbances in the temporal pressure variation. It is interesting to note that present boundary condition can also reduce the pressure jump when new fluid nodes generate.

6.3.5 Conclusions

Various issues associated with the moving boundary problem have been examined. A new boundary condition, which can ensure the continuity of the flow variable as well as momentum exchange as boundary crosses the lattice nodes, is presented. Various cases show that the proposed boundary condition can greatly reduce the oscillation caused by the moving boundary. The new boundary condition is easy to implement.

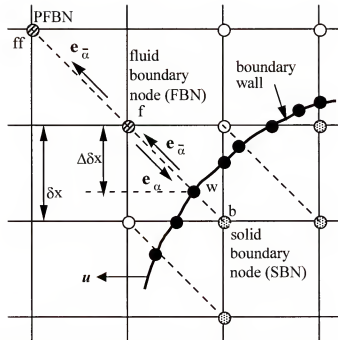


Figure 6.24 Layout of the regularly spaced lattices and curved wall boundary and definition of nodes.

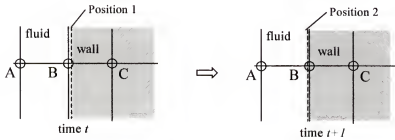


Figure 6.25 The generation of a new FBN and SBN in a moving boundary problem.

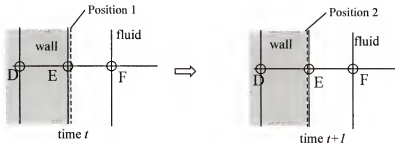


Figure 6.26 The generation of a new FBN in a moving boundary problem.

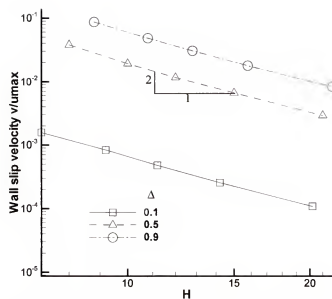


Figure 6.27 Quadratic convergence of the wall slip velocity for present boundary condition in a constant pressure driven channel flow.

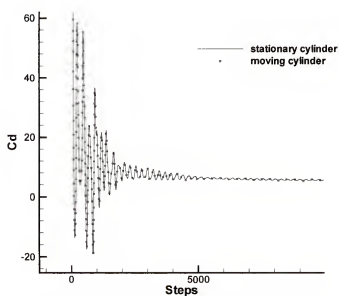


Figure 6.28a Convergent history of drag coefficient.

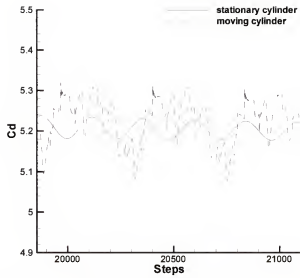


Figure 6.28b Drag coefficient at the final stage of computation.

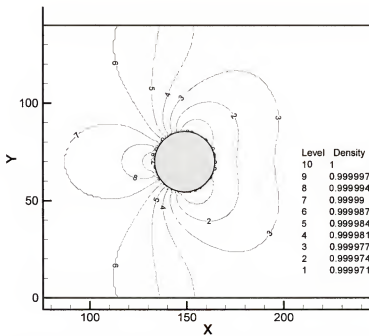


Figure 6.29a Density contour for the flow over a stationary cylinder.

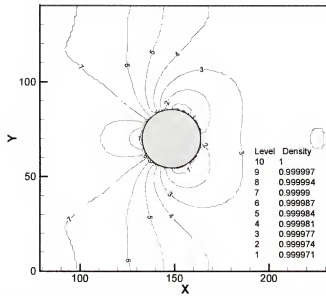


Figure 6.29b Density contour for the flow over a moving cylinder.

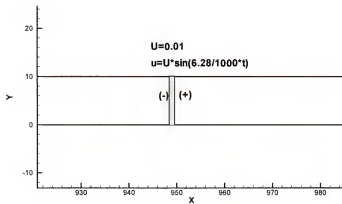


Figure 6.30 Computational domain for flow due to a sinusoidally oscillation plate.

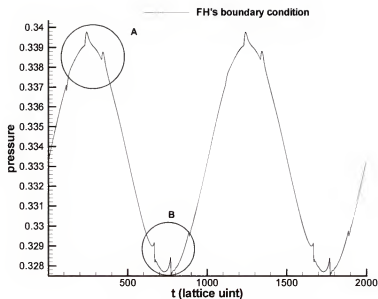


Figure 6.31a History of pressure at a point which is one grid away to the left of the plate. The details of circle regions A and B are given in Figure 6.31b and Figure 6.31c.

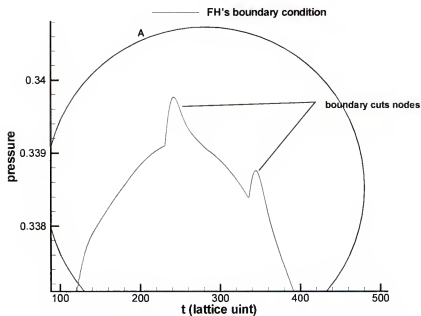


Figure 6.31b Enlarged region A in Figure 6.31a

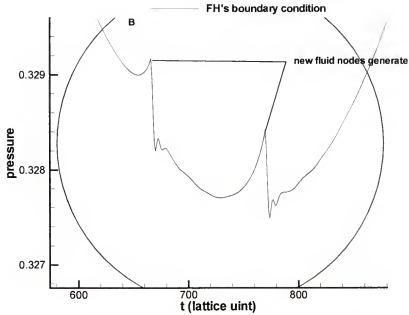


Figure 6.31c Enlarged region B in Figure 6.31a
 Figure 6.31 Pressure characteristic at a point which is one grid away to the left of the plate. FH's boundary condition is used in computation.

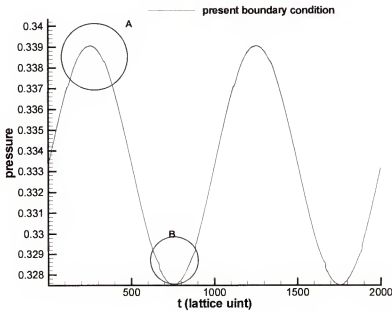


Figure 6.32a History of pressure at a point which is one grid away to the left of the plate. The details of circle regions A and B are given in Figure 6.32b and Figure 6.32c.

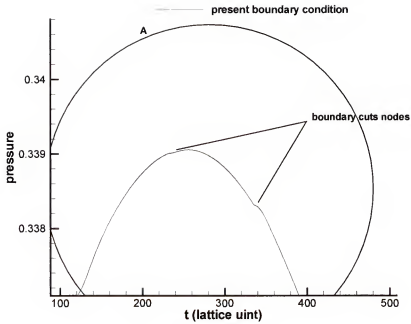


Figure 6.32b Enlarged region A in Figure 6.32a

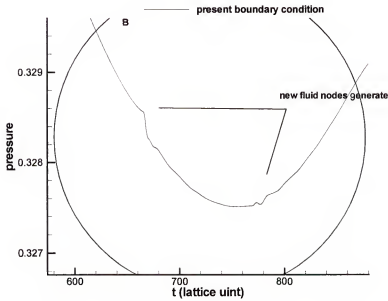


Figure 6.32c Enlarged region B in Figure 6.32a

Figure 6.32 Pressure characteristic at a point which is one grid away to the left of the plate. Present boundary condition is used in computation.

CHAPTER 7

SUMMARY AND FUTURE WORKS

Compared with NS equations, the LBE method has its own advantages and disadvantages. The disadvantages of LBE method include: firstly it require large a mount of memory to store the distribution function; secondly solution is generally dependent on the time which means capturing a steady state solution need a long time. The advantages of LBE include: firstly scheme is simple; secondly evolution rule is local and computation is easy to be parallelized.

The issues needed to be addressed in the LBE method include:

1. Increasing the efficiency of computation
2. Implementing LBE in high Re number flows
3. Evaluating the force on a solid body in the LBE simulation
4. Improving the boundary treatments
5. Implementing LBE in moving boundary problems
6. Implementing LBE in turbulent flows
7. implementing LBE in compressible flows

In this dissertation, most effort has been put to address the issues in the first five topics mentioned above. This effort includes:

1. A multi-block method in the LBE method

To increasing the computational efficiency in the LBE method, a multi-block method is developed. In this multi-block method:

- The formulae for information exchange at the interface between coarse and fine blocks are derived to ensure the mass and momentum conservation, and stress continuity across the interface.
- A customized time matching between coarse and fine blocks is designed to ensure the smooth transferring of physical variables between coarse and fine blocks.
- A symmetric, high-order interpolation is used obtain spatial distribution of the fine-block variables at the interface in order to prevent artificial spurious oscillations in the flow from being originated from the interface.

Studying cases show that the multi-block method can greatly increase the computational efficiency of LBE method without loss of accuracy.

2. Multi-time-relaxation model in the LBE method

In computing high Re flows, the computational stability will become a big issue. Computational stability depends on the LBE models, the boundary conditions, and the Re number of flow. In the present study, two different LBE models, SRT model and MRT model, are studied in various cases involving singularity at high Reynolds number. It is found that

- The difference between the two models can be non-local. The MRT model in general provides smoother variations of the macroscopic quantities and has much smaller regions of the oscillation near a singularity.

- Since the spatial oscillation is often accompanied by the high frequency pressure (acoustic) waves in transient simulations, the MRT model also offers a better convergence toward steady state as well.

3. Force evaluation on the solid body in the LBE method

Evaluating the force acted on a body by the fluid is a very important issue in the simulation. In conjunction with the LBE method, two methods for force evaluation are examined: one is based on stress integration on the surface and the other is based on momentum exchange between the fluid and the solid boundary. The momentum exchange method is found to be very simple to implement while the integration of stress requires tedious evaluation of the details of the surface geometry in addition to the extrapolation for stress related variable on the surface. The momentum exchange method gives a good result and thus is recommended for force evaluation.

4. The open boundary treatment

An open boundary condition based on the known equilibrium and non-equilibrium values was proposed. Compared with conventional bounce scheme, it was found that new treatment can

- Avoid strong coupling or interaction between flow variables at the boundary and at the interior of the flow field.
- Improve the convergence rate to steady state, stability of computation, and quality of the solution.

5. A unified treatment for solid wall boundary

A unified second-order accurate boundary condition treatment for the solid wall is developed. This new treatment is:

- Unified for $\Delta \geq 0.5$ and $\Delta < 0.5$ and there is no discontinuity in the boundary treatment.
- Very robust to implement and suffers little computational instabilities
- Overall better in the computational performance when using three-points interpolation compared with other boundary treatments.

6. An improved moving wall boundary condition

Moving boundary problems generate additional difficulties during the computation., which include

- Phase change, which means a node in the fluid may become a node inside solid and *vice versa*.
- Change of the Position of Singularity
- The change of the number of nodes which are used in the force evaluation using momentum exchange method.

A new boundary condition specifically designed for cases with moving wall is presented to solve the phase change problem. As the boundary crosses the lattice nodes, analysis shows that new boundary treatment can

- ensure the continuity of the flow variable near the solid boundary
- ensure the continuity of momentum exchange

Computational results demonstrate that the proposed boundary condition can reduce the oscillation caused by the moving boundary when compared with the solution obtained using other boundary treatments.

For the moving boundary problem, a stronger interaction exists between the solid and fluid and the accuracy of the force acting on the body plays even a bigger role since it feeds back to the flow field through the boundary condition. In the future work, more accurate force evaluation scheme needs to be developed to account for the changing configurations of the solid boundary. Strategies must be developed to reduce the transient oscillation in the flow variables as the boundary moves in the flow field. Especially, there is noise in pressure field in the flow near a solid body. This noise exists even in the flow over a stationary body, although in this case it will not cause big problem in simulation. When boundary moves this kind of noise will generate spatial and temporal pressure oscillation in computation. To remove such kind of noise in the pressure field is another goal in the study of moving boundary problem.

In the present study, only laminar flows are being considered. When Reynolds number increase, flows will become turbulent, so it is necessary to introduce turbulence model in computation to extend the application of the LBE method

LIST OF REFERENCES

- Benzi, R., Succi, S., Vergassola, M., The lattice Boltzmann equation theory and applications, *Phys. Reports* **222**, 145-197 (1992).
- Behrend, Q., Solid-fluid boundaries in particle suspension simulation via the lattice boltzmann method, *Phys. Rev. E*, **52**, 1164-1175 (1995).
- Bhatnagar, P. L., Gross, E. P., Krook, M., A model for collision processes in gases, I. small amplitude processes in charged and neutral one-component system. *Phys. Rev.* **94**, 511-525 (1954).
- Broadwell, J. E., Study of rarefied shear flow by the discrete velocity method, *J. Fluid Mech.* **19**, 401-404 (1964).
- Bouzidi, M., d'Humieres, D., Lallemand, P., Luo, L.-S, Lattice Boltzmann equation on a two-dimensional rectangular grid, *J. Comp. Phys.* **172**, 704-717 (2001).
- Bouzidi, M., dFirdaouss, M., Lallemand, P., Momentum transfer of a lattice Boltzmann fluid with boundaries. *Phys. Fluids* **13**, 3452-3459 (2001).
- Chen, H., Chen, S., Matthaeus, W. H., Recovery of the Navier-Stokes equations using a lattice-gas Boltzmann method, *Phys. Rev. A*, **45**, R5339-R5342 (1992).
- Chen, S., Martinez, D., Mei, R., On boundary conditions in lattice Boltzmann method, *Phys. Fluids* **8**, 2527-2536 (1996).
- Chen, S., Doolen, G. D., Lattice Boltzmann method for fluid flows, *Ann. Rev. Fluid Mech.* **30**, 329-364 (1998).
- Cornubert, R., Dhumieres, D., Levermore, D., A Knudsen layer theory for lattice gases, *Physica D*, **47**, 291-297 (1991)
- d'Humieres, D., Generalized lattice Boltzmann equations, *In Rarefied Gas Dynamics: Theory and Simulations*, ed. by D. Shizgal and D.P. Weaver. Prog. in Astro. Aero., Vol. **159**, 450-458 (1992).
- d'Humieres, D., Ginzburg, I., Krafczyk, M., Lallemand, P., Luo, L., Multiple-relaxation-time lattice Boltzmann models in three dimensions, *Phil. Trans. R. Soc. Lond. A* **360**, 437-451 (2002)

Drela, M., Giles, M. B., Viscous-inviscid analysis of transonic and low Reynolds number airfoils. *AIAA J.* **25**, 1347-1355 (1987).

Filippova, O., Hänel, D. Grid refinement for lattice-BGK models, *J. Comp. Phys.* **147**, 219-228 (1998).

Fletcher, C. A. J., *Computational Techniques for Fluid Dynamics*, Vols. I and II, Springer-Verlag, New York (1988).

Fornberg, B., Steady incompressible flow past a row of circular cylinder, *J. Fluid Mechanics* **225**, 655-671 (1991).

Frisch, U., Hasslacher, B., Pomeau, Y., Lattice-Gas Automata for the Navier-Stokes Equations, *Phys. Rev. Lett.* **56**, 1505-1508 (1986).

Ghia, U., Ghia, K. N., Shin, C. T., High-Re solution for incompressible flow using the Navier-Stokes equations and a multigrid method, *J. Comp. Phys.* **48**, 387-411 (1982).

Ginzbourg, I., and Alder, P. M., Boundary flow condition analysis for the three-dimensional lattice Boltzmann model, *J. Phys. II France* **4**, 191-214 (1994).

Gruna, D.W., Lattice methods for modeling hydrodynamics, Ph.D. Dissertation, Colorado State University, (1993)

Hardy, J., de Pazzis, O., Pomeau, Y., Molecular dynamics of a classical lattice gas: transport properties and time correlation functions, *Phys. Rev. A*, **13**, 1949-1961 (1976).

He, X., Luo, L.-S., A priori derivation of the lattice Boltzmann equation, *Phys. Rev. E* **55**, R6333-R6336 (1997a).

He, X., Luo, L.-S., Theory of the lattice Boltzmann equation: From Boltzmann equation to lattice Boltzmann equation, *Phys. Rev. E* **56**, 6811-6817 (1997b).

He, X., Luo, L.-S., Lattice Boltzmann model for the incompressible Navier-Stokes equation. *J. Stat. Phys.* **88**, 927-944 (1997c).

He, X., Zou, Q., Luo, L.-S., Dembo, M., Some progress in the lattice Boltzmann method. Part I, non-uniform mesh grids. *J. Comp. Phys.* **129**, 357-363 (1996)

He, X., Zou, Q., Luo, L.-S., Dembo, M., Analytic solutions and analysis on non-slip boundary condition for the lattice Boltzmann BGK model, *J. Stat. Phys.* **87**, 115-136 (1997).

Higuera, F. J., Jimenez, J., Boltzmann approach to lattice gas simulations, *Europhys. Lett.* **9**, 663-668 (1989).

Inamuro, T., Yoshino, M., Ogino, F., A Non-slip boundary condition for lattice Boltzmann Simulations, *Phys. Fluids*. **7**, 2928-2930 (1995).

Kandhai, D., Soll, W., Chen, S., Hockstra, A., Soot, P., Finite-difference lattice-BGK methods on nested grids, *Computer Physics Communications* **129**, 100-109 (2000).

Koelman, J. M. V. A., A simple lattice Boltzmann scheme for Navier-Stokes fluid flow, *Europhys. Lett.* **15**, 603-607 (1991).

Ladd, A. J. C., Numerical simulation of particular suspensions via a discretized Boltzmann equation. Part 1. Theoretical foundation, *J. Fluid Mech.* **271**, 285-309 (1994a).

Ladd, A. J. C., Numerical simulation of particular suspensions via a discretized Boltzmann equation. Part 2. Numerical results, *J. Fluid Mech.* **271**, 311-339 (1994b).

Ladd, A. J. C., Verberg, R., Lattice Boltzmann simulations of particle fluid suspensions, *J. Stat. Phys.* **104**, 1191-1251 (2001).

Lallemand, P., Luo, L.-S., Theory of the lattice Boltzmann method: dispersion, dissipation, isotropy, Galilean invariance, and stability, *Phys. Rev. E*. **61**, 6546-6562 (2000).

Lin, C.L., Lai, Y.G., Lattice Boltzmann method on composite grids. *Phys. Rev. E* **62**, Part A, 2219-2225 (2000).

Lockard, D. P., Luo, L.-S., Milder, S. D., Singer, B.A., Evaluation of Powerflow for aerodynamic applications, *Journal of Statistical Physics* **107**, 423-478 (2002).

Maier, R. S., Bernard, R. S., Grunau, D. W., Boundary conditions for the lattice Boltzmann methods, *Phys. Fluids*. **8** (1996).

McNamara, G., Zanetti, G., Use of the Boltzmann equation to simulate lattice-gas automata, *Phys. Rev. Lett.* **61**, 2332-2335 (1988).

Mei, R., Luo, L.-S., Shyy, W., An accurate curved boundary treatment in the lattice Boltzmann method, *J. Comp. Phys.* **155**, 307-330 (1999).

Mei, R., Shyy, W., On the finite difference-based lattice Boltzmann method in curvilinear coordinates, *J. Comp. Phys.* **143**, 426 (2000).

Mei, R., Shyy, W., Yu, D., Luo, L.-S., Lattice Boltzmann method for 3-D flows with curved boundary, *J. Comp. Phys.* **161**, 680-699 (2000).

Peyret, R., Taylor, T. D., *Computational Technique for Fluid Dynamics*, Vol. II, Springer-Verlag, New York (1983).

Qi, D., Lattice Boltzmann simulation of particles in non-zero-Reynolds-number flows. *J. Fluid Mech.* **385**, 41-62 (1999).

Qian, Y., d'Humieres, D., Lallemand, P., Recovery of Navier-Stokes equations using a lattice-gas Boltzmann method. *Europhys. Lett.* **17**, 479- (1992)

Rai, M.M, An implicit, conservative, zonal-boundary scheme for Euler equation calculation, AIAA-85-0488, 1985.

Schäfer, M., Turek, S., Benchmark computations of laminar flow over a cylinder, in *Notes in Numerical Fluid Mechanics*, Vieweg Verlag, Braunschweig, **52**, 547-566 (1996).

Shyy, W., Liu, J., Wright, J., Pressure-based viscous flow computation using multiblock overlapping curvilinear grid, *Numer. Heat Transf.* **25**, 39-59 (1994)

Shyy, W., Udaykumar, H. S., Rao, M. M., Smith, R. W., *Computational Fluid Dynamics With Moving Boundaries*, Taylor and Francis, Washington, DC (1996).

Shyy, W., *Computational Modeling for Fluid Flow and Interfacial Transport*, Corrected printing, Elsevier, Amsterdam (1997).

Shyy, W., Thakur, S.S., Ouyang, H., Liu, J., Blosch, E., *Computational Techniques for Complex Transport Phenomena*, Cambridge University Press, New York (1999).

Skordos, P. A., Initial and boundary conditions for the lattice Boltzmann method, *Phys. Rev. E.* **48**, 4823-4842 (1992).

Steger, J.L, Thought on the Chimera Method of Simulation of Three-Dimensional Viscous Flow, in Proceedings, computational Fluid Dynamics Symposium on Aeropropulsion, Cleveland, Ohio, NASA, CP-3078, 1-10, 1991.

Sterling, J. D., Chen, S., Stability analysis of lattice Boltzmann methods, *J. Comp. Phys.* **123**, 196-206 (1996).

Ye, T., Mittal, R., Udaykumar, H. S., Shyy, W., An accurate Cartesian grid method for viscous incompressible flows with complex immersed boundaries, *J. Comp. Phys.* **156**, 209-240 (1999).

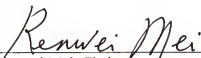
Ziegler, D.P., Boundary conditions for lattice Boltzmann simulations, *J. Stat. Phys.* **71**, 1171-1177 (1993).

Zou, Q., He, X., On pressure and velocity boundary conditions for the lattice Boltzmann BGK model, *Phys. Fluids* **9**, 1591-1598 (1997).

BIOGRAPHICAL SKETCH

Dazhi Yu received his B.S. degree in aerospace engineering in 1989 from Beijing University of Aeronautics and Astronautics in P.R. China. Then he worked at The Institute of Engineering Thermophysics, Chinese Academy of Sciences. He entered Ph.D program in the Department of Aerospace Engineering, Mechanics, and Engineering Science at the University of Florida in 1998.

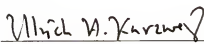
I certify that I have read this study and that in my opinion it conforms to acceptable standards of scholarly presentation and is fully adequate, in scope and quality, as a dissertation for the degree of Doctor of Philosophy.


Renwei Mei, Chairman
Professor of Aerospace Engineering,
Mechanics and Engineering Science

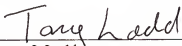
I certify that I have read this study and that in my opinion it conforms to acceptable standards of scholarly presentation and is fully adequate, in scope and quality, as a dissertation for the degree of Doctor of Philosophy.


Wei Shyy, Cochair
Professor of Aerospace Engineering,
Mechanics and Engineering Science

I certify that I have read this study and that in my opinion it conforms to acceptable standards of scholarly presentation and is fully adequate, in scope and quality, as a dissertation for the degree of Doctor of Philosophy.

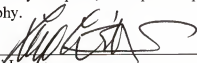

Ulrich H. Kurzweg
Professor of Aerospace Engineering,
Mechanics and Engineering Science

I certify that I have read this study and that in my opinion it conforms to acceptable standards of scholarly presentation and is fully adequate, in scope and quality, as a dissertation for the degree of Doctor of Philosophy.



Anthony J. Ladd
Professor of Chemical Engineering

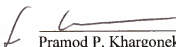
I certify that I have read this study and that in my opinion it conforms to acceptable standards of scholarly presentation and is fully adequate, in scope and quality, as a dissertation for the degree of Doctor of Philosophy.



Li-Shi Luo
Senior Staff of ICASE, NASA Langley
Research Center

This dissertation was submitted to the Graduate Faculty of the College of Engineering and to the Graduate School and was accepted as partial fulfillment of the requirements for the degree of Doctor of Philosophy.

August 2002



Pramod P. Khargonekar
Dean, College of Engineering

Winfred M. Phillips
Dean, Graduate School